

Hence, the numerical techniques help us to quickly understand the real flow environment and effectively communicate the conclusion. The CFD makes it possible to evaluate the field variables of the velocity, the pressure gradient between the proximal and distal of the vein graft model and the impact of the Wall Shear Stress (WSS) on the vein graft wall throughout a solution domain (Rory F. Rickard et al., 2009).

The 3D CFD analysis in this research is applied to calculate the velocity of the blood flow, the gradient of the blood flow pressure between the proximal and distal in the RSVG model, and the WSS impact on the RSVG wall that consist of the searching of the blood flow patterns in an applied irregular RSVG model; the oversize in the length and mismatching in the internal diameter between the RSVG model and the recipient artery and applying the boundary conditions of the blood flow models.

## **1.2 Problem Statement and Research Scope**

Even though the procedure was successfully performed by surgeons, its durability and longevity is still unpredictable. There are many upper limb vein graft failure cases that have been reported (George D. Chloros et al., 2008). Based on previous reports, most defected finger was cool and pale (Dumanian GA et al., 1998, Jocelyn A. et al, 2007,P., Berg et al., 2007, and Zol B.,Kryger et al., 2007).

Based on previous studies, the irregular vein geometry formation such as the kinking of the vein (H., Piza-Katzer, 1979; Qin, Liu et al., 2008) as well as a mismatch size of the internal diameter of the end-to end vein graft (H., Piza-Katzer, 1979; Chuang, DCet al., 1982; Rory F. et al., 2009) causes the vein graft failure. In fact, the length and internal diameters of the vein are strongly related to the vein graft lifespan

(Christopher L. et al., 2001; Sang-Wook, Lee et al., 2003). Hemodynamics studies including the blood flow patterns, the velocity, the gradient of the blood pressure and the WSS were believed to initiate the development and the growth of arterial stenosis but the previous studies lack of the realistic physiological considerations such as the irregular RSVG formations, blood flow pulsatility, especially in the microvascular vein grafting.

For the present study, the 3D CFD method was used to find out the velocity of the blood flow, the pressure gradient between the proximal and distal of the vein graft models and the impact of the shear stress on the vein graft's model that flow through the model of kink and the mismatch size of the RSVG segment in order to study the survival and to ensure the prolonging of the vein graft lifespan as well (Christopher L. Skelly, 2001; Sang-Wook Lee, 2003).

We propose the oversize of the RSVG kinked length models with the variables amplitude of two cycled sinusoidal wavy RSVG since the over length kink RSVG failures occurred in variable length. We also propose the mismatch of the RSVG models to the recipient arteries are 1:1.1, 1:1.2 and 1:1.3. The ideal size of the vein graft model diameter ratio to the artery diameter is 1:1 and straight also have been proposed as an ideal straight vein graft in comparison with the mismatch size and the kink vein graft models since any fluid flows in the straight tube should be provided very accurate fluidic properties such as velocity etc. (Donald F. et al., 2003; I.G.Currie, 2003; Lee Waite, 2005).

The simulation work in understanding of the blood flow behavior in the microvessel vein graft is vital prior to any experimentation work as it will save life and the operation time on laboratory animals such as mice. This research assume that the govern blood is the Newtonian, incompressible fluid, homogenous and does not slip at

the vessel wall. The govern blood is assumed as Newtonian blood because the whole blood behaves as Newtonian fluid with a constant viscosity at 37°C, which is the human body temperature, is constant because it is biologically maintained by other human system. The whole blood is incompressible to ensure the Navier-Stokes equations can be applied in this research. The govern blood does not slip at the vessel wall because the whole blood is firmly attached to vessel wall. The whole blood is homogenous (single phase) in the whole human vessels. The vessel wall is assumed as cylindrical and rigid body and the blood flow in laminar flow because the vessel wall at digital artery is not tapered and low distend effect and the Reynolds numbers ranged from 9.375 to 36.

In order to obtain the blood flow characteristics, simulations have been carried out by using a variety of the Reynolds numbers ranged from 9.375 and 36. The various of Reynolds number based on cases are shown in Table 1.1. Despite this, the numerical models of the laminar at steady state ( $t=0s$ ) and transient state ( $t \neq 0s$ ) are also utilized in this work to simulate the microvessel blood flow problems. The FVM approach is used to carry out the simulation commercial software ANSYS Fluent Version 12.1.

Motivated by this concoction of problem statement and scope, the research on microvessel blood flow behavior in the irregular geometry formation model of the vein grafts has been executed and played a pivotal role in this research.

Table 1.1 : Various numbers of Reynolds number based on cases.

Case	Diameter, cm	Re at $V_{min}$	Re at $V_{mean}$	Re at $V_{max}$
Ideal Straight	0.10	9.375	18.75	28.13
1	0.11	10.31	20.62	30.94
2	0.12	11.25	22.50	33.75
3	0.13	12.19	24.38	36.00
A	0.10	9.375	18.75	28.13
B	0.10	9.375	18.75	28.13
C	0.10	9.375	18.75	28.13

### 1.3 Objective

The main objective of this research is to investigate the relationships between the effect of blood flow on the irregular geometry and thrombosis formation in microvessels that relate to their long term survival. In order to achieve the purpose of this study, the main objective and the pre-objectives of the project are summarized as below:

1. To validate the numerical models of the laminar models. This is because the reliability of the CFD models is of paramount importance in simulation and also to check any discrepancies between these models.
2. To simulate the steady state and the pulsatile blood flow in irregular geometry formation model of the vein grafts.
3. To identify any critical range of geometry dimensions.
4. To study the relationship between the irregular geometry formation model of the vein grafts and prolonging survival.

#### Some pre-objectives

1. Concerning grid independence and number of nodes study.

The grid independence study needs to be carried out for every irregular geometry model used in this research. This is because the created number of nodes in the irregular geometry model of the vein graft through meshing process varies according to the dimension of the irregular geometry model. To get an accurate result, a large number of nodes need to be archived in meshing. The simulation work was carried out continuously by setting the convergence history until the residual target of mass and momentum reach less than  $1 \times 10^{-6}$ .

2. Accomplishment of the blood flow simulation algorithm, boundary condition, the User Define Function (UDF) as well as the irregular geometry models.

The blood flow simulation algorithm, boundary condition, the UDF as well as the irregular geometry models have to be validated by peer reviewed simulation work. This is because the reliability of the simulation results can be questioned even though the grid independence is achieved. An incompressible Navier-Stokes Equation, Newtonian fluid, measuring velocity profile, the WSS impact on wall, pressure gradient, steady and pulsatile flow of the blood within irregular formation geometry of the vein graft model were chosen based on the simulation work previously done by other researchers.

The research objective can only be achieved after the completion of all research pre-objectives.

#### **1.4 Dissertation Organization**

This dissertation is presented in six chapters.

Chapter 1 deals with the introduction of the research and overview of this thesis. The fundamental of the upper extremity vein grafting surgery have been addressed in order to provide better solutions for the RSVG problem. This chapter also presents the CFD analysis, problem statement, research scope, objectives and finally the dissertation organization.

Chapter 2 presents a brief analysis of the overall literature review from previous CFD analysis that had been done by researchers. This chapter discusses about the application and the ability of the CFD Analysis in hemodynamic system. It also covers current vessel failures and the CFD Analysis method had been proposed and conducted

by previous authors. Later, a discussion on the summary of literature review and the research proposal is presented.

Chapter 3 discusses the theoretical blood flow in microvessels and the computational simulation study. In this chapter, the basic concepts of fluid mechanics are viewed as it is fundamental to describe the fluid dynamics. The simulation details, such as meshing, boundary conditions and the flow equations that have been applied in this study are also mentioned.

Chapter 4 explains the research methodology. This chapter presents the validation of the blood flow simulation algorithms, the grid independence of irregular formation of the vein graft model, the boundary conditions in irregular formation of the vein graft model as well as the numerical models.

Chapter 5 presents the results and discussion for the blood flow in steady state simulations on ideal vein graft model and the irregular formation of the vein graft models followed by the pulsatile blood flow results.

Finally, the conclusion and future work recommendations are presented in Chapter 6.

## CHAPTER 2

### LITERATURE REVIEW

#### 2.1 Literature Review

This chapter provides the CFD Analysis method that has been applied by previous researchers. Their research methodologies are also discussed. Finally, the inferences in the vessel failure were mentioned at the end of this chapter.

The CFD method is applied to determine the hemodynamic factors such as the deformation erythrocytes (Secomb T.W. et al., 2007; A. Jafari et al., 2009; Doddi, S.K. & Bagchi, P., 2009), the blood viscosity (Cole JS et al., 2003; Filipovic N. et al., 2009), the shear stress impact on the vessel wall (Klyszcz T. et al., 1997; Cole JS et al., 2003), and the blood flow velocity (Jung F. & Zeintl H., 1997; Mette S. Olufsen et al., 2000; Filipovic N. et al., 2009; Tzu-Ching Shih, et al., 2011) in the complex 3D blood microvessels. Their previous researches exposed that the CFD technique not only can show the information of the blood flow motion but also the changing in shape of the Red Blood Cells flowing in the microvessels. As a conclusion, they found out that the numerical method become a powerful method to study the patterns of the blood flow especially in the geometrically complex vessel.

A. Jafari et al. ( 2009 ) applied a commercially available Fluent ANSYS Inc. CFD package Fluent 6.2 which is based on the finite volume method in order to simulate the behavior of the blood flow in microvessels. The 3D CFD modeling and

simulation are also presented on the motion of a large number of deformable cells in the microchannels (Doddi, S.K. & Bagchi, P., 2009).

The CFD method of the pulsatile flow, non-Newtonian of the blood flow through a femoral artery bypass model, have been conducted by Cole JS et al. (2003) in order to understand the bypass blood flows, and to identify factors of the blood flow which contribute to the progression of disease such as thrombosis. From their research, more effective bypass design could be developed and prolonged the lifespan of the femoral artery bypass.

Tzu-Ching Shih, et al. (2011) also applied the CFD method in his research to calculate the velocity of the Red Blood Cells (RBCs) in six cases microvessels of finger nail-fold. They reconstructed 3D images from 2D images of the microvessel. They assumed that the capillaries in a circular cross sections and the vessels walls as non-slip boundary conditions. An origin velocity of the Red Blood Cells flowing into each microvessel was calculated by the Optical Flow Estimation (OFE). The velocities of multiple points along each microvessel simulated by the CFD, Average results of the CFD, were compared with the Optical Flow Estimation (OFE) calculations, the Velocity of Optical Flow Estimation. The study indicates that the CFD method can be considered as one of acceptable methods by providing reasonable accuracy in the result of the RBCs velocity in the finger nail-fold microvessels.

The relationships between the irregular geometry formation and the thrombosis were also previously studied by Qin Liu et al. (2008), Rory F. Rickard et al. (2009) and W. W. Jeong and K. Rhee (2009). Qin Liu et al. (2008) stated that the local shear stresses or shear rates, especially in the bent or stretched microvessels could induce the formation of the thrombus. For that reason, the bent or stretched microvessels was tested experimentally and simulated computationally. They found out that the thrombi



were originated at the inner wall of the curvature angle in these bent or stretched microvessel models. The 3D CFD using commercial software, Fluent ANSYS Inc., was used to determine the mechanical mechanism that induced the thrombus. The microvessels were modeled with variable shaped cross-sections (elliptic and circular) as well as different curvature ( $0^\circ$ ,  $90^\circ$  and  $180^\circ$ ) in order to simulate the stretching and bending microvessels. From their CFD simulation result, the inner wall of the curved circular shaped microvessel models showed the highest values in the Wall Shear Rate and the Wall Shear Rate gradient at the inner wall of the curved circular-shaped microvessel models. They are found at the inner side when the vessels are bent and two apexes of the wall with shorter axis for the  $0^\circ$  (straight) elliptic shaped vessel. From their observation, the bent and elliptic-shaped microvessels have strongly related to the different value in the shear stresses or shear rates. They also found out that the value of shear stress or shear rates gradient between the outer and the inner wall of the microvessels become higher in more bent and the angle of the elliptic-shaped microvessels.

Rory F. Rickard et al. (2009) stated that the vessel size mismatch could cause anastomotic failure in the microvascular surgery. In the surgical procedure, an end-to-end attachment has to be applied if an end-to-side anastomosis is not available. Most of end-to-end techniques are characterized to deal with the size mismatch. Their research objective was to numerically analyze the WSS and the blood flow patterns in four idealized end-to-end anastomoses artery models, where the upstream or the recipient artery is smaller than the downstream. The four techniques model were a wedge cut of the larger vessel, an oblique region of smaller blood vessel, a fish-mouth cut of small vessel and an invaginating attachment. The blood flow was remodeled by the FVM applying the commercially available CFD code Fluent ANSYS Inc. From their

experimental simulation works, the invagination model showed that the ring vortices happened. The word 'vortices' is a plural noun for the vortex and it happens when the flow is mostly in a spinning motion. The ring vortices also have been seen in the fish-mouth model. However, the ring vortices effects were less seen in the invagination model compare to the fish-mouth model. The counter-rotating, spiral, complex vertices were found dispersed downstream in the oblique region. The first wedge model showed least flow separation, with the high flow became centralized but decelerated in the flow rate. The impacts of the WSS were similar for all models. They concluded that by shortening the length of the wedge or increasing the downstream vessel radius to 1.5mm led to separation in the blood flow.

W. W. Jeong and K. Rhee (2009) believed that the existing and growth of the arterial stenosis caused hemodynamic factors including the blood viscosity characteristics, the shear stress and the blood flow pattern, but they are still lack in previous studies of realistic physiological considerations. They suggested that the flow pulsatility, non-Newtonian viscosity and the irregular surface geometry may cause arterial stenosis problem as a research inference. They used the arterial models that suffered with 48 percent occlusions under clinical blood flow function in order to explore the effect of the non-Newtonian viscosity and the irregularity at the surfaces on the blood flow regions. The CFD based on the FVM was applied for the non-Newtonian and Newtonian characterized blood model in their research. Based on their observation after the experimental work, the WSS in those smooth surface simulation models were lower compared to the model in suffered irregularity at the surface. They found out that the non-Newtonian viscosity in the blood properties are strongly related to the increasing of the WSS. They also found out that the dimension less pressure drop and the time average of the WSS in steady state flow was lower than in the pulsatile

flow. However, the WSS and the pressure gave less effect in the pulsatility effects compared to the non-Newtonian viscosity in the blood properties. By the end of their research, they found out that the non-Newtonian viscosity in the blood properties and artery model with suffered irregularity in the surface could predict pressure drop and the WSS in the stenosis arteries.

Minh Tuan Nguyen and Lee (2012) did the CFD simulations on the laminar flow in nine sinusoidal wavy shaped tubes conducted for mean Reynolds number of 250, which is in the range of clinical flow-rate and investigated flow structures, pressure distribution and particle trajectories both in steady state and periodic flow conditions. For comparison purposes, six wave lengths and amplitudes of sine function for geometry of the tube models were tested. The results showed that small amplitude secondary curvature has significant influence on the nature of the flow patterns and the particle mixing mechanism. This reveals that the characterizing accurate geometry is essential in accurate predicting of in vivo hemodynamics and may motivate further studies on any possibility with regards to the reflection of the secondary flow on the vascular remodeling and the pathophysiology.

## **2.2 Summary**

From literature reviews, the previous studies revealed that the CFD method could be applied in the human vessel and give the information of the blood flow behavior. For that reason, the 3D Fluent software is applied in this research. The vessel mismatch (the recipient artery is smaller than the vein graft) can cause anastomotic failure in the microvascular. As in our inference, the vessel size mismatched (the recipient artery is larger than the vein graft) also could cause anastomotic failures.

Thrombi were originated at the inner wall of the curvature angle in these bent in the microvessel models. We predict that the re-formation of thrombi also will occur in various amplitude of sinusoidal wavy vein graft. The end-to-end mismatched internal diameter and the kinked over length of the Reverse Saphenous Vein Grafts (RSVGs) have been proposed as the irregular geometries formation for this research. For the blood flow model, the laminar steady state and the laminar pulsatile state have been set as the blood flow model.

© This item is protected by original copyright

## CHAPTER 3

### THEORETICAL BLOOD FLOW IN THE MICROVESSELS AND THE COMPUTATIONAL SIMULATION STUDY

#### 3.1 Review of Basic Fluid Mechanics Concept

Density is the mass per unit volume of a substance and is given by the Greek character  $\rho$  (rho). The SI units for  $\rho$  are  $kg/m^3$  and the approximate density for blood is  $1050 kg/m^3$ . In other word, blood is slightly denser than water.

$$\rho = \frac{kg}{m^3} \quad (3.1)$$

The specific weight is an inversely to density ( $\gamma=1/\rho$ ), presented by Greek symbol  $\gamma$  (gamma), is defined as its weight over volume. Thus,  $\gamma$  can be related to density through the equation

$$\gamma = \rho g [N/m^3] \quad (3.2)$$

Where  $g$  is the gravitational force and is always used to present the weight of the system.

##### 3.1.1 Viscosity

The common fluids, such as water, oil, petrol and air, the shear stress and shear stress rate are indicated by this equation which can be related to the relationship of the form

$$\tau = \mu \frac{du}{dy} \quad (3.3)$$

where the constant of proportionality is presented by the Greek symbol – ( $\mu$ ) and also called the *dynamic viscosity*, the *absolute viscosity*, or simply the *viscosity* of the fluid. According to Equation 3.3, the graph plots of the shear stress,  $\tau$  versus shear stress rate,  $du/dy$  should be linear with the slope equal to the viscosity as shown in Figure 3.1. The particle of the fluid relates the actual value of the viscosity and also highly relates on temperature as shown in Figure 3.1 with the two curves for water. The Newtonian fluids can be defined when the shear stress of fluids is linearly related to the stress strain rate (also referred to the angular deformation rate). The formulation of Equation 3.3 is a general formulation and applicable in more complex flow type of the Newtonian fluids.

Meanwhile, the non-Newtonian fluids can be defined when the shear stress of fluids are not linearly related to the shear strain rate. For this research, we assume that blood is homogenous and Newtonian fluid.

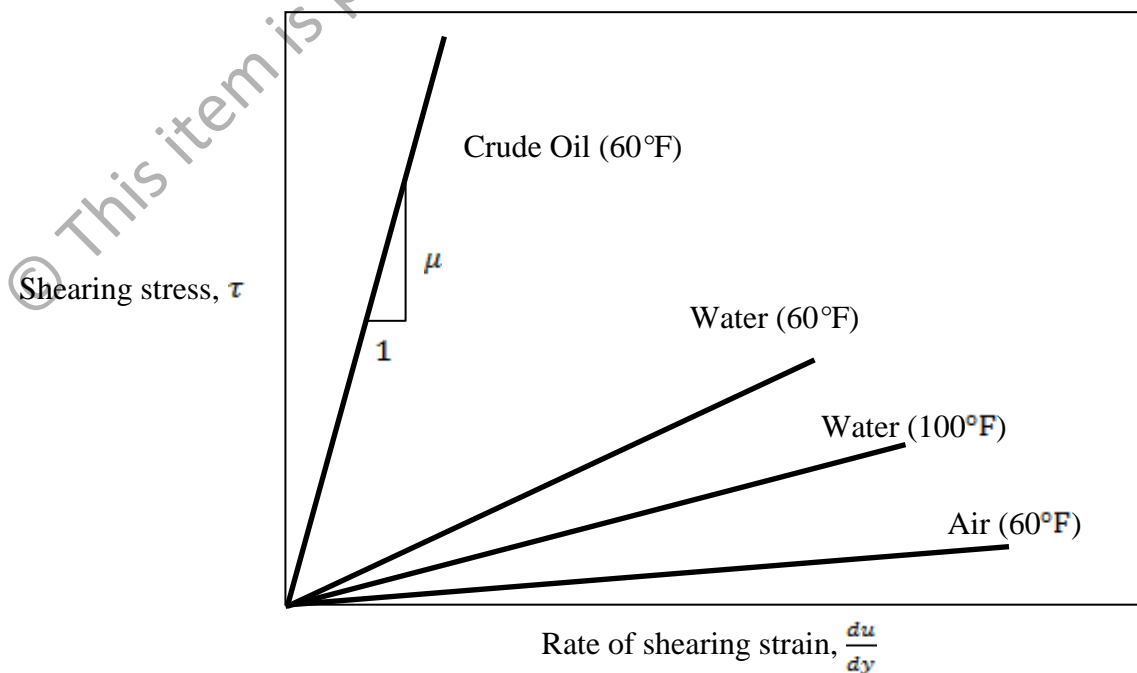


Figure 3.1 Linear variation of shear stress with shear strain rate for common fluids.

### 3.1.2 Pressure Variation in a Fluid at Rest and Incompressible Fluid

#### 3.1.2.1 Pressure Variation in a Fluid at Rest

$$\frac{dp}{dz} = -\gamma \quad (3.4)$$

An Equation 3.4 is the fundamental equation for fluids at rest (no external force) and can be used to determine how pressure with the elevation level, where  $dp$  is differential in pressure and  $dz$  is differential in the elevation level. This equation indicates that the pressure gradient in the vertical direction is negative value which means that the pressure decreases if we move upward in a fluid at rest.

#### 3.1.2.2 Incompressible Fluid

The specific weight is equal to the product of fluid density and the acceleration of gravity ( $\gamma = \rho g$ ), changes in  $\gamma$  are caused by a change in either  $\rho$  or  $g$ . For most engineering applications the variation in  $g$  is negligible, so our concern to the product of fluid density and the acceleration of gravity. Commonly, a fluid with constant density ( $\rho = \text{constant}$ ) is called an incompressible fluid. For this research, we also assume that blood is incompressible fluid and we also ignore about the acceleration gravity in our calculation. We usually neglect the liquids with the variation in density value and applicable even it is over large vertical distances, so that the

assumption of constant specific weight ( $\gamma = \text{constant}$ ) when dealing with any liquid is a good one.

### **3.1.3 Differential Analysis of Fluid Flow - Microscopic Balances of Mass and Momentum**

The main goal of biofluid mechanics in this research is to identify the relationship between variables so that the value of one or more of these variables can be determined in terms of given boundary conditions. As a first step, the basic balances of properties or “Conservation Laws” that involve multiple variables of interest will be introduced. The view of biofluid mechanics study is divided into two parts which are Macroscopic and Microscopic view. Since our study focuses on Microscopic Balances of Mass and Momentum in the microvessel blood flow, these laws relative to an infinitesimal or Microscopic volume will be evaluated. By doing the Microscopic approach, complex and detailed parameters can be determined such as local velocity, pressure and so on.

### **3.1.4 Conservation of Mass– Derivation of the Continuity Equation**

A system is defined as a collection of unchanging contents, so the conservation of mass principle for a system is simply stated as

$$\text{Time rate of change the system mass} = 0$$



or

$$\frac{DM_{sys}}{Dt} = 0 \quad (3.5)$$

Where  $M_{sys}$  is the system mass.

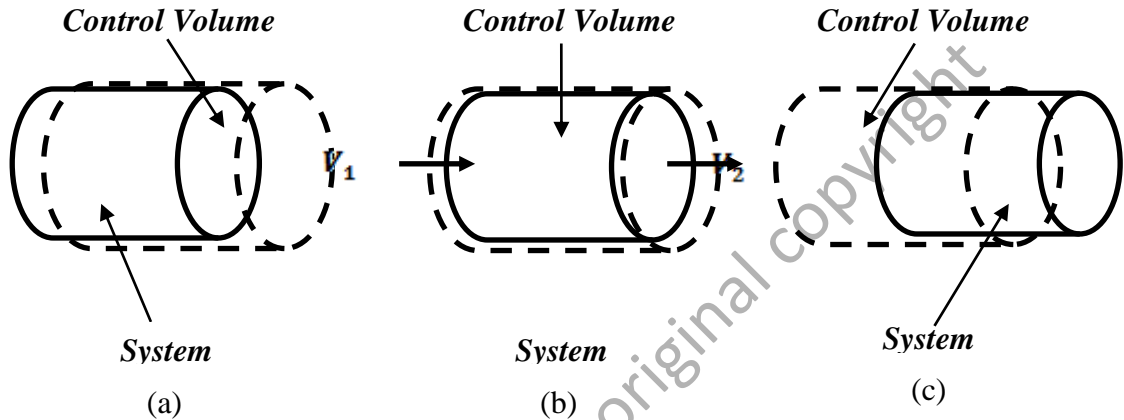


Figure 3.2 System and control volume in the tube at three different instances of time. (a) System at time  $t - \delta t$ . (b) System and control volume at  $t$ , coincident condition. (c) System and control volume at  $t + \delta t$ .

Figure 3.2 shows a system and a fixed, non-deforming control volume that is coincident at an instant of time. Thus, we can express Equation 3.6 which is also a derivation result from the Reynolds transport theorem that allows us to state,

$$\frac{DM_{sys}}{Dt} = \frac{\partial M_{cv}}{\partial t} + \rho_2 A_2 V_2 + \rho_1 A_1 V_1 \quad (3.6)$$

or can be expressed as

Time rate of change of the mass of the coincident system	=	Time rate of change of the mass of the contents of the coincident control volume	=	Net rate of flow of mass through the control surface
--	---	--	---	--

Because the amount of mass in volume  $dV$  is  $\rho dV$ , it follows that the amount of mass in the control volume,  $M_{cv}$ , can be written as in Equation 3.7

$$M_{cv} = \int_{cv} \rho dV \quad (3.7)$$

If the control volume has multiple inlets and outlet, Equation 3.6 can be arranged by replacing with Equation 3.7 for flow through each of the inlets and outlets to give Equation 3.8

$$\frac{DM_{sys}}{Dt} = \frac{\partial}{\partial t} \int_{cv} \rho dV + \sum \rho_{out} A_{out} V_{out} - \rho_{in} A_{in} V_{in} \quad (3.8)$$

When a flow is at steady state flow ( $t=0s$ ), all field properties at any specified point), including density,  $\rho$ , remain constant with time and the time rate of change of the mass of the contents of the control volume is zero (Equation 3.9 and 3.10).

$$\frac{\partial M_{cv}}{\partial t} = 0 \quad (3.9)$$

$$\frac{\partial}{\partial t} \int_{cv} \rho dV = 0 \quad (3.10)$$

The control volume expression for *conservation of mass*, commonly called the *continuity equation*, is obtained by combining Equation 3.5 and Equation 3.8 to obtain Equation 3.11.

$$\frac{\partial}{\partial t} \int_{cv} \rho dV + \sum \rho_{out} A_{out} V_{out} - \rho_{in} A_{in} V_{in} = 0 \quad (3.11)$$

From Equation 3.11 the mass can be conserved if the time rate of change of the mass of the contents of the control volume plus the net rate of mass flow through the control

surface of the control volume plus the net rate of mass flow through the control surface equal to zero.

For the *mass flowrate*,  $\dot{m}$  symbol is often expressed, through a section of the control volume having area  $A$  as in Equation 3.12.

$$\dot{m} = \rho AV = \rho \quad (3.12)$$

where  $\rho$  is the density of fluid,  $V$  is the normal velocity component of fluid to the area  $A$ , and  $Q=VA$  is the volume flowrate ( $m^3/s$ ). Note the symbols used to denote mass,  $m$  (kg), and mass flowrate,  $\dot{m}$ (kg/s).

The case of the fluid flow across the non-uniform section area  $A$  always happens. For that case, the appreciate fluid velocity to use in Equation 3.22 is the average value of the component of velocity normal to the section is involved. This average value,  $\bar{V}$ , is defined in Equation 3.13 and shown in the Figure 3.6.

$$\bar{V} = \frac{\int_A \rho V dA}{\rho A} \quad (3.13)$$

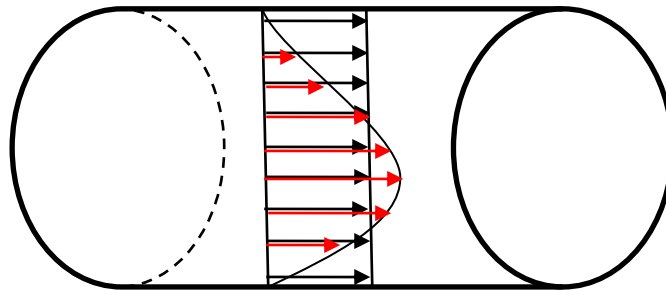


Figure 3.3 Uniform (Mean) and Non-uniform blood flow velocity profile through the straight tube

### 3.1.4.1 Differential Form of Conservation of Mass/Continuity Equation

The small and stationary cubical element will be taken as our control volume as illustrated in Figure 3.4.

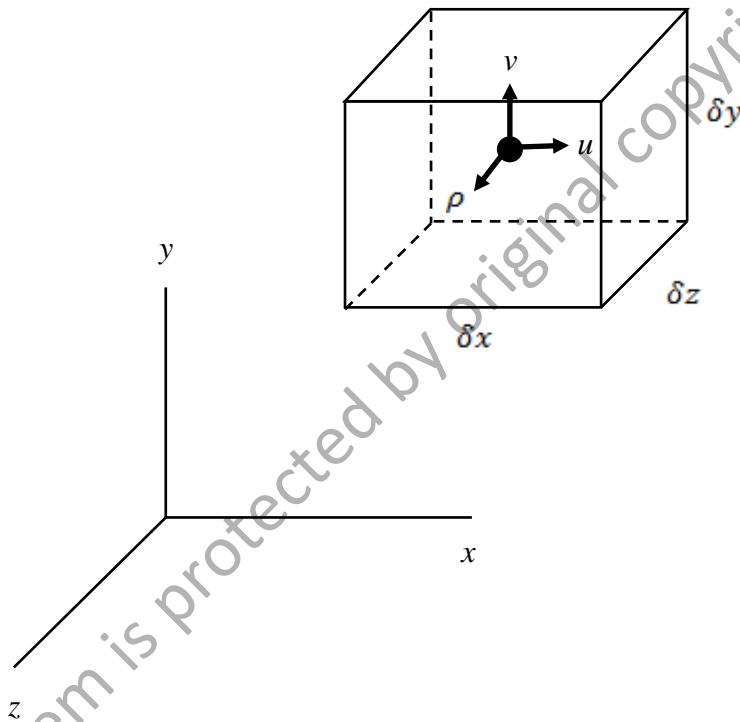


Figure 3.4 The differential element for the development of conservation of mass equation.

At the center of the element the fluid density is  $\rho$  and the velocity has component  $u$ ,  $v$  and  $w$ . Since the element is small the volume integral in Equation 3.10 can be expressed as

$$\frac{\partial}{\partial t} \int_{cv} \rho dV \approx \frac{\partial \rho}{\partial t} \delta x \delta y \delta z \quad (3.14)$$

The rate of mass flow through the surfaces of the element can be obtained by considering the flow in each of the coordinate direction separately. For example, in Figure 3.5 flow in the  $x$  direction is depicted.

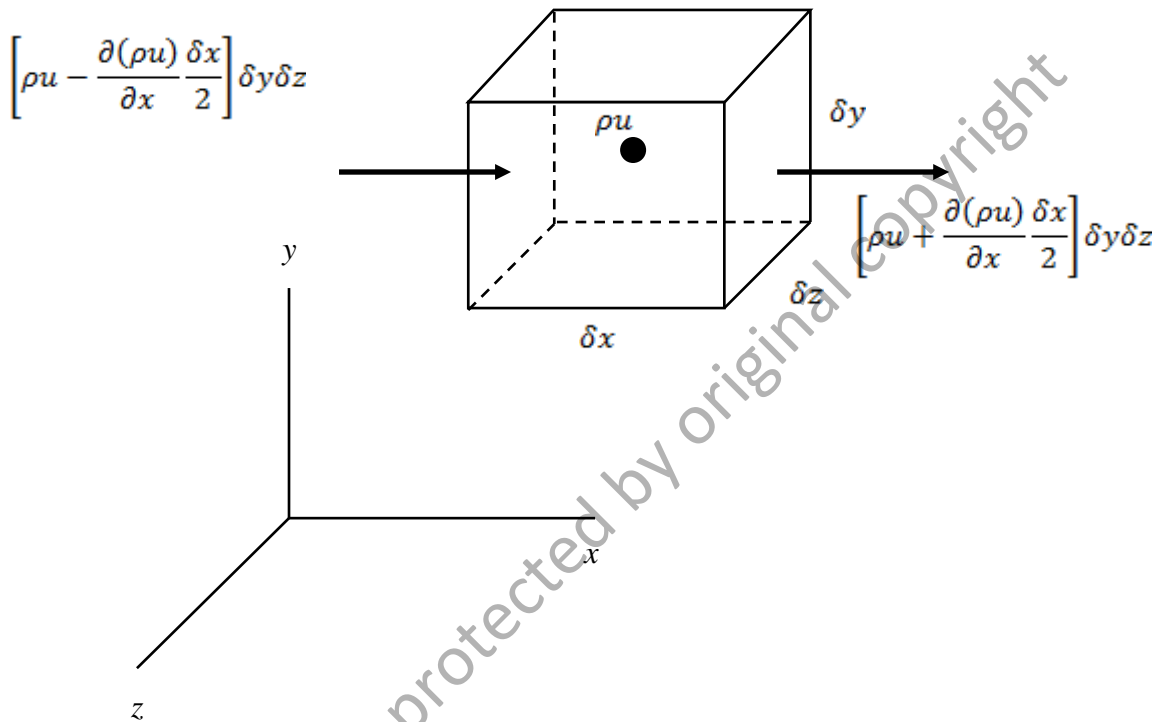


Figure 3.5 The differential element for the development of conservation of mass equation.

If we let  $\rho u$  represents the  $x$  component of the mass rate of flow per unit area at the center of the element, then on the right face

$$\rho u|_{x+(\delta x/2)} = \rho u + \frac{\partial(\rho u)}{\partial x} \frac{\delta x}{2} \quad (3.15)$$

and on the left face

$$\rho u|_{x-(\delta x/2)} = \rho u - \frac{\partial(\rho u)}{\partial x} \frac{\delta x}{2} \quad (3.16)$$

Note that we are really using Taylor series expansion of  $\rho u$  and neglecting higher order terms such as  $(\delta x)^2$ ,  $(\delta x)^3$  and so on. When the right-hand sides of Equation 3.15 and Equation 3.16 are multiplied by the area  $\delta y \delta z$ , the rate in which the mass is crossing the right and left sides of the element is obtained, as illustrated in Figure 3.5. When these two expressions are combined, the net rate of mass flowing from the element through the two surfaces can be expressed as

$$\begin{aligned}
 \text{Net rate of mass outflow in } x \text{ direction} &= \left[ \rho u + \frac{\partial(\rho u)}{\partial x} \frac{\delta x}{2} \right] \delta y \delta z - \left[ \rho u - \frac{\partial(\rho u)}{\partial x} \frac{\delta x}{2} \right] \delta y \delta z = \frac{\partial(\rho u)}{\partial x} \delta x \delta y \delta z \\
 &= \frac{\partial(\rho u)}{\partial x} \delta x \delta y \delta z
 \end{aligned} \tag{3.17}$$

For simplicity, only the flow in the  $x$  direction has been considered in Figure 3.8, but, in general, there will also be flows in the  $y$  and  $z$  directions. An analysis similar to the one used for the flow in the  $x$  direction shows that

$$\text{Net rate of mass outflow in } y \text{ direction} = \frac{\partial(\rho v)}{\partial y} \delta x \delta y \delta z \tag{3.18}$$

and

$$\text{Net rate of mass outflow in } z \text{ direction} = \frac{\partial(\rho w)}{\partial z} \delta x \delta y \delta z \tag{3.19}$$

Thus,

$$\text{Net rate of mass outflow} = \left[ \frac{\partial(\rho u)}{\partial x} + \frac{\partial(\rho v)}{\partial y} + \frac{\partial(\rho w)}{\partial z} \right] \delta x \delta y \delta z \tag{3.20}$$

From Equation 3.18, 3.19, and 3.20, these do not follow that differential equation for the conservation of mass is

$$\frac{\partial \rho}{\partial t} + \frac{\partial(\rho u)}{\partial x} + \frac{\partial(\rho v)}{\partial y} + \frac{\partial(\rho w)}{\partial z} = 0 \quad (3.21)$$

As mentioned previously, this equation is also commonly referred as the continuity equation.

The continuity equation is one of the fundamental equations of fluid mechanics and, as expressed in Equation 3.21, is valid for a steady or unsteady flow, and compressible or incompressible fluids. In vector notation, Equation 3.21 can be simplified as in Equation 3.22.

$$\frac{\partial \rho}{\partial t} + \nabla \cdot \rho \mathbf{V} = 0 \quad (3.22)$$

Two special cases are of particular interest. For *steady* flow ( $t=0s$ ) of *compressible* ( $\rho \neq \text{constant}$ ) fluids (Equation 3.23 or 3.24)

$$\nabla \cdot \rho \mathbf{V} = 0 \quad (3.23)$$

or

$$\frac{\partial(\rho u)}{\partial x} + \frac{\partial(\rho v)}{\partial y} + \frac{\partial(\rho w)}{\partial z} = 0 \quad (3.24)$$

This follows since the definition  $\rho$  is not a function of time for steady flow, but could be a function of position. For *incompressible* fluids the fluid density,  $\rho$ , is a constant ( $\rho = \text{constant}$ ) throughout the flow so that Equation 3.22 becomes (Equation 3.25 or 3.26)

$$\nabla \cdot \mathbf{V} = 0 \quad (3.25)$$

or

$$\frac{\partial u}{\partial x} + \frac{\partial v}{\partial y} + \frac{\partial w}{\partial z} = 0 \quad (3.26)$$

Equation 3.25 and 3.26 apply to both steady and unsteady flow of incompressible fluids.

### 3.1.5 Conservation of Momentum

In deriving the differential form of this law, the dynamics associated with a fluid control volume ( $\Delta v = \Delta x \Delta y \Delta z$ ) are considered once again as shown in Figure 3.6.

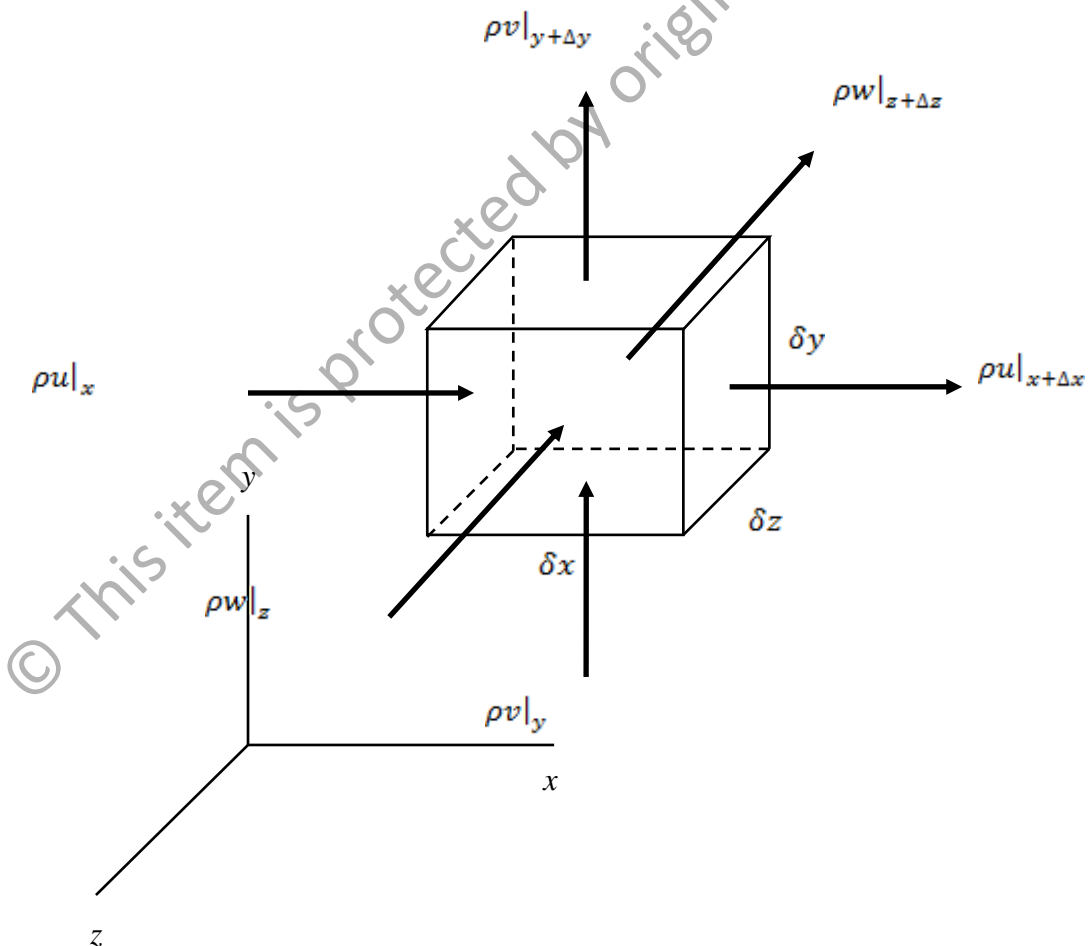


Figure 3.6 Mass flux across the surfaces of control volume



Newton's Second Law of Motion is now applied, as written in Equation 3.27, in terms of the time rate of change of momentum (Equation 3.28):

$$\Sigma \vec{F} = m\vec{a} \quad (3.27)$$

Sum of the external <i>forces</i> acting on the Control Volume	=	Net rate of efflux of <i>linear momentum</i> across the Control Volume	=	Time rate of change of linear momentum <i>within</i> the Control Volume
---	---	---	---	--

(3.28)

In general, the linear momentum per unit volume fluid can be expressed as  $\rho\vec{v}$  so that by multiplying this term by the rate of volume change, we can obtain the time rate of change of the linear momentum. To determine the flux of a property *across* the Control Volume surface, the appropriate expression for the rate of volume change is  $(\vec{v} \cdot \hat{n}) dA$ , where  $\hat{n}$  is the outward directed normal to a particular surface. For a change of the property *within* the Control Volume, the rate of the volume change is simply given by  $\frac{dv}{dt}$ . As in the derivation of the Continuity Equation, the Control Volume considered is constant and we can express the above equality in Equation 3.29.

$$\lim_{\Delta v \rightarrow 0} \frac{\Sigma \vec{F}}{\Delta x \Delta y \Delta z} = \lim_{\Delta v \rightarrow 0} \iint \frac{\rho \vec{v} (\vec{v} \cdot \hat{n}) dA}{\Delta x \Delta y \Delta z} + \lim_{\Delta v \rightarrow 0} \frac{\partial}{\partial t} \iiint \frac{\rho \vec{v} dV}{\Delta x \Delta y \Delta z} \quad (3.29)$$

If we take the limit of  $\Delta v = \Delta x \Delta y \Delta z$  as it approaches zero.

Each of these terms can be evaluated separately as follows:

1. Sum of the external forces (Equation 3.30)

$$\lim_{\Delta v \rightarrow 0} \frac{\Sigma \vec{F}}{\Delta x \Delta y \Delta z} = d\vec{F} \quad (3.30)$$

2. Net rate of momentum efflux across the control volume (Equation 3.31)

$$\lim_{\Delta v \rightarrow 0} \iint \frac{\rho \vec{v}(\vec{v} \cdot \hat{n}) dA}{\Delta x \Delta y \Delta z} = \frac{\partial}{\partial x} (\rho V u) + \frac{\partial}{\partial y} (\rho V v) + \frac{\partial}{\partial z} (\rho V w) = \vec{V} \left[ \frac{\partial}{\partial x} (\rho u) + \frac{\partial}{\partial y} (\rho v) + \frac{\partial}{\partial z} (\rho w) \right] + \rho \left[ u \frac{\partial \vec{v}}{\partial x} + v \frac{\partial \vec{v}}{\partial y} + w \frac{\partial \vec{v}}{\partial z} \right]$$

(3.31)

At this point, we can also use the Continuity Equation to substitute terms (Equation 3.32)

$$\frac{\partial}{\partial x} (\rho u) + \frac{\partial}{\partial y} (\rho v) + \frac{\partial}{\partial z} (\rho w) = -\frac{\partial \rho}{\partial t}$$

(3.32)

and reduce this limit to (Equation 3.33)

$$\lim_{\Delta v \rightarrow 0} \iint \frac{\rho \vec{v}(\vec{v} \cdot \hat{n}) dA}{\Delta x \Delta y \Delta z} = -\vec{V} \frac{\partial \rho}{\partial t} + \rho \left[ u \frac{\partial \vec{v}}{\partial x} + v \frac{\partial \vec{v}}{\partial y} + w \frac{\partial \vec{v}}{\partial z} \right]$$

(3.33)

3. Time rate of change of momentum within the control volume (Equation 3.34)

$$\lim_{\Delta v \rightarrow 0} \iiint \frac{\vec{v} \rho dV}{\Delta x \Delta y \Delta z} = \frac{\partial}{\partial t} (\rho \vec{V}) = \rho \frac{d\vec{v}}{dt} + \vec{V} \frac{\partial \rho}{\partial t}$$

(3.34)

Substituting for the limits and combining the terms gives Equation 3.35

$$d\vec{F} = \rho \left[ u \frac{\partial \vec{v}}{\partial x} + v \frac{\partial \vec{v}}{\partial y} + w \frac{\partial \vec{v}}{\partial z} \right] + \rho \frac{d\vec{v}}{dt}$$

(3.35)

The change of momentum has been expressed in terms of its components velocities. Let us look at the external forces in further details. They consist of the sum of the **body forces**,  $\vec{F}_B$ , and the **surface forces**,  $\vec{F}_S$ . The forces are typically due to the presence of gravitational, electromagnetic, and electrostatic fields. If the only body force is gravity, then (Equation 3.36)

$$F_{BX} = \rho g_x \Delta x \Delta y \Delta z$$

(3.36)

The surface forces acting on the control volume are those due to the normal,  $\sigma$ , and the shear stress,  $\tau$ , stresses. These stresses can be assumed to vary continuously from their nominal values at the center of the Control Volume in each of the coordinate directions as illustrated in Figure 3.10.

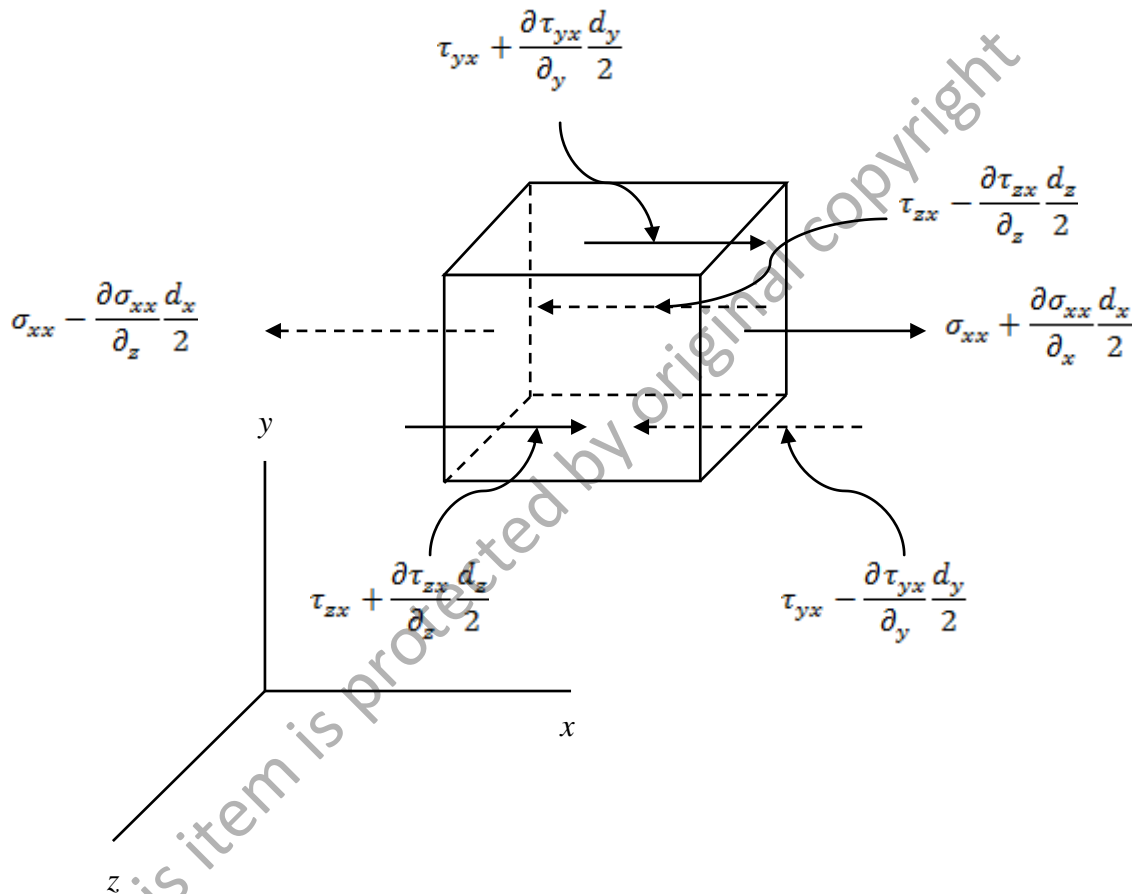


Figure 3.7 Normal and shear stresses along the  $x$  coordinate in the Control Volume

Figure 3.7 depicts the normal and shear stresses acting on the Control Volume in the  $x$  direction alone. Similar figures can be constructed for the normal and shear stresses acting in the  $y$  and  $z$  directions. This, the net surfaces force acting in the  $x$  direction is given in Equation 3.37.

$$F_{Sx} = \left(\frac{\partial \sigma_{xx}}{\partial x}\right) \Delta x \Delta y \Delta z + \left(\frac{\partial \tau_{yx}}{\partial y}\right) \Delta x \Delta y \Delta z + \left(\frac{\partial \tau_{zx}}{\partial z}\right) \Delta x \Delta y \Delta z \quad (3.37)$$

The total force acting on the control volume in the  $x$  direction then becomes (Equation 3.38)

$$F_x = F_{Bx} + F_{Sx} \quad (3.38)$$

which, in the limit, can be expressed in Equation 3.48a.

$$dF_x = \rho g_x + \frac{\partial \sigma_{xx}}{\partial x} + \frac{\partial \tau_{yx}}{\partial y} + \frac{\partial \tau_{zx}}{\partial z} \quad (3.38a)$$

Similarly, the differential force components in the  $y$  and  $z$  directions are:

$$dF_y = \rho g_y + \frac{\partial \sigma_{yy}}{\partial y} + \frac{\partial \tau_{xy}}{\partial x} + \frac{\partial \tau_{zy}}{\partial z} \quad (3.38b)$$

$$dF_z = \rho g_z + \frac{\partial \sigma_{zz}}{\partial z} + \frac{\partial \tau_{xz}}{\partial x} + \frac{\partial \tau_{yz}}{\partial y} \quad (3.38c)$$

By substituting the results of the above expression in Equation 3.38a to 3.38c back into the expression for the Newton's Second Law (Equation 3.39) yield in Equation 3.40a to 3.40c.

$$\sum F = m \left( \frac{d\vec{v}}{dt} \right) = \frac{d(m\vec{v})}{dt} \quad (3.39)$$

$$\rho g_x + \frac{\partial \sigma_{xx}}{\partial x} + \frac{\partial \tau_{yx}}{\partial y} + \frac{\partial \tau_{zx}}{\partial z} = \rho \left( \frac{\partial u}{\partial t} + u \frac{\partial u}{\partial x} + v \frac{\partial u}{\partial y} + w \frac{\partial u}{\partial z} \right) \quad (3.40a)$$

$$\rho g_y + \frac{\partial \tau_{xy}}{\partial x} + \frac{\partial \sigma_{yy}}{\partial y} + \frac{\partial \tau_{zy}}{\partial z} = \rho \left( \frac{\partial v}{\partial t} + u \frac{\partial v}{\partial x} + v \frac{\partial v}{\partial y} + w \frac{\partial v}{\partial z} \right) \quad (3.40b)$$

$$\rho g_z + \frac{\partial \tau_{xz}}{\partial x} + \frac{\partial \tau_{yx}}{\partial y} + \frac{\partial \tau_{zz}}{\partial z} = \rho \left( \frac{\partial w}{\partial t} + u \frac{\partial w}{\partial x} + v \frac{\partial w}{\partial y} + w \frac{\partial w}{\partial z} \right) \quad (3.40c)$$

In this form, we can see that the right-hand side of the above equations actually represents density (mass/volume) X acceleration, or force/volume, where the acceleration terms can be separated in **local acceleration** ( $\partial u/\partial t$ , etc.) component. The total acceleration can be expressed in terms of the substantive derivative in Equation 3.41.

$$\frac{Du}{Dt} = \frac{\partial u}{\partial t} + u \frac{\partial u}{\partial x} + v \frac{\partial u}{\partial y} + w \frac{\partial u}{\partial z} \quad (3.41)$$

Equation 3.40a to 3.40c represents the complete form of the different Conservation of Momentum balances. These equations cannot be solved, however, because there are more unknowns (i.e., dependent variables) than equations. Thus, it is necessary to derive additional information in order to provide those equations. Those equations are applicable for incompressible Newtonian fluids. Here, the **normal** and **shear** stresses can be expressed in Equation 3.42a-c.

$$\sigma_{xx} = -p + 2\mu \frac{\partial u}{\partial x} \tau_{xy} = \tau_{xy} = \mu \left( \frac{\partial u}{\partial y} + \frac{\partial v}{\partial x} \right) \quad (3.42a)$$

$$\sigma_{yy} = -p + 2\mu \frac{\partial v}{\partial y} \tau_{yz} = \tau_{zy} = \mu \left( \frac{\partial w}{\partial y} + \frac{\partial v}{\partial z} \right) \quad (3.42b)$$

$$\sigma_{zz} = -p + 2\mu \frac{\partial w}{\partial z} \tau_{zx} = \tau_{xz} = \mu \left( \frac{\partial u}{\partial z} + \frac{\partial w}{\partial x} \right) \quad (3.42c)$$

By substituting these relationships into Equation 3.42a to 3.42c, we obtain the

**Equation of Motion** in *scalar* form along the three coordinate axes as

$$\rho g_x - \frac{\partial p}{\partial x} + \mu \left( \frac{\partial^2 u}{\partial x^2} + \frac{\partial^2 u}{\partial y^2} + \frac{\partial^2 u}{\partial z^2} \right) = \rho \left( \frac{\partial u}{\partial t} + u \frac{\partial u}{\partial x} + v \frac{\partial u}{\partial y} + w \frac{\partial u}{\partial z} \right) \quad (3.43a)$$

$$\rho g_y - \frac{\partial p}{\partial y} + \mu \left( \frac{\partial^2 v}{\partial x^2} + \frac{\partial^2 v}{\partial y^2} + \frac{\partial^2 v}{\partial z^2} \right) = \rho \left( \frac{\partial v}{\partial t} + u \frac{\partial v}{\partial x} + v \frac{\partial v}{\partial y} + w \frac{\partial v}{\partial z} \right) \quad (3.43b)$$

$$\rho g_z - \frac{\partial p}{\partial z} + \mu \left( \frac{\partial^2 w}{\partial x^2} + \frac{\partial^2 w}{\partial y^2} + \frac{\partial^2 w}{\partial z^2} \right) = \rho \left( \frac{\partial w}{\partial t} + u \frac{\partial w}{\partial x} + v \frac{\partial w}{\partial y} + w \frac{\partial w}{\partial z} \right) \quad (3.43c)$$

The equivalent *vector* form as in the Equation 3.44.

$$\rho \vec{g} - \nabla p + \mu \nabla^2 \vec{V} = \rho \frac{D\vec{V}}{dt} \quad (3.44)$$

which can simply be written as in Equation 3.45.

$$\frac{\partial \vec{V}}{\partial t} + (\vec{V} \cdot \nabla) \vec{V} = -\frac{1}{\rho} \nabla p + \vec{g} + \nu (\nabla^2 \vec{V}) \quad (3.45)$$

by expanding the material derivative for acceleration and dividing by density,  $\rho$ .

The above equation (in either scalar or vector form) are commonly called the **Navier-Stokes** equations for the incompressible Newtonian fluids.

### 3.2 Computational Fluid Dynamics (CFD)

As mention earlier, in order to solve a set of equations, we must have at least as many constraints as we have dependent variables. Examination of Equation 3.43a to Equation 3.43c shows that there are *four* dependent variables-pressures ( $p$ ) and three velocity components ( $u$ ,  $v$  and  $w$ ) defined in terms of *four* independent variables-time ( $t$ ) and three position coordinate ( $x$ ,  $y$  and  $z$ ) – but only *three* equations. However, by including the Continuity equation, we obtain the fourth constraint, which will allow us to uniquely define each dependent variable. Mathematically, Equation 3.22 (Continuity Equation) and Equation 3.44 (Navier-Stokes Equation) are first-order and second-order partial differential equations, respectively. Furthermore, Equation 3.43a to Equation

3.43c is nonlinear because of the presence of product terms such as  $u \cdot \partial u / \partial x, v \cdot \partial u / \partial y, w \cdot \partial u / \partial z$ , etc. Unfortunately, no exact analytical solution has been taken. One is to first simplify the equations until they have a mathematical form in which there is a solution. For example, we could assume a steady, two-dimensional flow (say, in the  $x$ - $y$  plane) along one axis (say, the  $x$  axis), which would eliminate all terms involving  $\partial / \partial t$  and two of the velocity components. If the flow were in the  $x$  direction only, the Equation 3.22 could reduce to

$$\frac{\partial u}{\partial x} = 0 \quad (3.46)$$

Or

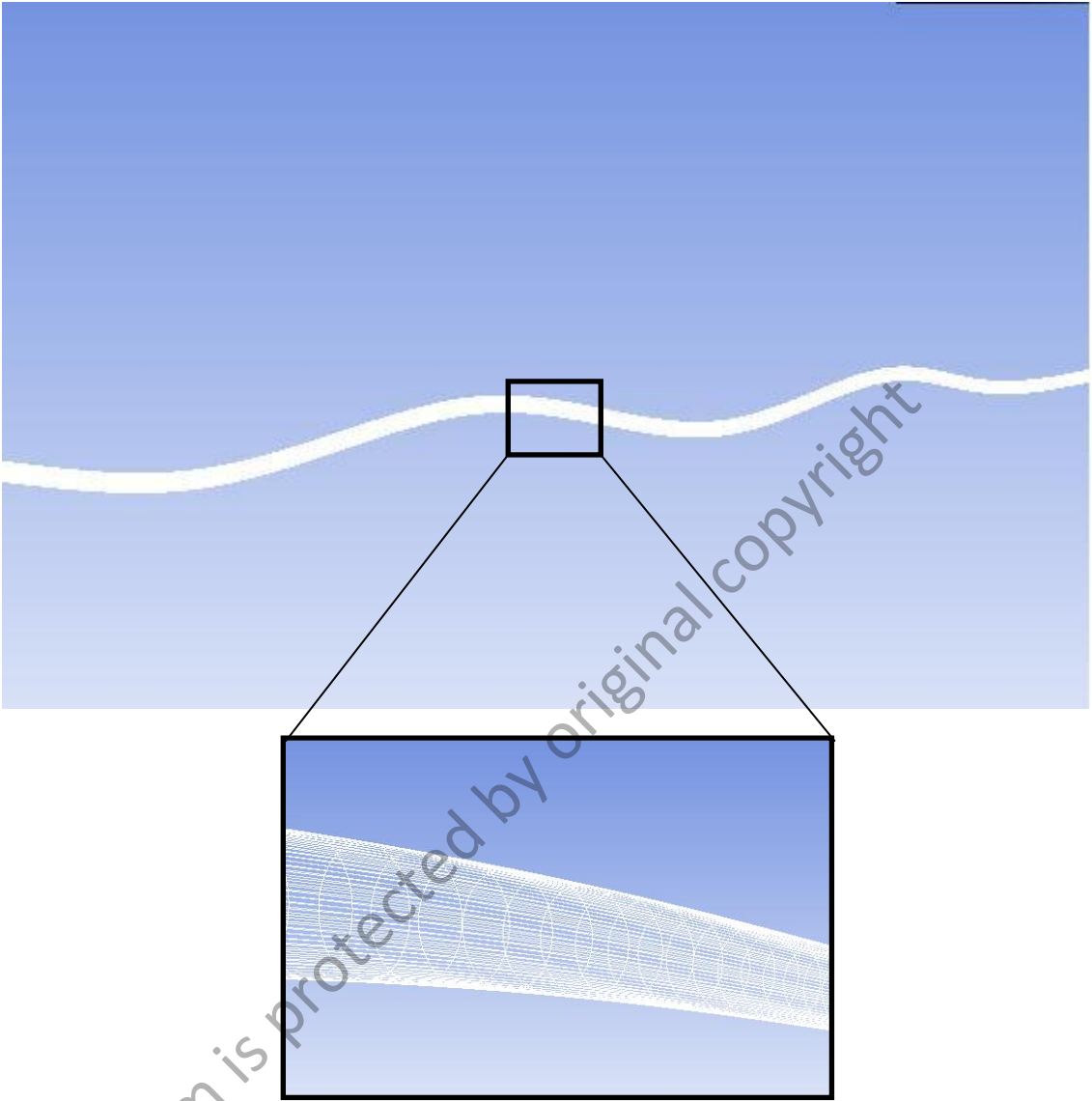
$$u = f(y) + C \quad (3.47)$$

Where  $C$  is the integration constant, Equation 3.54 will be reduced to

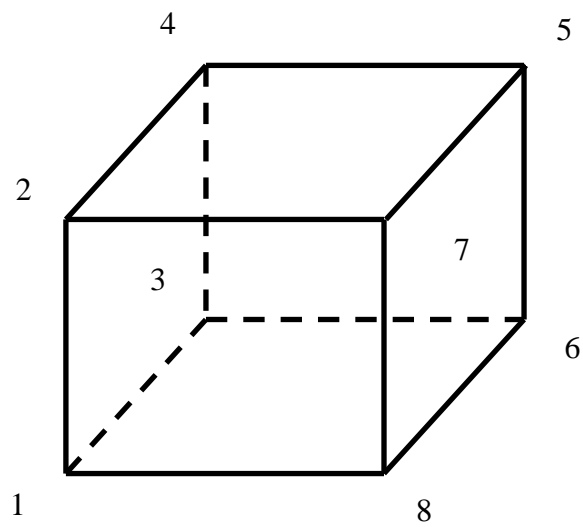
$$\frac{\partial p}{\partial x} = \mu \left( \frac{\partial^2 u}{\partial y^2} \right) \quad (3.48)$$

Here, it is now possible to solve  $u(y)$  as an explicit function of  $p$ .

The other approach taken is to solve these equations numerically. This approach is more complex, but it provides the ability to solve problems without making unrealistic simplifying assumptions. The basic technique is to first sub-divide the flow into many small regions, or **cells** (Figure 3.11b), over which the governing equations are applied. Rather than using the differential form of the equations, however, they are rewritten in algebraic form in terms of changes that occur in variables due to the incremental changes in position and time. Solutions are then obtained locally at the specific locations or **nodes** (Figure 3.8b), on the finite elements across a **mesh** (Figure 3.8a) of element Figure 3.8 and Figure 3.9.



(a)



(b)



Face	Associated Nodes
Face 1	1-2-3-4
Face 2	3-4-5-6
Face 3	5-6-7-8
Face 4	1-2-7-8
Face 5	2-4-5-7
Face 6	1-3-6-8

(c)

Figure 3.8(a) The CFD Mesh for the saphenous vein graft model with a kink failure. (b) Hexahedron cells that applied on the saphenous vein graft model (c) Table of Face and Node numbering for the Hexahedron cells

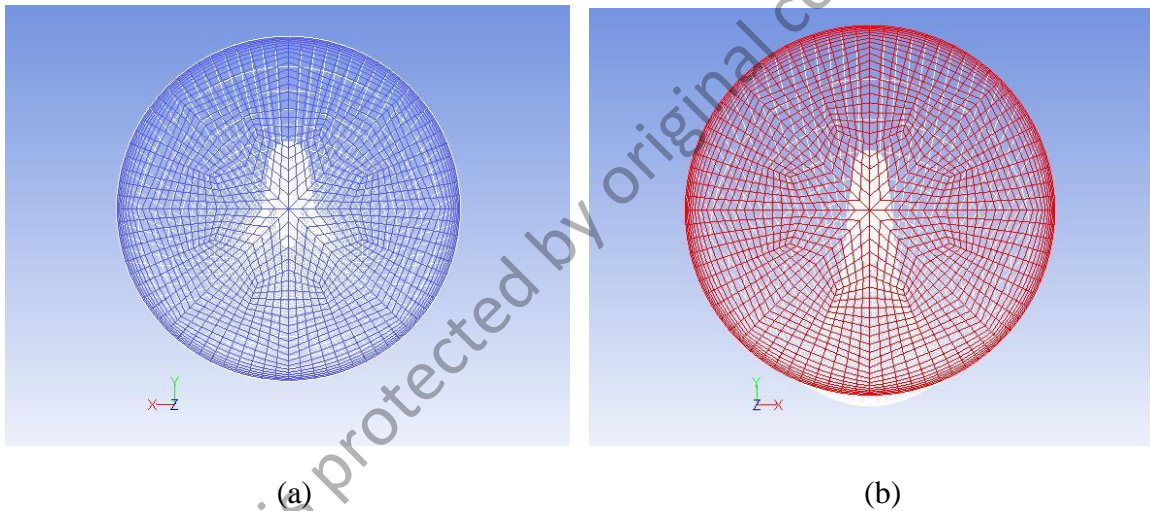


Figure 3.9: The fine meshes are employed in the area of the saphenous vein graft in order to obtain more accurate result in this region of interest. For this research interest region is at the wall of the vein graft model ;(a) Proximal or Inlet region and (b) Distal or Outlet region.

This set of solutions is updated at subsequent time intervals over the entire mesh until some acceptable levels of accuracy, or **tolerance**, are achieved based upon the convergence between the successive values of certain output variables. Obviously, this can be a very detailed and time- consuming process depending upon the complexity of the geometry being analyzed and the initial and boundary conditions imposed. Furthermore, additional features are sometimes included in the equations to allow for

the simulation of Non-Newtonian fluids and the turbulent flow conditions, for example. While it is always important to validate such results, these **computational fluid dynamic** (CFD) software programs are increasingly being used to solve challenging biomedical flow problems unapproachable by any other means.

### **3.3 Computational Simulation Details and Modeling**

#### **3.3.1 Computational Simulation Details**

Computational simulation of blood flow in ideal and irregular of the vein graft models are executed via ANSYS FLUENT V13 and the discretization scheme is based on the finite volume method. A structured hexahedron mesh has been utilized for nodes generation due to a better meshing yield and it is also more suitable for ideal and irregular vein formation models by applying the GAMBIT V2.4.6. Meshing is a process of engagement of sub-domains or to generate small cells into ideal and irregular of the vein graft models to become as an interlock by using a hexahedron cell or element. This is amenable to solve the governing equations through created grids. The meshing step begins by setting and generating the coarse grids to ensure that there are no problems in the first place of generating the grids, and then followed by generation of successive smaller grids at the interest region like in this research, the wall region is confirmed as an interest region for the wall shear stress study. This is because the first time meshing can reflect a significant effect on the results due to low mesh density (Ferziger&Peric, 2002; Shaw, 1992). However, the skewness value

should also be considered as to achieve successive in meshing. Skewness is defined as the difference between the shape of the cell and the shape of an equilateral cell of the equivalent volume. The highly skewed cells can decrease accuracy and destabilize the solution. Each element has a value of skewness between 0 and 1, where 0 represents an ideal element. In the GAMBIT V2.5.6, the skewness that value below than 0.5 is an acceptable value in meshing. The predicting equation of the blood flow through the vein graft models have to be converged and the meshing required to achieve the Grid Independent state. The Grid Independent state can be achieved by observing the results that do not change for further refinements of the grid (Tu et al., 2008).

Furthermore, a simulation by the vein graft failures has been introduced in this work. This is to achieve high accuracy and Grid Independence, where the ideal and irregular vein graft models have been remodeled to small size and more cells. Hence, the computations for all models are executed case-by-case as illustrated in Figure 3.10.






Failure Case	Model	Failure Detail		
		Case	Internal Diameter Mismatch Ratio, $(d_{\text{artery}} : d_{\text{vein}})$	Amplitude of two cycled sinusoidal wavy vein, cm
Ideal Straight		Ideal	1:1	0
Internal diameter mismatch	 	Case 1	1:1.1	0
		Case 2	1:1.2	0
		Case 3	1:1.3	0
Over length kink	 	Case A	1:1	0.05
		Case B	1:1	0.10
		Case C	1:1	0.15

Figure 3.10 Table of the vein graft models

Convergence can be easily achieved too due to density of the meshing increased in the vein graft model. A reasonable convergence solution for the iterations has been set for both mass and momentum, with residual level being below  $1 \times 10^{-6}$ .

Based on clinical diagnostic and surgical results, the real vein graft is in cylindrical geometry. As our objective to investigate our model close to *in-vivo* vein graft, the ideal and irregular formation of the vein graft model has been designed and created them in three dimensions cylindrical geometry. Furthermore, we can investigate any part of interest in  $x$ ,  $y$  axes and even in  $z$  axis of the vein graft models compared to

the two dimensional analysis that limited into two axes only,  $x$  and  $y$  axis. In this circumstance, the computational effort or the central processing unit (CPU) time occurred due to direct involvement of the three axes. Therefore, several assumptions are applied in this work to reduce the computation time, such as:

1. No heat transfer function applied at the blood flow through the vein graft model
2. No backward flow function activation at distal or outlet region of the vein graft model
3. Flow is fully developed at the inlet region which means no user define function applied for parabolic profile flow

However, we still extrude our vein model length in order to allow the blood flow to become fully developed since no user define function applied as illustrated in Figure 3.11. As a solution, the inlet region in monitoring the flow is set right after the blood flow become a fully developed flow. A fully developed flow is calculated based on the entrance length ( $L_e$ ) of a pipe channel as cited by Krishnan B. Chandaran et al. (2007) (Figure 3.11). Typical entrance lengths are given by

$$\frac{L_e}{D} = 0.06 Re \text{ for laminar flow} \quad (3.49)$$

where  $D$  and  $Re$  are the pipe diameter and Reynolds number respectively.

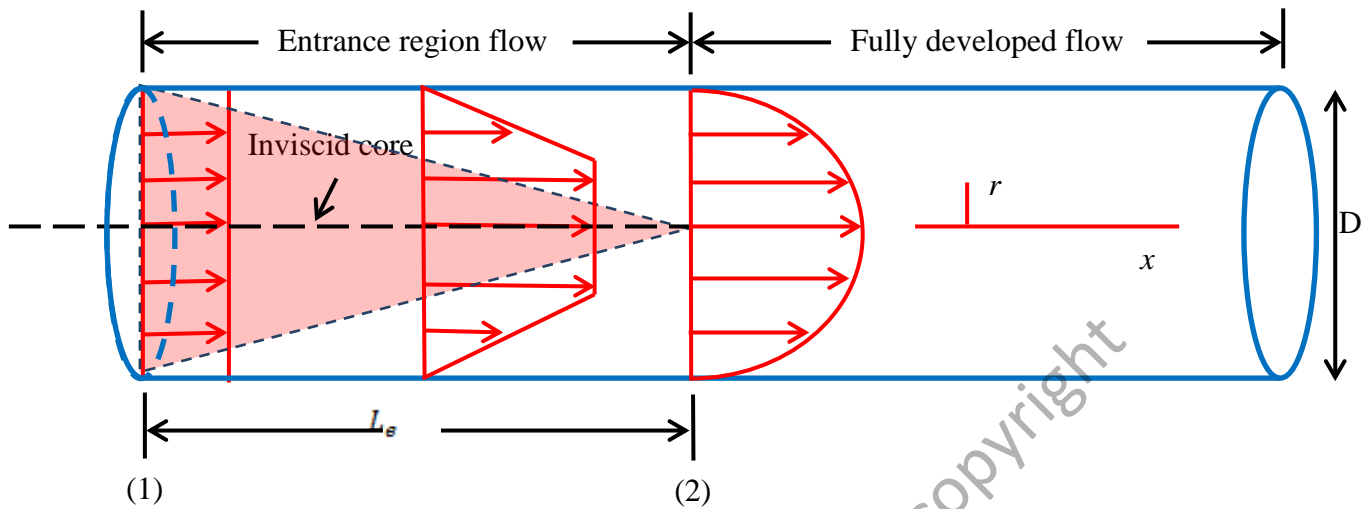


Figure 3.11 Entrance region, developing region and fully developed in the vein graft model

Once the fluid reaches the end of the entrance region at Section (2), the flow is simpler to describe because the velocity is a function of only the distance from the pipe centerline,  $r$  and independent of  $x$ . Hydraulically, the entrance length is very important because the transport properties such as centerline velocity or maximum velocity, pressure gradient between the proximal and distal of the vein graft model and the wall shear stress impact on the vein graft model depend strongly after the blood flow over than this entrance length region.

### 3.3.2 Fluid Mechanics in a Vein Graft Model

Most of the blood flow in the human circulation occurs within tubular structures such as arteries, capillaries and vein as well. For that reason, the study of fluid mechanics in a straight tube is of particular interest in biofluid mechanics. Even

though the human vasculature is not geometrically a series of straight tubes of constant diameter, results from this analysis do provide good estimates or starting points for further evaluation. In this chapter, there are several definitions of terms, which are relevant to common blood flow conditions.

Based on clinical results, the circulatory system is pulsatile in most regions like the systemic arteries and the microcirculation. The unsteady term for flow type is very general and refers to any flow type that is simply and not constant. The pulsatile flow can be defined as the flow that has a periodic flow behavior and a net directional blood flow motion over cycle (i.e., the average flow is  $> 0$ ). On the other hand, the oscillatory flow means the flow has periodic flow behavior but oscillates back and forth without a net forward or reverse output (i.e., the average flow  $\leq 0$ ). The fact of the unsteadiness type of blood flow is well known. Describing the principles of blood flow under more simplified condition is very helpful before furthering to complex physiologic environments. The simplest case to consider, therefore, is that of steady state blood flow type of Newtonian fluid through a straight, rigid, circular tube aligned in a horizontal position (Figure 3.12)

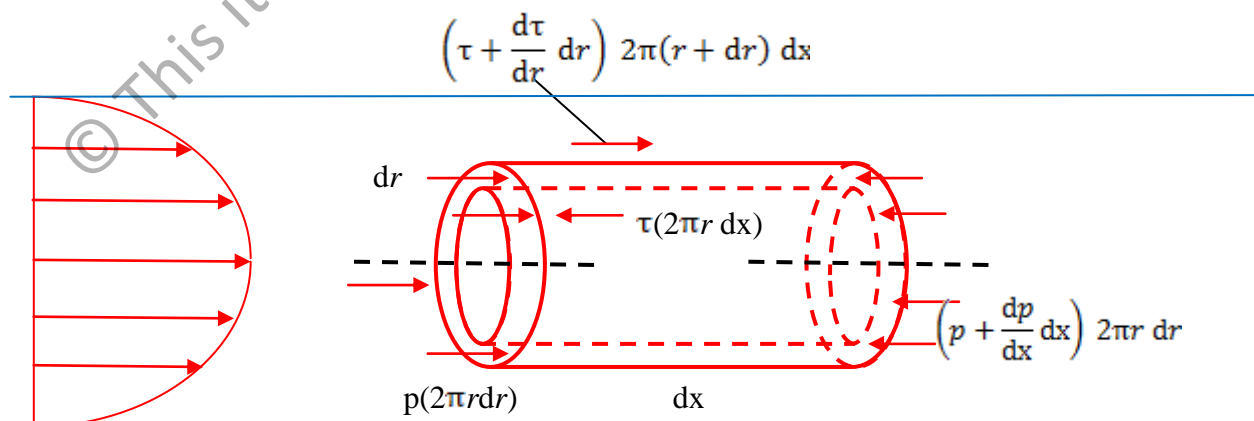


Figure 3.12 Force balance for steady blood flow through an ideal straight, horizontal, vein graft model

### 3.3.2.1 Blood Flow Stability and Related Characteristics

The nature of flow of a Newtonian fluid in a straight, rigid, circular tube is controlled by the inertial (accelerating) and the viscous (decelerating) forces applied to the fluid elements. When the *viscous* forces dominate, the flow is called **laminar** and is characterized by smooth motion of the fluid. The laminar flow can be thought of as if the fluid is divided into a number of layers flowing parallel to each other without any disturbances or mixing between the layers. On the other hand, when the *inertial* forces strongly dominate, the flow is called **turbulent**. Here, the fluid exhibits a disturbed, random motion in all directions, which is superimposed on its repeatable, main motion.

#### 3.3.2.1.1 Steady State Laminar Blood Flow in a Vein Graft Model

The key characteristic of the laminar flow is that it is well organized and very efficient, whereas the turbulent flow is chaotic and accompanied by high energy losses. Therefore, the turbulent flow is undesirable in the blood circulation because of the excessive workload it would put on the heart and also because of potential damage to the blood cells. A helpful index used to determine whether the flow in a tube or turbulent is the ratio of the inertial forces to the viscous forces. This ratio is classically known as the **Reynolds number** ( $Re$ ), which is dimensionless since both terms have units of [F]. It is defined as

$$Re = \frac{\text{Inertial forces}}{\text{Viscous forces}} = \frac{\rho V d}{\mu} \quad (3.50)$$



Where  $\rho$  [ $\text{kg}/\text{m}^3$ ] is the density of fluid,  $V$  [ $\text{m}/\text{s}$ ] is the average velocity of the fluid over the cross section of the tube,  $d$  [ $\text{m}$ ] is the tube diameter, and  $\mu$  [ $\text{kg}/\text{m} \cdot \text{s}$ ] is the dynamic viscosity of the fluid. Although the inertial forces obviously begin to dominate for  $Re > 1$ , it has been determined experimentally that in a smooth-surfaced tube, the flow is laminar for all conditions where  $Re < 2100$ . In this research, the blood flow has been calculated and recognized as laminar blood flow type. This means that the turbulence flow characteristic should be ignored. Furthermore, if the tube is long enough to have stabilized any entrance effects (Figure 3.12), the velocity profile then takes on a parabolic shape and the flow is called a *fully developed* laminar flow.

In section 3.1.5, we discussed the principle of Conservation of Momentum and derive the Navier-Stokes Equation. For the incompressible Newtonian flow, the equation of motion in vector notation given by Equation 3.55

$$\frac{\partial \vec{v}}{\partial t} + (\vec{v} \cdot \nabla) \vec{v} = -\frac{1}{\rho} \nabla p + \vec{g} + \nu (\nabla^2 \vec{v}) \quad (3.51)$$

Where  $\vec{v}$  [ $\text{m}/\text{s}$ ] is the velocity vector,  $p$  [ $\text{Pa}$ ] is the pressure,  $\vec{g}$  [ $\text{m}/\text{s}^2$ ] is the gravitational acceleration,  $\rho$  [ $\text{N} \cdot \text{s}^2/\text{m}^4$ ] is density and  $\nu$  [ $\text{m}^2/\text{s}$ ] is the kinematic viscosity of the fluid, respectively.

If we apply these equations in cylindrical coordinates (Equation 3.52) to the case of steady flow in an ideal straight, circular, horizontal vein graft model (Figure 3.13),

$$\rho \left[ \frac{\partial v_z}{\partial t} + V_r \frac{\partial v_z}{\partial r} + \frac{v_\theta}{r} \frac{\partial v_z}{\partial \theta} + V_z \frac{\partial v_z}{\partial z} \right] = F_z - \frac{\partial p}{\partial z} + \mu \left( \frac{\partial^2 v_z}{\partial r^2} + \frac{1}{r} \frac{\partial v_z}{\partial r} + \frac{1}{r^2} \frac{\partial^2 v_z}{\partial \theta^2} + \frac{\partial^2 v_z}{\partial z^2} \right) \quad (3.52)$$

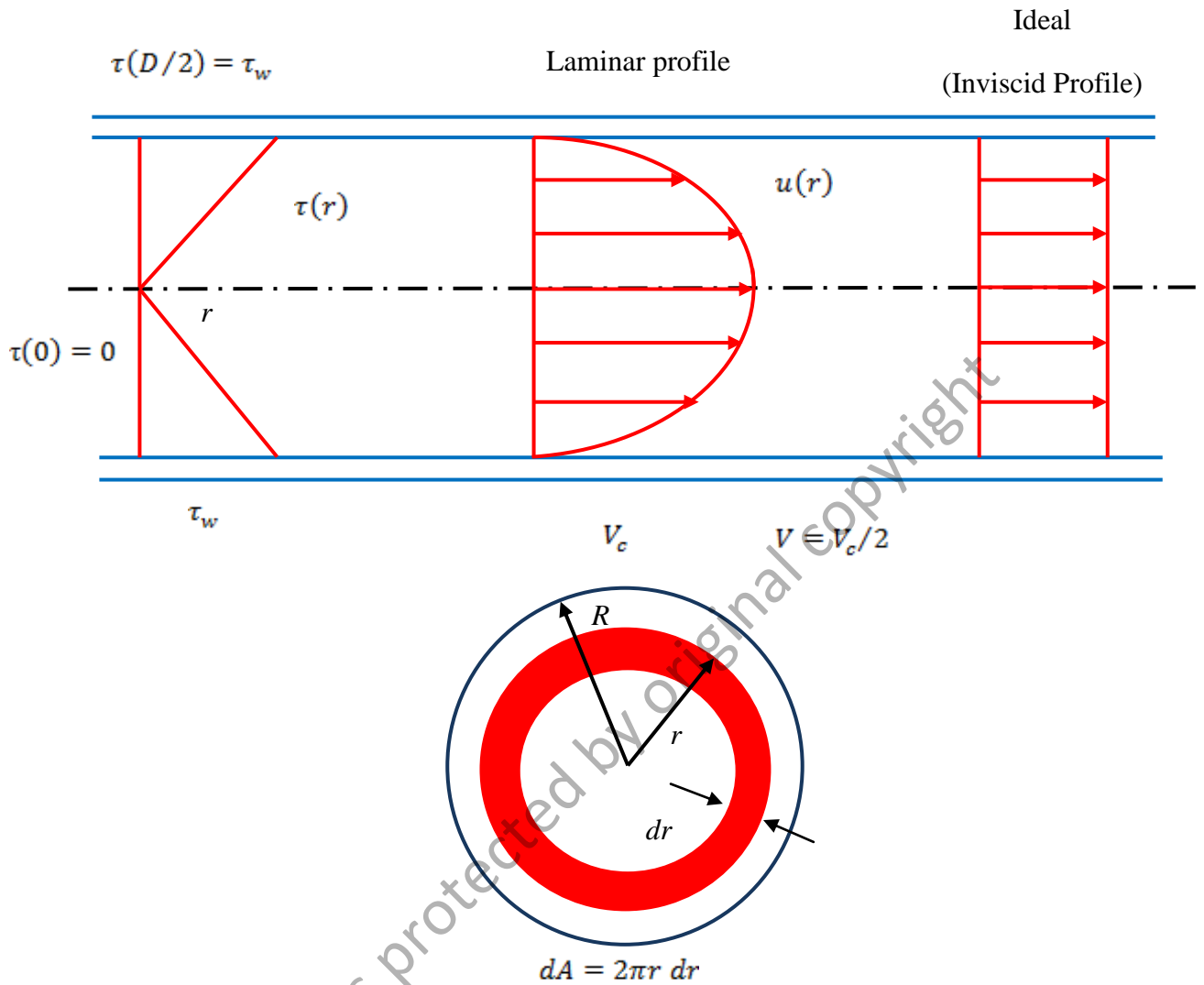


Figure 3.13 The shear stress distribution within the fluid in an ideal straight vein graft model (laminar flow) and typical profiles

Then the momentum balance in the  $z$  (axial) direction reduces to

$$-\frac{\partial p}{\partial z} + \mu \left[ \frac{1}{r} \frac{\partial}{\partial r} \left( r \frac{\partial v_z}{\partial r} \right) \right] = 0 \quad (3.53)$$

since the time rate of change (i.e.,  $\partial/\partial t$ ), secondary velocity (i.e.,  $V_r$  and  $V_\theta$ ), and circumferential velocity gradient (i.e.,  $\partial v_z/\partial \theta$ ) terms are zero. As a consequence, the conservation of mass balance results in  $\partial v_z/\partial z$  also being zero.

Rearranging terms yields

$$\frac{\partial p}{\partial z} = \mu \left[ \frac{1}{r} \frac{\partial}{\partial r} \left( r \frac{\partial V_z}{\partial r} \right) \right] \quad (3.54)$$

Since pressure is *only* a function of length and axial velocity is *only* a function of radius, however, this equation can be written equivalently in terms of ordinary derivatives, or

$$\frac{\partial p}{\partial z} = \mu \left[ \frac{1}{r} \frac{\partial}{\partial r} \left( r \frac{\partial V_z}{\partial r} \right) \right] \quad (3.55)$$

We can further observe that, for the two terms of the equation (i.e., Left Hand Side and Right Hand Side) to be equal for *all* values of independent variables  $r$  and  $z$  (each of which is only present in one of the terms), each term must be constant. Equation 3.55 then can be integrated twice to yield (Equation 3.56 and Equation 3.57)

$$\frac{\partial V_z}{\partial r} = \frac{1}{2\mu} \left( \frac{dp}{dz} \right) r + \frac{c_1}{r} \quad (3.56)$$

$$V_z = \frac{1}{4\mu} \left( \frac{dp}{dz} \right) r^2 + c_1 \ln r + c_2 \quad (3.57)$$

The constant terms,  $c_1$  and  $c_2$ , can be evaluated by applying known values of axial velocity at the specific boundary locations. For example,  $V_z = 0$  at  $r = R$  is due to the “non-slip” condition at the vein graft wall. The values of  $V_z$ , however, is not known at the vein graft model center,  $r = 0$ , although we can assume that it is a maximum at the point due to overall symmetry of the vein graft model. Thus, the appropriate boundary condition here is  $dV_z/dr = 0$ , which requires that  $c_1 = 0$  and which also constrains all velocities to be finite.

Evaluating  $c_2$  and substituting it into Equation 3.57 results in

$$V_z = \frac{1}{4\mu} \left( \frac{dp}{dz} \right) [r^2 - R^2] \quad (3.58)$$

If we replace the differential pressure gradient term by the pressure gradient along the *entire* ideal straight vein graft model,  $\Delta p/L$ , then the velocity variation, or “profile” in an ideal straight vein graft model is given by

$$V_z(r) = \left[ \frac{\Delta p R^2}{4\mu L} \right] \left[ 1 - \left( \frac{r}{R} \right)^2 \right] \quad (3.59)$$

or

$$V_z(r) = V_{\max} \left[ 1 - \left( \frac{r}{R} \right)^2 \right] \quad (3.60)$$

Where  $V$  [m/s] is the velocity of the fluid at distance  $r$ [m] from the center of the tube,  $V_{\max}$ [m/s] is the maximum (centerline) velocity,  $R$ [m] is the radius of the tube,  $d$ [m] is the diameter of the tube, and  $\Delta P$ [Pa] is the pressure drop along a length  $L$ [m] of the tube. By integrating this velocity profile over the tube’s cross section and dividing by two, we can obtain the average velocity

$$V_{\text{avg}} = \frac{V_{\max}}{2} \quad (3.61)$$

Since the flow rate in tube,  $Q$ [m<sup>3</sup>/s], is equal to the average velocity,  $V_{\text{avg}}$ , times the cross-sectional area, we can write

$$Q = V_{\text{avg}} (\pi R^2) = \frac{V_{\max}}{2} (\pi R^2) \quad (3.62)$$

Or

$$Q = \left( \frac{\Delta p R^2}{8\pi L} \right) (\pi R^2) = \frac{\Delta p \pi R^4}{8\pi L} \quad (3.63)$$

In terms of the tube diameter, this becomes

$$Q = \frac{\Delta p \pi d^4}{128 \mu L} \quad (3.64)$$

Solving for the pressure difference, we obtain

$$\Delta p = 128 \frac{\mu L Q}{\pi d^4} \quad (3.65)$$

which is commonly known as the **Hagen-Poiseulle Equation**.

The **Hagen-Poiseulle Equation** is very important equation to validate the results obtained from this simulation works. If the simulation results show exactly or nearly to the theoretical results, it means that our simulation works are correct.

#### 3.3.2.1.2 Blood Viscosity and the Wall Shear Stress impact on the Vein Graft Model

In the study of the vein graft vascular disease, one of the most important variables is the shear stress,  $\tau [N/m^2]$  of the blood flow, at the vessel wall ( $\tau_w$ ) of the vein graft model (Figure 3.6). The wall shear stress has considerable clinical relevance because it provides information about both the magnitude of both the blood exerted on the vessel wall as well as the force exerted by the fluid layer on another (Krishnan B. Chandran, et al, 2007). In healthy blood vessels, the shear stress is generally low ( $\sim 15$  to  $20$  dynes/cm<sup>2</sup>) and is not harmful to either the blood cells or to the cells, which lines up the inner surface of the vessel, called **endothelial cells**. The shear stress varies with the flow conditions (cardiac output, heart rate etc.) as well as with the local

geometry of the vessel (curves, branches, etc.). Excessively high levels of the shear stress caused, for example, by atherosclerosis lesion or artificial heart valves, may damage the red blood cells (a condition called “**hemolysis**”) or the endothelium of the vessel wall. Other abnormal shear stresses, such as the very low or strongly oscillatory shear stresses, may also change the biological behavior of some cells, such as platelets in the blood stream in which they become activated, leading to thrombus formation. These stresses may also act on endothelial cells lining the vessel wall, which then act as active compounds, leading to vessel constriction or wall hypertrophy.

Based on our earlier discussions, we can determine the shear stress for the laminar flow of Newtonian fluid as being linearly related to the shear rate ( $dV/dr$ ) according to Equation 3.3 as expressed in terms of cylindrical coordinates

$$\tau = \mu \frac{dV}{dr} \quad (3.3)$$

Where  $V$  is the velocity [m/s] at the radial position  $r$  [m] and  $\mu$  is the dynamic viscosity [N-s/m<sup>2</sup>] of the fluid. For laminar case, the wall shear stress can be determined from the force balance within a control volume if the pressure drop,  $\Delta p$ , is known along a length  $L$  of the ideal straight vein graft model (Figure 3.13)

$$\tau_{wall} = \frac{d \Delta p}{4 L} \quad (3.66)$$

As mentioned earlier, both viscous and shear stresses, if large enough, can potentially activate or lyse (i.e. rupture) the blood cells. However, the origin and, consequently, the scale of both viscous and shear stresses are different. The viscous shear stresses act on a molecule scale, i.e., they arise from the tendency of one molecule to remain in close proximity to its neighbor. This is quantified in fluids

through the measure of their “viscosity”. As the viscous stresses act on a scale much smaller than the diameter of a blood cell (in the order of few  $\mu\text{m}$ ), the blood cells will always experience the viscous shear stress if one is present.

### 3.3.3 Boundary Conditions

Boundary conditions are the sets of properties or conditions that are defined at every surface of ideal straight and irregular formation of the vein graft model. This defining process is one of the most important stages in computation in order to simulate the blood flow model numerically. The simulation will lead to a wrong solution if it is wrongly specified as erroneous sets of the boundary condition (Versteeg et al., 1995; Tu et al., 2008). The setting of the following boundary conditions is a common practice in the vein graft modeling or the vein graft wall bounded flow. A Newtonian fluid, nonslip at the wall of the vein graft model, the laminar blood flow, the steady and pulsatile flow, the vein graft model as cylindrical shape, the vein graft model as a rigid body and blood flow are types of boundary conditions that need to be specified at each case of the vein graft models in order to solve the blood flow problems.

## CHAPTER 4

### RESEARCH METHODOLOGY

#### 4.1 Introduction

The simulation work in engineering field has become well established for further engineering analysis. However, the outcomes of simulation works have always being argued. Due to this, the simulation work must be validated first before any results can be established. Hence, in this chapter, the study of simulation algorithms and the integrity of its results are carefully validated against peer reviewed experimental works. The experiment had been performed by Tzu-Ching et al. (2011) in measuring the red blood cells velocity in the capillaries of finger nail-folds. More details on this experiment will be discussed in the following subchapter. Further information on this experiment is discussed in the following subtopic. The thesis models, as laid in the proceeding chapter have been utilized in this validation work to investigate the blood flow phenomena in irregular formation of the vein graft models. Those models are carefully validated with an error of 1.5% which is within acceptable limits. Therefore, this validation will save and set as a benchmark in meshing to use the models and carry out further investigation for blood flow in the irregular vein graft models. Besides, case by case simulation methods has been introduced to achieve higher accuracy in results as the results do not show any significant changes in velocity with further refinements



in the grids. Finally, the boundary conditions in this validation simulation works are also included from the experimental work.

## 4.2 Simulation Procedures

First of all, an ideal straight vein graft model must be drawn in the GAMBIT Geometry Design which is the meshing software and followed by mesh generation. The GAMBIT Geometry Design has also been applied in designing every case of irregular formation of the vein graft model. Each vein graft model was examined for mesh quality especially the skewness range of the cells. In GAMBIT Geometry Design software, the skewness range of the cells must be below than 0.6. Otherwise, the error will occur when executing the geometry in the ANSYS Fluent Software. After the mesh generation, the vein graft models are ready for computation process. (Please refer Appendix A)

The procedure begins with the definability and initialization of physical boundary conditions by the ANSYS Fluent Software pre-processing tool. In this initialization process, the design problems have to be carefully initialized with specific boundary conditions according to the design problems. Next, the designed problems are ready to be solved iteratively by the ANSYS Fluent-Solver tool with appropriate equations. In this study, both the steady and pulsatile flow function have been utilized at ideal straight and irregular formation of the vein graft models while preserving the same boundary conditions for the designed vein graft models. This is to obtain the different results between this ideal straight and the irregular formation of the vein graft

models. Finally, the results are analyzed at the post-processing (Please refer Appendix B). The entire flow of the process for this simulation sequence is illustrated in Figure 4.1.

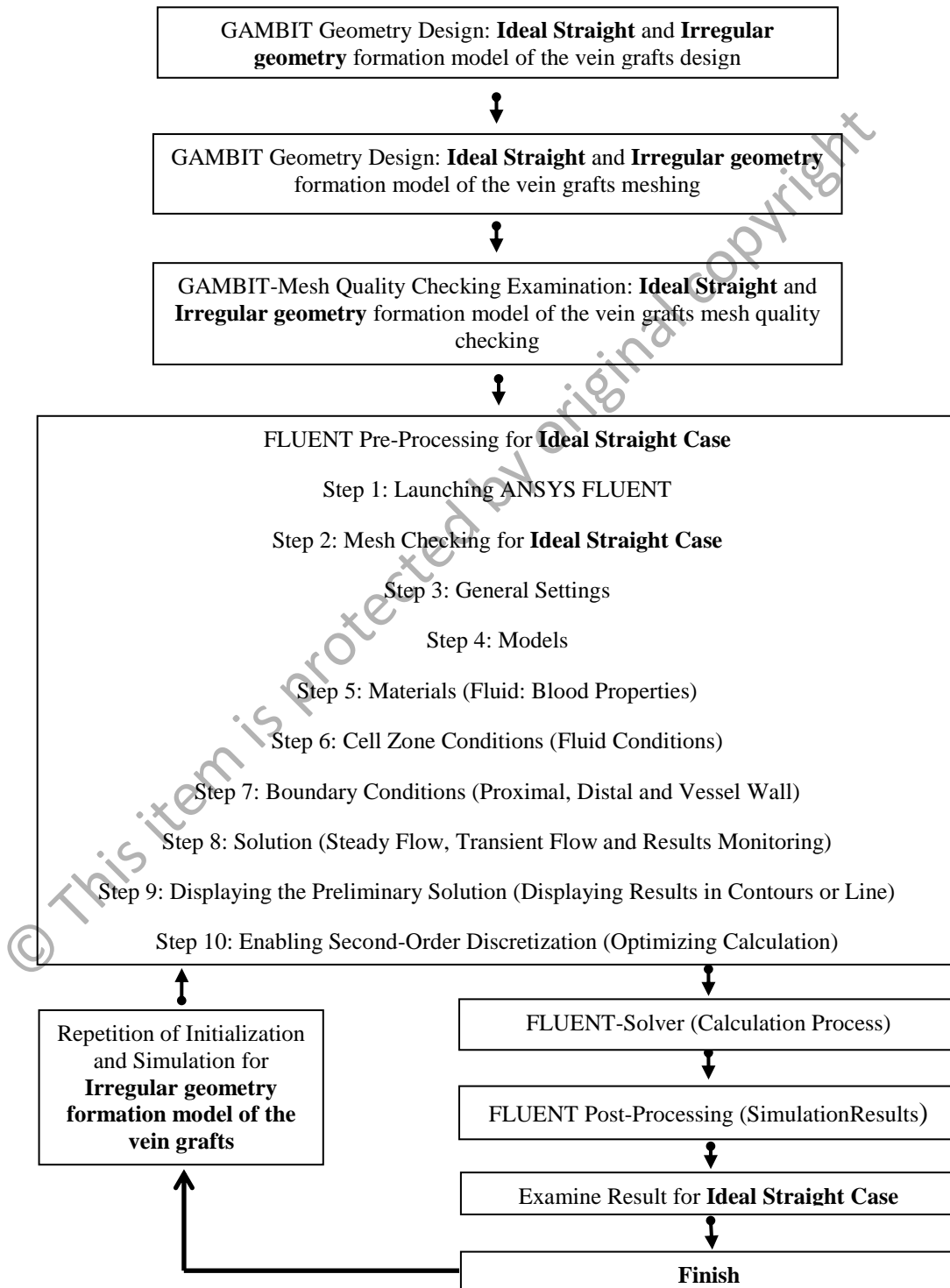


Figure 4.1 The entire flow of the process for simulation work

### 4.3 Validation Basis

The work of Tzu-Ching Shih et al. (2011) concerns the measurement of the red blood cells velocity in the capillaries of finger nail-fold by applying the computational fluid dynamic method. The two-dimensional captured capillary images were reconstructed to three dimensional models by assuming circular cross sections. The vessel walls were also assumed as the non-slip walls. The red blood cells velocity that calculated by the OFE (Optical Flow Estimation) was used in their experiment as a reference fluid or yardstick in order to measure and compare the red blood cell velocity that calculated by the CFD. The calculated red blood cell velocities of various grid sizes in meshing were almost identical to each other at each distance, indicating that the CFD numerical results are grid independent. Based on their experiment, it is noted that the CFD method can provide a reasonable accuracy to the red blood cells velocity in the finger nail-fold capillaries.

The blood vessel model that they had used was assumed as circular cross sections with the capillary diameter ranging from 8.98 to 21.72  $\mu\text{m}$ , and about 1 cm in length. Other blood flow properties that they had set in their experiment were an inlet flow and Reynolds number of 191.70  $\mu\text{m/s}$  and 0.003, respectively. From the calculation, the Reynolds number showed below than 1 most certainly describes the flow of fluids as laminar blood flow. The non-slip boundary conditions were applied on the vessel walls and a uniform velocity profile was used at the inlet. The blood was approximated as a Newtonian fluid with a density of 1050  $\text{kg/m}^3$  and a dynamic viscosity of 0.035  $\text{kg/m/s}$ . Figure 4.2 shows the outlet velocities with different element numbers obtained from their experiment. Their experiment results shows a good

agreement with their estimated analytical results, suggesting that the CFD method and the incompressible Navier–Stokes equations can be used to predict the blood flow behavior of homogenous fluid within a blood vessel in the finger nail-fold .Therefore, their method has been used in this work to validate the simulation algorithms, the model equation as well as the boundary conditions.

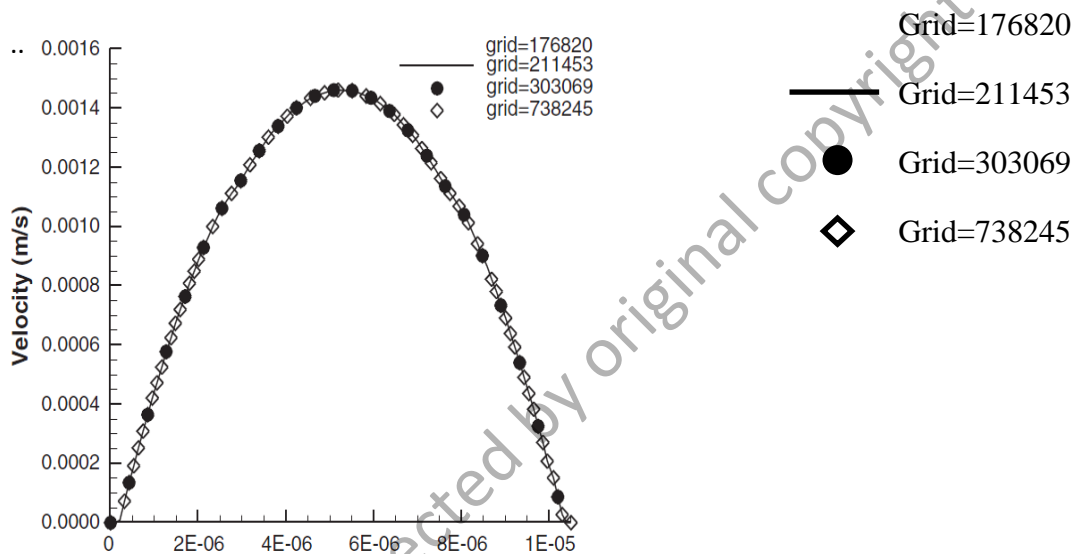


Figure 4.2 The velocity profile at the vessel outlet with different element numbers. The profile was observed at (Tzu-Ching Shih et al., 2011).

#### 4.4 Simulation Validation Details



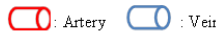


##### 4.4.1 Case by Case Simulation

In order to achieve the grid independence state, simulation by cases has been introduced in this meshing work. This method has led to achieve the highest number of nodes in the designed irregular formation of the vein graft model. The error occurred if

more nodes are created such as in length kink of the vein graft model, only 443 681 nodes were accepted. As shown previously in Figure 3.12, the finer meshes are employed in the area of the saphenous vein graft in order to obtain more accurate result in this region of interest. Furthermore, the spacing between two nodes can also be reduced orderly, at the same times the numbers of nodes in the total vein graft models increase. To add further, this research interest region is at the wall of the vein graft model. In addition, this particular method is very suitable for the vein graft models with longer length as more accurate results can be obtained (Rory F. Rickard, 2009). Hence, the simulation work case by case is considered suitable for this validation work since the microchannel used in Rory F. Rickard, (2009) and of Tzu-Ching Shih et al.' (2011) experiments. The amount of larger number of nodes in the vein graft model should lead to better approximations or more accurate results. Simultaneously, the convergence criterion can be easily achieved in calculating due to the higher density of meshing in the vein graft model.

Table 4.1 shows the details of the simulation case by case that have been performed to simulate the experimental work in order to achieve the grid independence. These are ideal straight vein graft model, three cases of mismatch vein graft model and three cases of kink vein graft model simulation which have been performed. Further details on the accuracy of the analysis are discussed in the following subtopic of meshing.

Table 4.1:Details of simulation based on cases.

Case	Model	Geometry Detail				
		Case	Internal Diameter,cm		Vein Length, cm	Amplitude of two cycled sinusoidal wavy vein, cm
			Artery	Vein		
Ideal Straight		Ideal	0.10	0.10	10	0
Internal diameter mismatch	 	Case 1	0.11	0.10	10	0
		Case 2	0.12	0.10	10	0
		Case 3	0.13	0.10	10	0
Over length kink	 	Case A	0.10	0.10	10.01	0.05
		Case B	0.10	0.10	10.04	0.10
		Case C	0.10	0.10	10.10	0.15

#### 4.4.2 Meshing



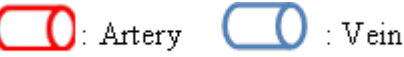


The first step of the pre-processing step in the ANSYS Fluent is the creation of geometry of the vein graft model. After that, the created geometry of the vein graft models will proceed to the meshing stage. Those works were done in GAMBIT. Meshing is a process of engagement of the sub-domains or to generate small cells into ideal and irregular of the vein graft models to become an interlock by using a hexahedron cell or element. This is a requirement to solve the governing equations

through created grids into the vein graft model. At the beginning, the meshing process starts by generating vertices as a guidance to generate the grids, and then followed by the refinement of successively smaller grids. The fine meshes are employed in the area of saphenous vein graft in order to obtain more accurate results in this region of interest. For this research, the interest region is at the wall of vein graft model. This is because the first time meshing can reflect a significant effect on the results due to low mesh density (Ferziger J.H, 1992).

As stated previously, the vein graft models with a length range between 10 cm and 10.10 cm have to be refined with the objective of increasing the number of nodes in the vein graft models where hexahedron cells are utilized since this produces better meshing yields in the vein graft models especially at the wall of the vein graft models even for more complex geometries.

Table 4.2 shows the summary of the total number of nodes and hexahedron elements that have been generated through the different subtopic meshing process.

Table 4.2 Total number of nodes and hexahedron elements

Case	Model	Case	Total number of nodes	Total number of hexahedron elements
Ideal Straight		Ideal	248 751	242 000
Internal diameter mismatch	 	Case 1	248 751	242 000
		Case 2	248 751	242 000
		Case 3	248 751	242 000
Over length kink	 	Case A	222 761	216 000
		Case B	443 681	432 000
		Case C	443 681	432 000

#### 4.4.3 Boundary Conditions

The boundary conditions for validation in this simulation works are carefully extracted from previous experimental works conducted by GJTangelder et al. (1986), Mette S. Olufsen, (2000), Christopher L. (2001), Sang-Wook Lee et al. (2003), Meena S. et al. (2006), Jung J. et al. (2008), Qin, Liu et al. (2008), Rory F. et al. (2009) and Tzu-Ching et al. (2011) to ensure their conditions is applied exactly the same into the this



simulation work. This is to accurately simulate and to attain reliable results required . Hence, the boundary conditions are as follows (Wilmer W. Nichols et al, 1998, Krishnan B. Chandran, 2007) :

1. The property of blood has been assumed as homogenous liquid and its viscosity is the same at all rates of shear. The particle of blood is well known as a suspension of particles, but it has been proven that, in the vessels in which the internal diameter is larger compared to the size of red blood cell, it behaves as Newtonian liquid. However, this assumption is applicable in tubes over than 0.5 mm radian. It is available for this research since the only tubes over than 0.5 mm internal diameter are applied.
2. The blood flow does not slip at the vessel walls. It is assumed that velocity is zero when  $r = R$ , which means that zero velocity at the vessel walls.
3. The blood flow is laminar which means the blood flow is parallel to the wall of the vessel. This assumption is not applicable in turbulent blood flow. However, it has been proven that we limit this study by dealing with the laminar blood flow only.
4. The rate of blood flow is at 'steady' state. It is only valid in steady state simulation cases but not for pulsatile (acceleration or deceleration) flow simulation cases.
5. The vessel is cylindrical in shape. There are two opinions on this assumption; first, the cross section of the vessel is circular and second, the vessel walls are parallel. Even though this vein graft models may be good approximation for most of the existing digital arteries and saphenous vein in the upper extremity circulation, the digital arteries and the vein grafts are more elliptical in shape. The digital arteries do not taper with their cross sections (Mette S. Olufsen,

2000). Thus, the general assumption of circular cross for the saphenous vein graft section without taper is a close to reality.

6. The rigid vessel wall and the diameter do not vary with the internal pressure. The arterial walls are more visco-elastic and dilated with the pulse pressure compared to the wall of veins. The interaction between the flowing blood and the dilatable arterial wall is an important factor in the description of the flow dynamics. Thus, the assumption of rigid walls in the model is also not valid. However, based on previous simulation work, the distensibility of the vessels will not affect the solution.
7. The length of the vessel model needs to be extended and compared to the region being studied. Theoretically, close to the proximal (or the inlet) of the vein graft model, blood has not yet become the flowed with the parabolic velocity profile characteristic of the laminar flow. The distance required to establish the steady form of flow is known as the 'entrance length', and here the Poiseuille's equation does not apply. We can conclude that, any result needs to be collected right after the entrance length of the vessel model.

The blood velocity in digital artery is calculated by Ying He et al. (2004) in the experiment is 6.25 cm/s for minimum velocity, 12.5 cm/s for mean velocity and 18.75 cm/s for maximum velocity. The internal diameter of digital artery is approximately about 1 mm (Ying He et al., 2004). Based on paper reviews, the velocity of blood flow through the vein graft must be exactly the same as the exercised artery to ensure the prolonging survival of the vein grafting. Therefore, the inlet velocity of 12.5 cm/s as the mean velocity is applied at the proximal of the vein graft model in all cases, ideal straight model and irregular formation of the vein graft models for steady state analysis.

For unsteady or pulsatile flow analysis, the User Define Function (UDF) containing 6.25 cm/s and 18.75 cm/s for minimum and maximum velocity is applied at the proximal in all cases (Please refer Appendix C). An interval time is set to be 4 seconds for one cycle of pulsatile (Ying He et al., 2004).

An absolute pressure of 1 atm is applied at the inlet region of the vein graft models as the patients are at the atmospheric pressure while ignoring the gravitational force and the energy equation.

#### **4.4.4 Grid Independence**

As stated previously, the Navier-Stokes Equations was used as the governing equations. Those equations have to be fully converged in order to get better results. However, based on literature studies, achieving the grid independence state is the only method in obtaining high accuracies. The grid independence state can be defined as an achievement when the results do not change for further refinements of the grid in the vein graft models. At the same time, the convergence in calculation also strongly depends on the mesh refinement of the vein graft models or in other words, how much smaller the grids are packed into the vein graft models. High density of grids are packed into the vein graft models, it helps to achieve the convergence quickly or required a minimum number of iteration in calculation. We can conclude that the convergence and grid independence states are quickly achieved based on the quality and quantity of the grid generated in the vein graft models (Rainald Lohner, 2008).

Figure 4.3 shows the grid independence test and accuracy that has been achieved for the simulated vein graft models. The resulting velocity profile for the Internal Diameter Mismatch Cases shows a huge discrepancy compared to other cases. This is because of the initial or normal speed that carried by blood flows from the wide artery vessels to the narrow vessels. The Ideal Straight and Over Length Kink Cases of the simulations do not show any significant changes in the velocity profiles. Further increment in the number of nodes in the vein graft models via simulation by cases, which also reduces the spacing size between nodes, leading to better approximation with higher accuracy. Hence, the results achieved the grid independence state. However, the errors happen in the simulated results for those cases where the error percentage is less than 1.48% as compared to the measured result (Ying He et. al, 2004) which is well within the 5% error limit. The computational fluid dynamics numerical software ANSYS FLUENT was applied. In the numerical solution algorithm as given by Fluent, the governing Navier-Stokes equations (linear momentum and conservation of mass) were solved rapidly. The equations are linear, steady and simple with several iterations of the solution loops, were needed before a solution result was fully converged. By applying this approach, the resulting algebraic equations for the dependent variables (the flow velocities) in each control volume were solved by the Least Squares Cell based on the linear equation solver and discretization method. The calculation was carried out by setting the convergence criteria as  $10^{-6}$ . The governing equations were calculated rapidly until calculations of all flow variables were converged on the HP workstation Z600 desktop (Intel Xeon, 4 GB RAM).

## 4.5 Validation

### 4.5.1 SteadyState Blood Flow Model

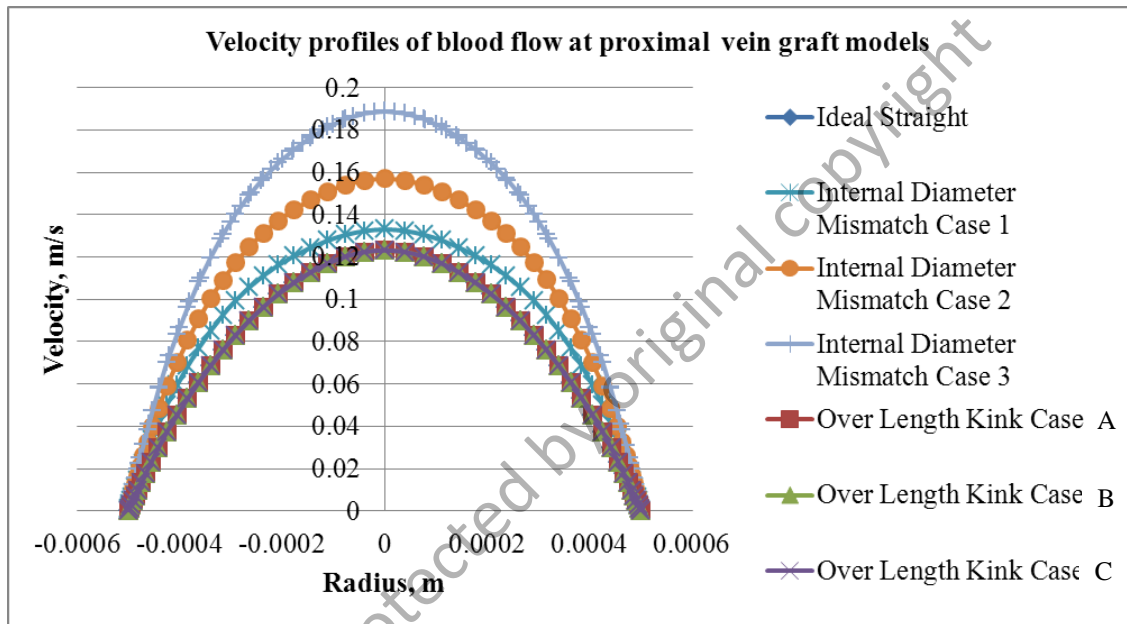


Figure 4.3 Grid independence tests

Figure 4.4 shows the comparison of the velocity profiles of blood flow through the vein graft models between the measurement and the simulation result of the steady state blood flow. The model has been simplified according to the previous simulation work to obey several experimental conditions such as laminar blood flow, Newtonian fluid, incompressible fluid, blood as homogenous liquid and it does not slip at the vessel walls. The simulation results of the velocity profile form have been monitored at the proximal, middle and distal of the vein graft models. Those profiles have also been compared to previous measured results (Ying He et al., 2004).

The measured velocity of blood flow in the finger digital artery from Ying He et al.'s (2004) experiment is about 0.125 m/s being 1.48% higher than the simulation result at 0.12315 m/s, which is well within the 5% error limit except for the mismatch cases. Thus, the observed velocity profile of blood flow in the vein graft models by the steady state flow model shows a very good agreement with the simulation data. It also shows the ability to produce better prediction on the blood flow in the vein graft models for low Reynolds number. Besides, the error percentages of each monitor region between the experimental and simulation works are shown in table 4.3. Based on this table, the error values obviously explain that the experiment value is much higher than the simulation values even for Internal Diameter Mismatch Cases. As stated previously, this is due to the initial or normal speed that carried by blood, flows from the wide artery vessels to the narrow vessels. However, a similar setting of meshes were set on that model of cases and validated. The steady state blood flow models have been methodologically validated by theoretical and simulation works. Thus, the vein graft models can be used for further investigations in the blood flow even in a steady state or pulsatile blood flow.

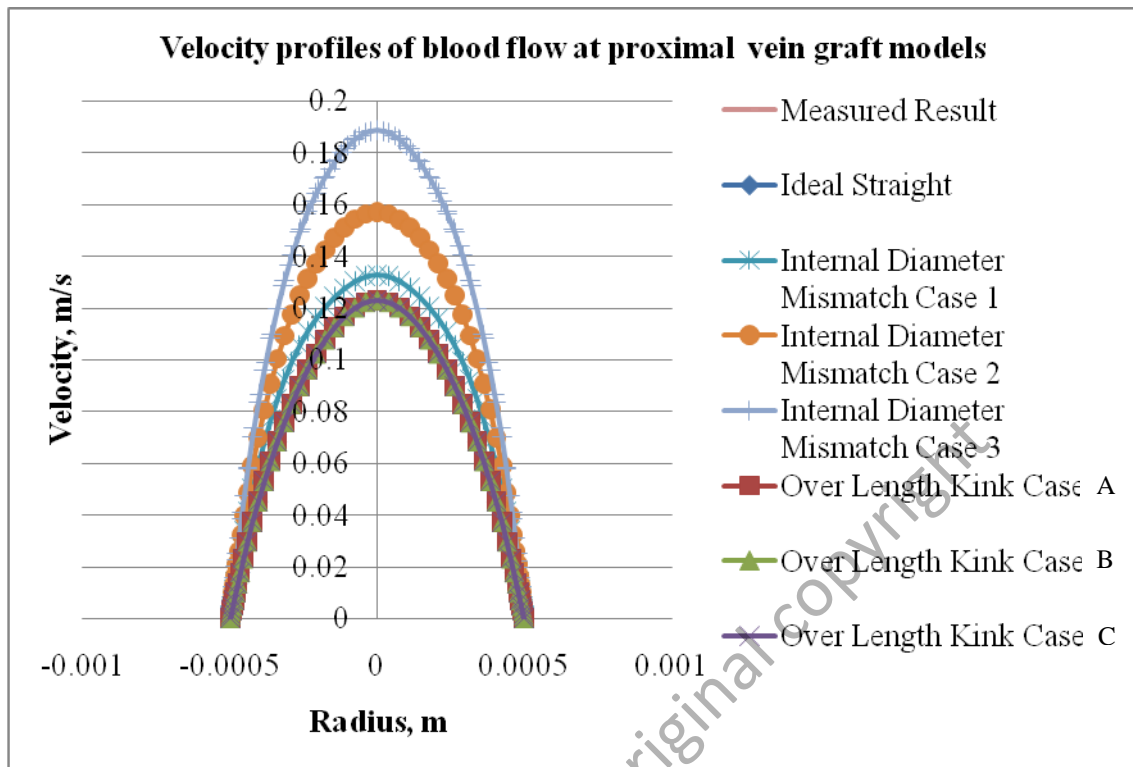







Figure 4.4 Comparison of velocity profiles between an experiment by Ying He et al. (2006) and the validation simulation of steady state blood flow model.

Table 4.3 Error percentage between experiment and simulation by the steady state blood flow model

Case	Model	Case	Error (%)		
			Proximal	Middle	Distal
Ideal Straight		Ideal	1.48	1.48	1.48
Internal diameter mismatch	 	Case 1	1.48	1.48	1.48
		Case 2	1.48	1.48	1.48
		Case 3	1.48	1.48	1.48
Over length kink	 	Case A	1.48	1.48	1.48
		Case B	1.48	1.48	1.48
		Case C	1.48	1.48	1.48

#### 4.5.2 The Pulsatile Blood Flow Model

The investigation of blood flow in an ideal straight and irregular formation of the geometry vein graft models were extended in the pulsatile blood flow function by using the same vein graft models that were previously applied in steady state cases. Figure 4.5 shows the comparison of the pulsatile velocity of blood flow between the Ying He et al.'s (2004) experimental and simulation by using laminar pulsatile of the FLUENT User Define Function. This validation is observed at the proximal of the vein



graft model crossing the center line of the sections, exactly as the location of previous simulation works (A. Jafari et al., 2009, Christopher L., et al., 2001, QinLiu et al., 2008, Rory F. Rickard et al., 2009, Sang-Wook Lee et al., 2003, Tzu-Ching et al., 2011, W. W. Jeong et al., 2009). The values of velocity, pressure gradient and WSS were observed right after 4 seconds because the stability was achieved on that time. The difference velocity of pulsatile blood flow through the vein graft models between measured and ideal straight results are 1.60% error. Thus, the observed blood flow velocity profiles of the pulsatile model also show a very good agreement with the experimental data. The error percentages for each monitor region (proximal, middle and distal) between the velocity profiles for the simulation works are illustrated in Table 4.4.

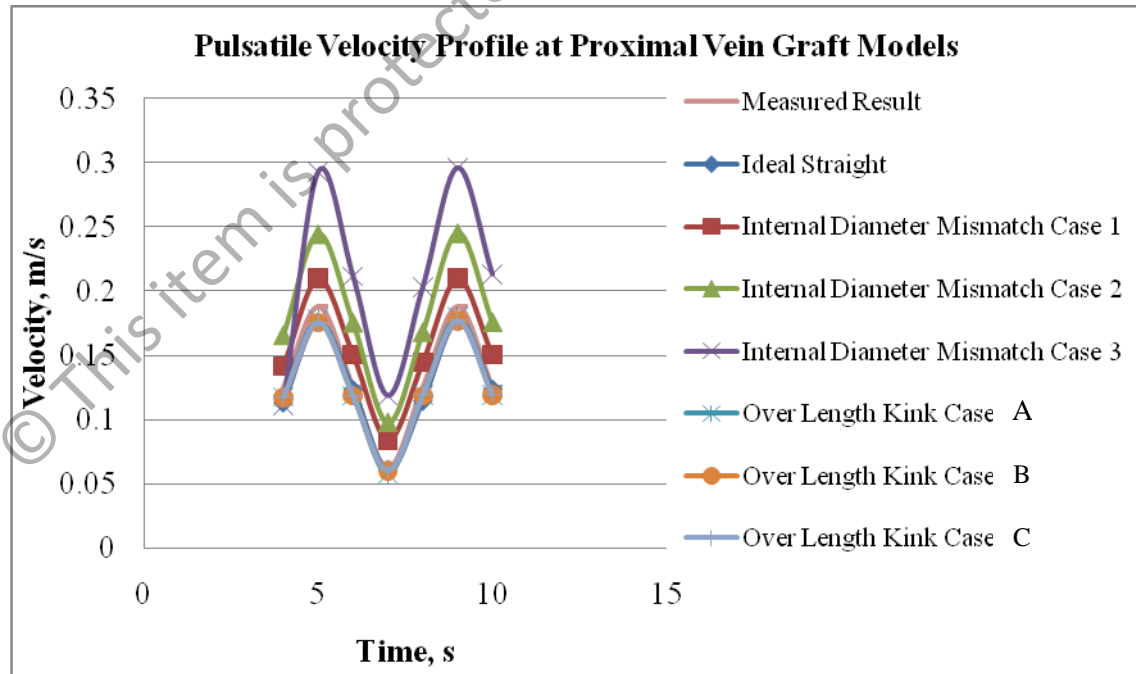

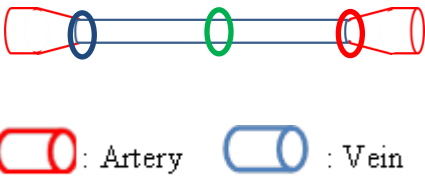

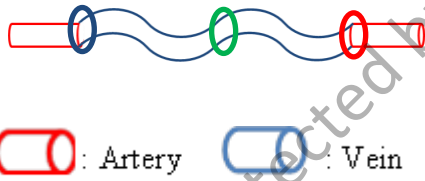



Figure 4.5 Comparison of pulsatile velocity profiles between measured result by Ying He et al. (2004) and validation simulation of the pulsatile blood flow models.

Table 4.4 Error percentage between the experiment and simulation by the pulsatile models.

Case	Model	Case	Error (%)		
			Proximal	Middle	Distal
Ideal Straight		Ideal	1.60	1.60	1.60
Internal diameter mismatch	 	Case 1	1.60	1.60	1.60
		Case 2	1.60	1.60	1.60
		Case 3	1.60	1.60	1.60
Over length kink	 	Case A	1.60	1.60	1.60
		Case B	1.60	1.60	1.60
		Case C	1.60	1.60	1.60

#### 4.6 Summary

The validation between the simulation works and the previous experimental works have been performed by utilizing both steady state and pulsatile models. Both models show a very good agreement to the approximate velocity profiles of blood flow in the vein grafts. The velocity profile error percentage between the experiment and the simulation at the vein graft models are 1.48% and 1.60% by the steady state and pulsatile models, respectively. Besides, the simulation by cases which has been

introduced in this work to achieve grid independence as well as higher result accuracies, shows promising achievement. Therefore, it can be concluded that, the simulation algorithms, the model equation as well as the boundary conditions used in this validation simulation works give promising results when compared to the measured results. Hence, these validated simulation algorithms, model equation, boundary conditions and the simulation by cases method form the benchmark upon which the basis to perform further simulations for the blood flow in the vein graft models.

© This item is protected by original copyright

## CHAPTER 5

### RESULT AND DISCUSSION

#### 5.1 Introduction

In order to address the hypothesis in the introduction, computations are performed for irregular formation of the vein graft models. The dimensions of irregular formation of the vein graft models are classified into two major cases, the internal diameter mismatched and over length kink of the vein graft models.

For the dimension of internal diameter mismatched vein graft models, 1 mm internal diameter of the vein graft models are attached to various internal diameter of the artery models and the vein graft length of 10 cm for the vein graft models are kept constant. In the over length kink vein graft models, the vein graft diameter of 1 mm is kept constant. However, the vein graft lengths are based on the amplitude of two cycled sinusoidal wavy vein graft.

All irregular vein graft models are created to investigate any significant differences in term of velocity of the blood flow, the pressure gradient between proximal and distal, the impact of the wall shear stress and the strain rate in the vein graft models. In the current simulations, there are three different inlet velocities from 6.25 cm/s up to 18.75 cm/s, which have been used as the parameters to simulate blood flow in the vein graft models by using both steady and pulsatile laminar models.

After examining and ensuring that the grid independence is achieved and the equations have been converged, the final results are examined in the post-processing tool Ansys FLUENT Inc. and Microsoft Excel. An observation of the simulation results is shown and discussed in this chapter.

The fact that the blood flow is unsteady is well known. However, it is helpful to first describe the principles of fluid flow under more simplified conditions before moving to complex physiologic situations. Because of this reason, we decided to simulate irregular formation of the vein graft models on the laminar steady state first and then proceed with the laminar pulsatile state.

## **5.2 Irregular Formation Geometry of Vein Graft Model**

The computational domain of the irregular formation geometry of the vein graft models with designing in the GAMBIT. The internal diameter mismatched vein graft models are designed with 10 cm in length, 0.10 cm in internal diameter of the vein graft models and 0.11 cm (Case 1), 0.12 cm (Case 2) and 0.13 cm (Case 3) in internal diameter of the artery models. Those designs of internal diameter mismatched vein graft models can be seen in Figure 5.1 for Case 1, Figure 5.2 for Case 2 and Figure 5.3 for Case 3, respectively. The figures show the vein graft models' inlet, outlet and wall boundaries. The internal diameter mismatched design of the vein graft models consist of the same diameter of the vein graft which are attached to three different internal diameters of the artery models. The internal diameter mismatched of the vein graft models were extruded from the inlet after considering the entrance length for all

calculated Reynolds numbers. For Case 1, 0.10 cm internal diameter of the vein graft models is attached with 0.11 cm internal diameter of the artery models. The subsequent cases, 0.10 cm internal diameter of the vein graft models are attached to 0.12 cm internal diameter of the artery model for Case 2 and 0.13 cm internal diameter of the artery model for Case 3.

In order to carry out the simulation works, the internal diameter mismatched models have to be meshed whereby the domain will be divided into small grids to create nodes where the governing equations are solved. Therefore, the repetition in meshing is done on the internal mismatched diameter vein graft models to create large number of nodes and achieve the grid independence without affecting the vein graft models. The numbers of nodes and hexahedron elements employed to achieve the grid independence for internal diameter mismatched vein graft models are shown in Table 5.1. The maximum total numbers of nodes is 248 751 for all cases, respectively, which attained at meshing works.

Table 5.1: Summary of Meshing for Internal Diameter Mismatched Vein Graft Models

Simulation by Cases	Internal Diameter Mismatched Vein Graft Models	
	Total number of nodes	Total number of hexahedron elements
Ideal Straight Case	248 751	242 000
Case 1	248 751	242 000
Case 2	248 751	242 000
Case 3	248 751	242 000

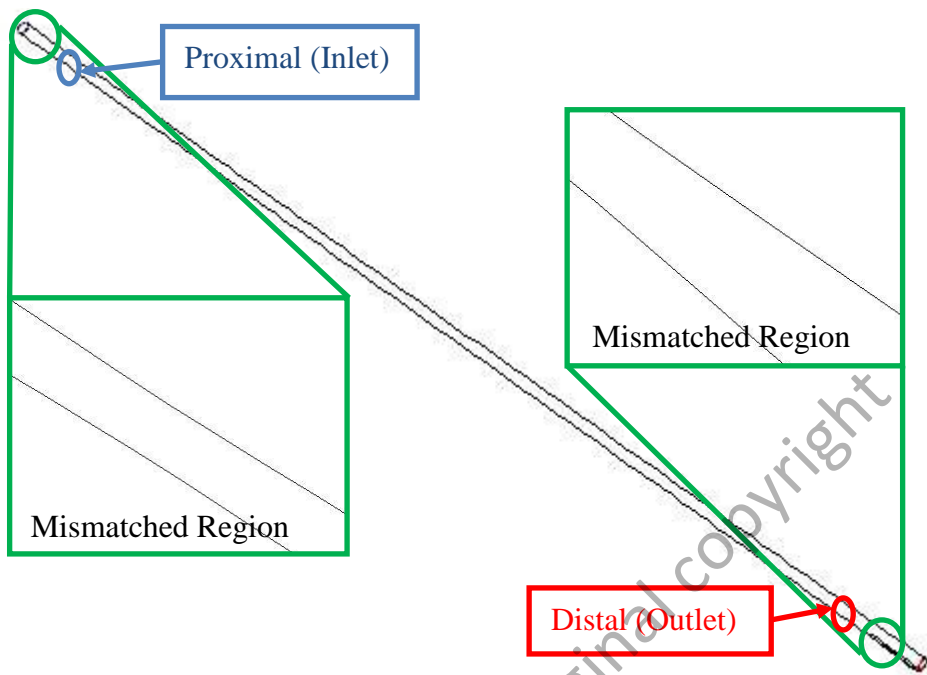


Figure 5.1: Internal Diameter Mismatched Vein Graft Model for Case 1

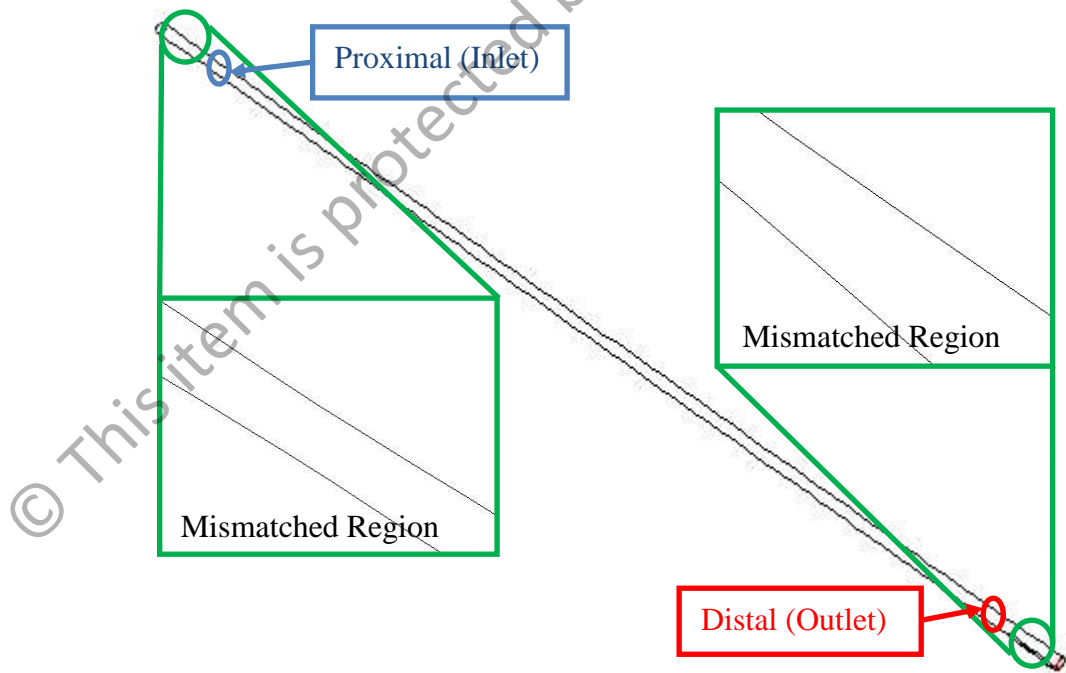


Figure 5.2: Internal Diameter Mismatched Vein Graft Model for Case 2

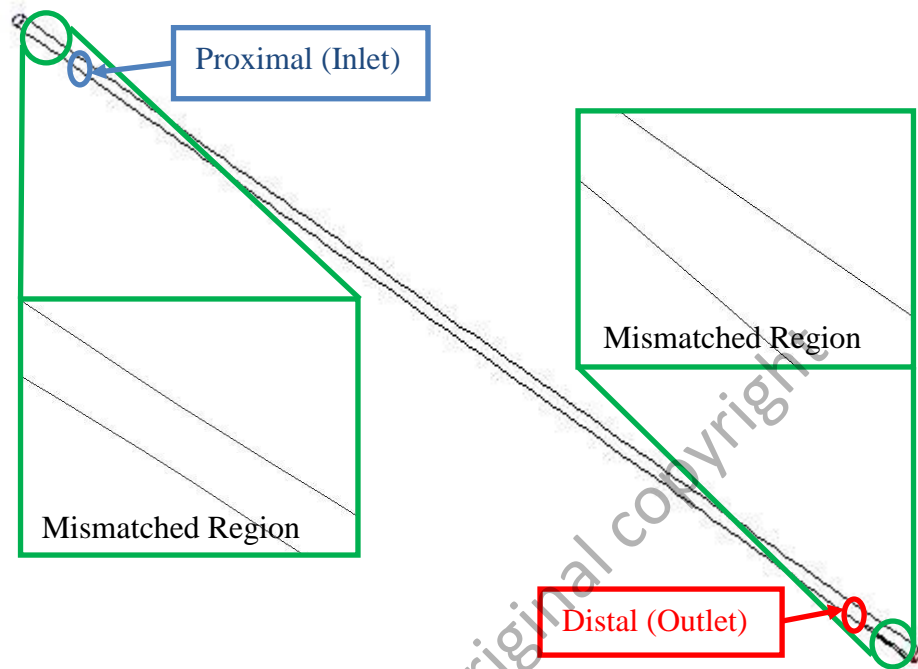


Figure 5.3: Internal Diameter Mismatched Vein Graft Model for Case 3

Three designed Over Length Kinked Vein Graft Models with the kink and curves,  $9^\circ$ ,  $18^\circ$  and  $27^\circ$ , are illustrated in Figure 5.4, Figure 5.5 and Figure 5.6 with the centerline of the vein graft model lengths are 10.01 cm, 10.04 cm, and 10.10 cm, respectively. Those vein graft models are also designed at the same distances in wall to wall diameter. The figures also represent the vein graft models inlet as proximal, outlet as distal and kinked regions. As proposed previously, the vein graft models of 1 millimeter was kept constant for these vein graft models too, as to maintain the consistency of the study within this particular channel, the vein graft models diameter and the vein graft models were also extruded from the inlet after considering the entrance lengths for all calculated Reynolds numbers. Even though the simulation works have been done for the same vein graft models diameter, but the amplitude in the



vein graft models play as an important function for the investigations since the shape of the geometry does affect the fluid flow in the vein graft models. In order to achieve the grid independence, simulation by cases has been performed. The number of nodes and hexahedral elements that are employed to achieve the grid independence state is shown in Table 5.1. The total number of nodes and hexahedral elements generated by cases simulation are 222 761 nodes and 216 000 hexahedral elements for Case A and 443 681 nodes and 432 000 hexahedral elements for Case B and 443 681 nodes and 432 000 hexahedral elements for Case C, respectively. Table 5.2 also shows the number of nodes and hexahedral elements that are employed to achieve the grid independence state in the Over Length Kink Vein Graft Models.

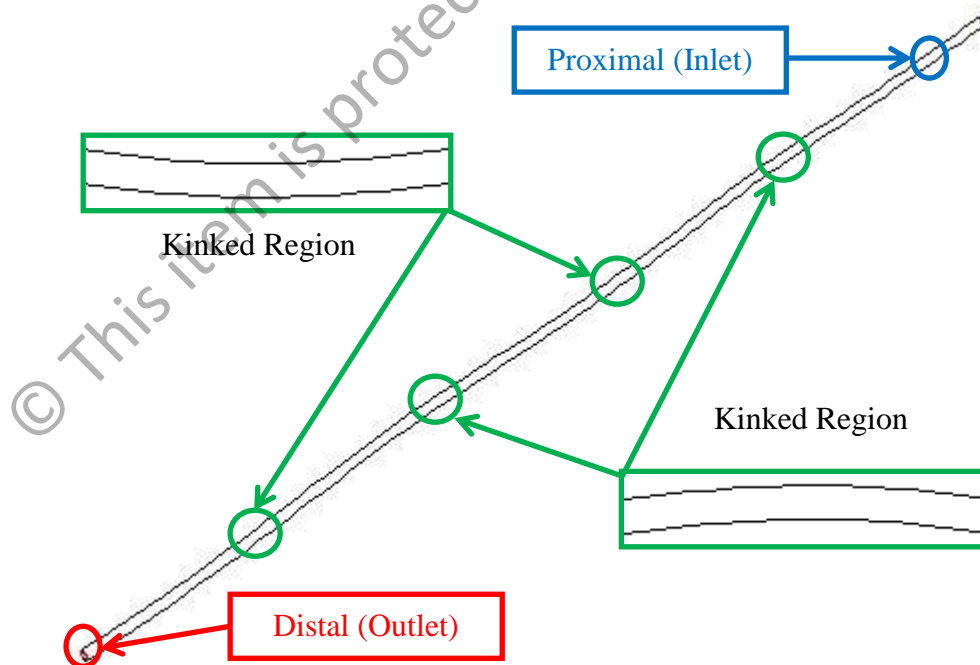


Figure 5.4: Over Length Kinked Vein Graft Models for Case A

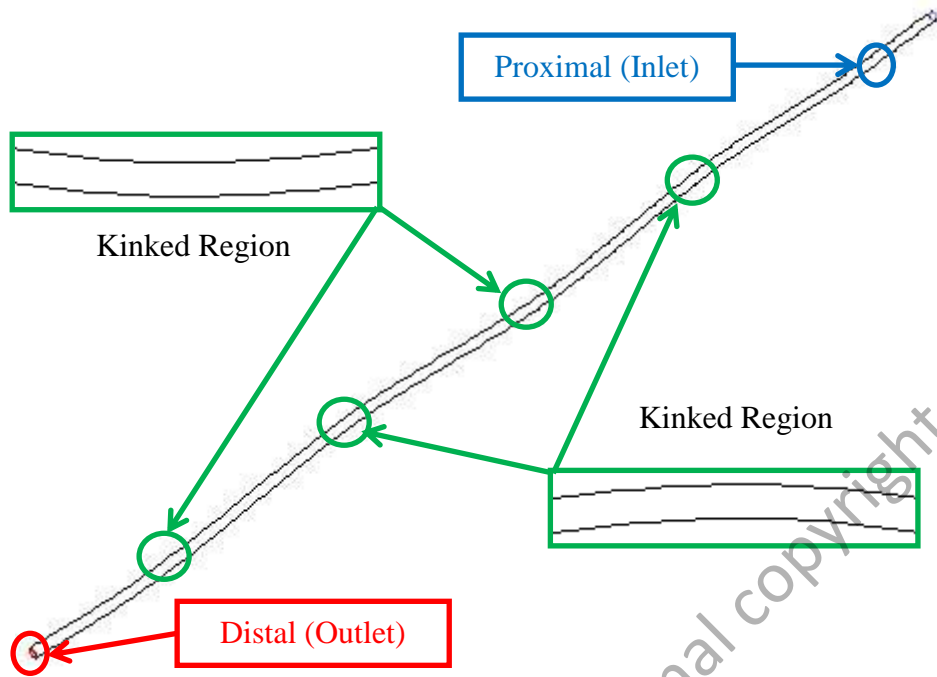


Figure 5.5: Over Length Kinked Vein Graft Models for Case B

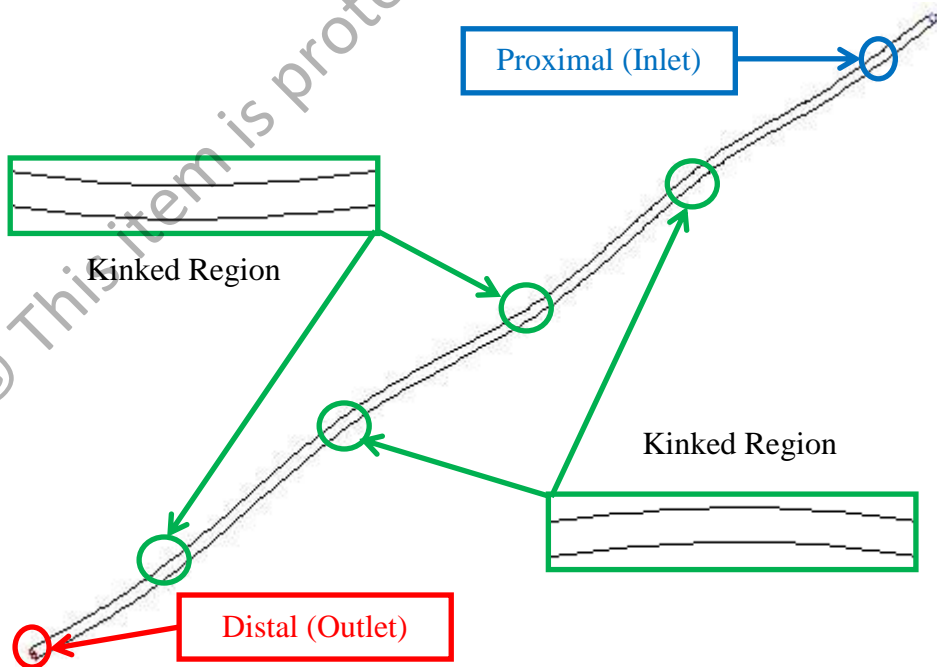


Figure 5.6: Over Length Kinked Vein Graft Models for Case C

Table 5.2: Summary of meshing for Over Length Kinked Vein Graft Models

Simulation by Cases	Over Length Kinked Vein Graft Models	
	Total number of nodes	Total number of hexahedron elements
Ideal Straight Case	248 751	242 000
Case A	222 761	216 000
Case B	443 681	432 000
Case C	443 681	432 000

### 5.3 Grid Independence Test

The grid independence test is carried out for these Internal Diameter Mismatched Vein Graft Models by observing the velocity profiles blood flow. The velocity profile is observed at the proximal (inlet), middle and distal (outlet) of the vein graft models. These are Case 1, Case 2 and Case 3 simulations which have been carried out for the test of grid independence and accuracy. Figure 5.7, Figure 5.8 and Figure 5.9 show the independence checking for Case 1, Case 2 and Case 3, respectively.

The error percentage of the velocity profile of the Internal Diameter Mismatched Vein Graft Model for Case 1 at the middle and distal is 1.605 % and 0.831 % higher compared to the proximal, respectively. In terms of the Internal Diameter Mismatched Vein Graft Model for Case 2, the error percentage of the velocity profile at the middle and distal is 2.646 % and 0.8127 % compared to the proximal, respectively. The error percentage of the velocity profile for Case 3 at the proximal and middle is 1.984% and 1.975 % higher compared to the distal, respectively. Additionally, the velocity profiles also do not show any significant variations hence the simulation has achieved the grid independence. Besides, the convergence history has been monitored for both mass and momentum until the residual target reaches below  $1 \times 10^{-6}$ .

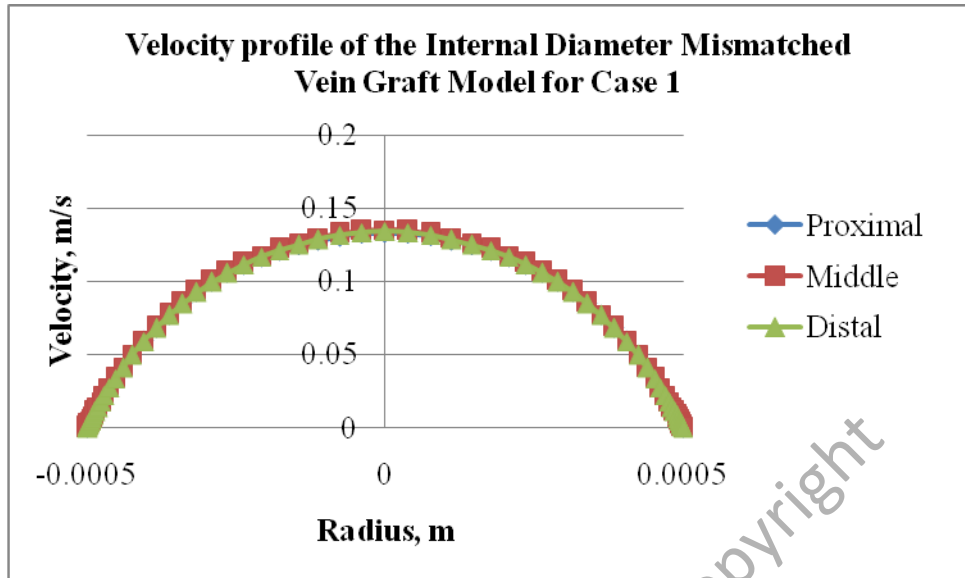


Figure 5.7: The grid independence test of the Internal Diameter Mismatched Vein Graft Model for Case 1 with comparison of velocity profiles for three different positions in the vein graft model.

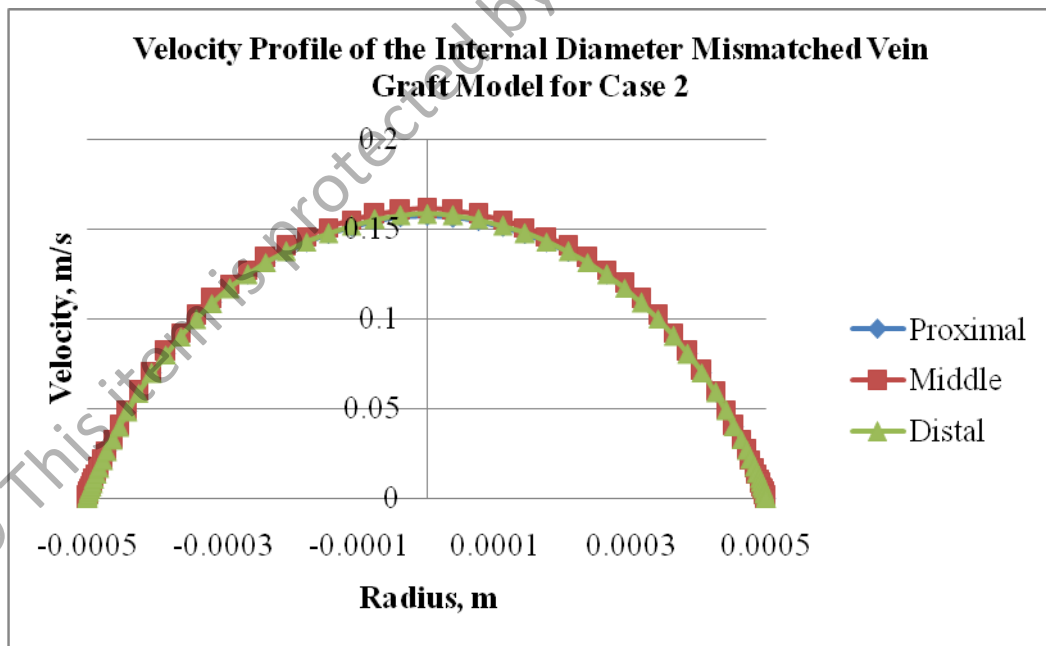


Figure 5.8: The grid independence test of the Internal Diameter Mismatched Vein Graft Model for Case 2 with comparison of velocity profiles for three different positions in the vein graft model.

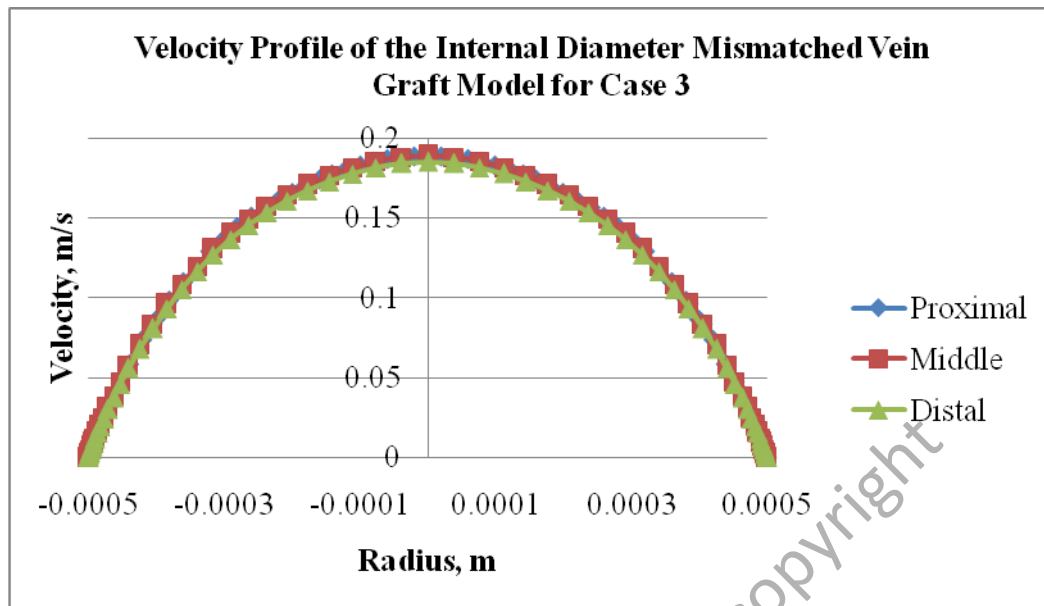


Figure 5.9: The grid independence test of the Internal Diameter Mismatched Vein Graft Model for Case 3 with comparison of velocity profiles for three different positions in the vein graft model.

As stated in the previous chapter, the same settings of grid that were used for ideal straight and internal diameter mismatched vein graft models is also applied for the Over Length Kinked Vein Graft Model. An observation on the velocity profile of the blood flow test is also conducted for the grid independence test in these cases. The velocity profile is observed at the proximal (inlet) and distal (outlet) of the vein graft models, where the fully developed flow is considered. Figure 5.10, 5.11 and 5.12 show the grid independence test for the Over Length Kinked Vein Graft Models, respectively. Based on the observation, the error percentage of the velocity profile of the Over Length Kinked Vein Graft Model for Case A, Case B and Case C at the proximal is 0.29%, 0.11 % and 0.07 % lower compared to the distal, respectively. However, the velocity profiles do not show any significant changes since the micro channels are in the grid independence state.

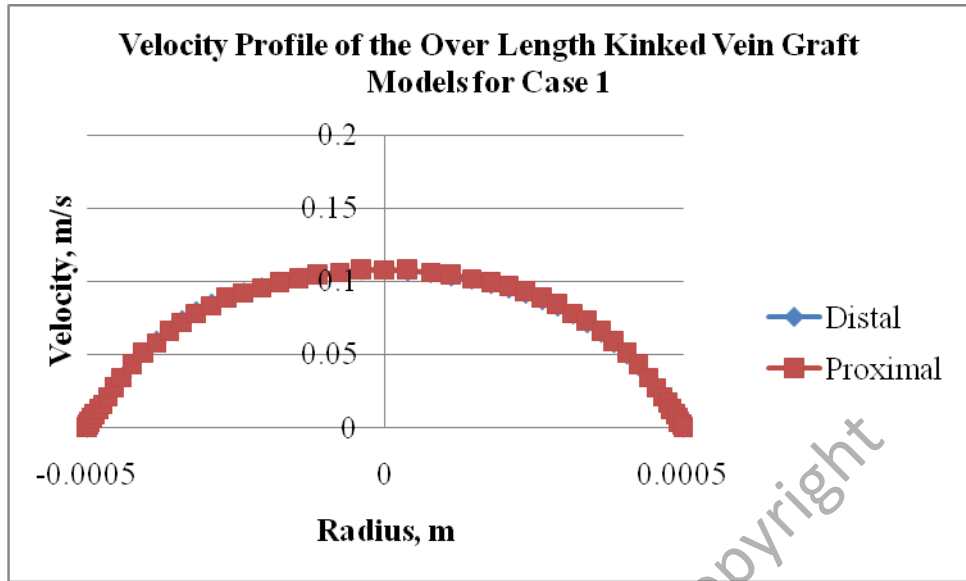


Figure 5.10: The grid independence test of the Over Length Kinked Vein Graft Models for Case A with comparison of velocity profiles for two different positions in the vein graft model.

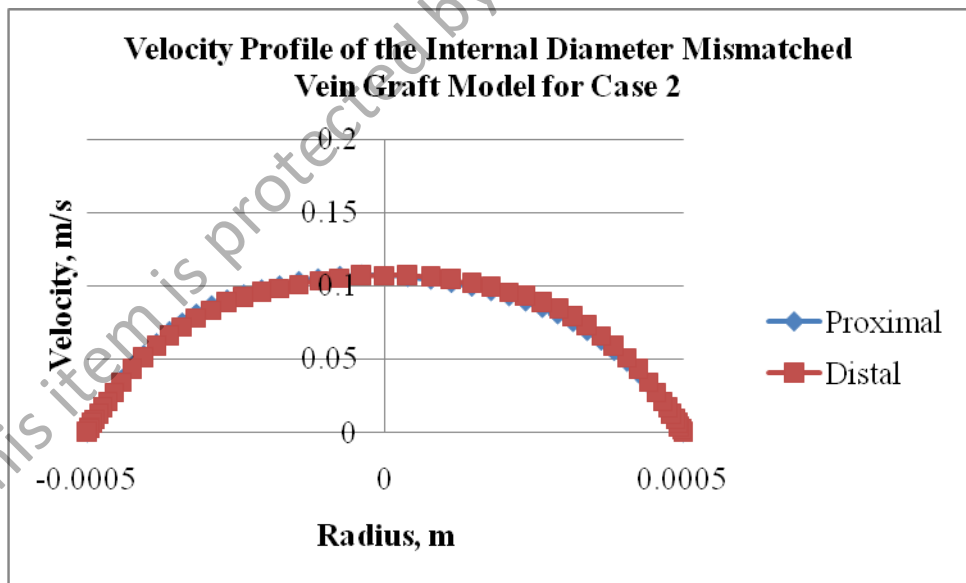


Figure 5.11: The grid independence test of the Over Length Kinked Vein Graft Models for Case B with comparison of velocity profiles for two different positions in the vein graft model.

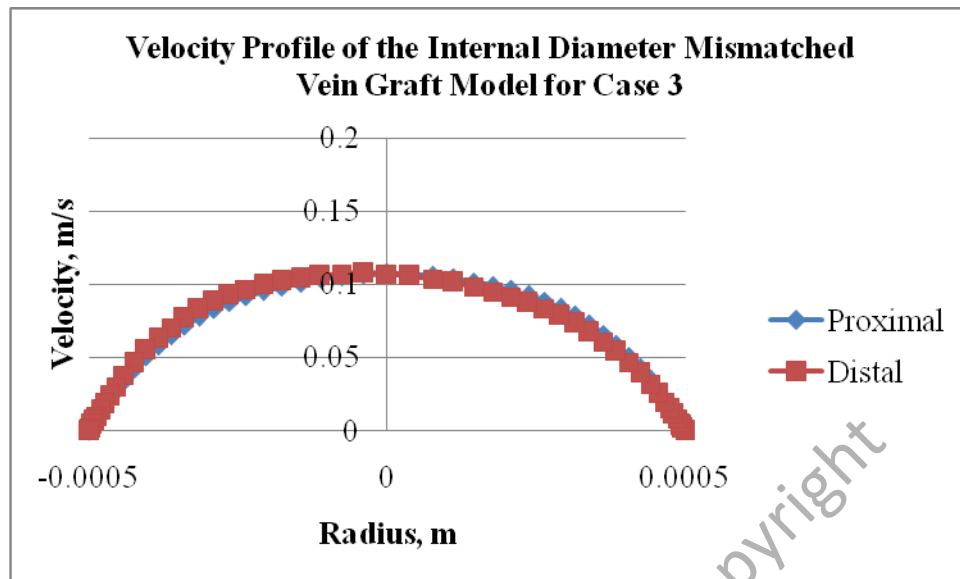


Figure 5.12: The grid independence test of the Over Length Kinked Vein Graft Models for Case C with comparison of velocity profiles for two different positions in the vein graft model.

Therefore, analysis and results that have been discussed in the following subsections are based on simulation of the internal diameter mismatched and the Over Length Kinked Vein Graft Models.

#### 5.4 Simulation Results of the Irregular Vein Graft Models

In this section, several important preliminary field variables in the blood flow phenomenon of the vein graft models are the central focus. As mentioned earlier, several investigations are carried out for a series of cases of the irregular vein graft models by using the laminar steady state and the laminar pulsatile blood flow models. The laminar steady state blood flow model is considered for validation. Meanwhile, the laminar pulsatile blood flow model is considered for the pulsatile model to study the

pulsatile blood flow on an actual vein graft model as to closely simulate the in-vivo condition of the vein graft. Besides, the utilization of this laminar pulsatile blood flow model is to check its capability to predict blood flow in the vein graft models as well as any correlation differences with the laminar steady state model. The modeling for blood flow is based on continuity and momentum equations. Hence, the field variables considered here are velocity in terms of the profile, pressure gradient and wall shear stress which have been observed for the irregular vein graft models. Other findings related to the flow mechanism such as fully developing region or entrance length are also described. The utilization of the laminar steady state and laminar pulsatile blood flow models allow the observation of any trend of the blood flow.

#### **5.4.1 Results of Velocity Observation in Laminar Steady State Flow**

Table 5.3 shows the summary of dimension for Internal Diameter Mismatched Vein Graft Models. For a model of the Ideal Straight Case, 0.10 cm internal diameter of the vein graft is attached to 0.10 cm internal diameter of the artery. For Case 1, 0.10 cm internal diameter of the vein graft is attached to 0.11 cm internal diameter of the artery. For Case 2 and Case 3, 0.10 cm internal diameter of vein graft is attached to 0.12 cm and 0.13 cm internal diameter of the arteries, respectively. Ratios of attachment with internal diameter differences are also shown in Table 5.3. The inlet velocity of 12.5 cm/s is applied at the proximal of the vein graft model in all cases for this experiment.





Figure 5.13 shows the schematic figure of Internal Diameter Mismatched Vein Graft Model that represents the model of Ideal Straight, Case 1, Case 2 and Case 3. Where  $R_{ia}$  is the artery internal radius,  $O_{ia}$  is the centre of the artery,  $-R_{ia}$  is the artery internal radius,  $R_{iv}$  is the vein internal radius,  $O_{iv}$  is the centre of the vein,  $-R_{iv}$  is the vein internal radius,  $L_v$  is the vein length constant. As stated in Chapter 4, the Surface Monitors need to be set in the Fluent Pre-Processing to allow the flow variables such as velocity, pressure, wall shear stress and strain rate can be collected and analyzed. The applied Surface Monitors for velocity observation in these models are Lines. These lines are placed at the Proximal and Distal of the vein graft models.

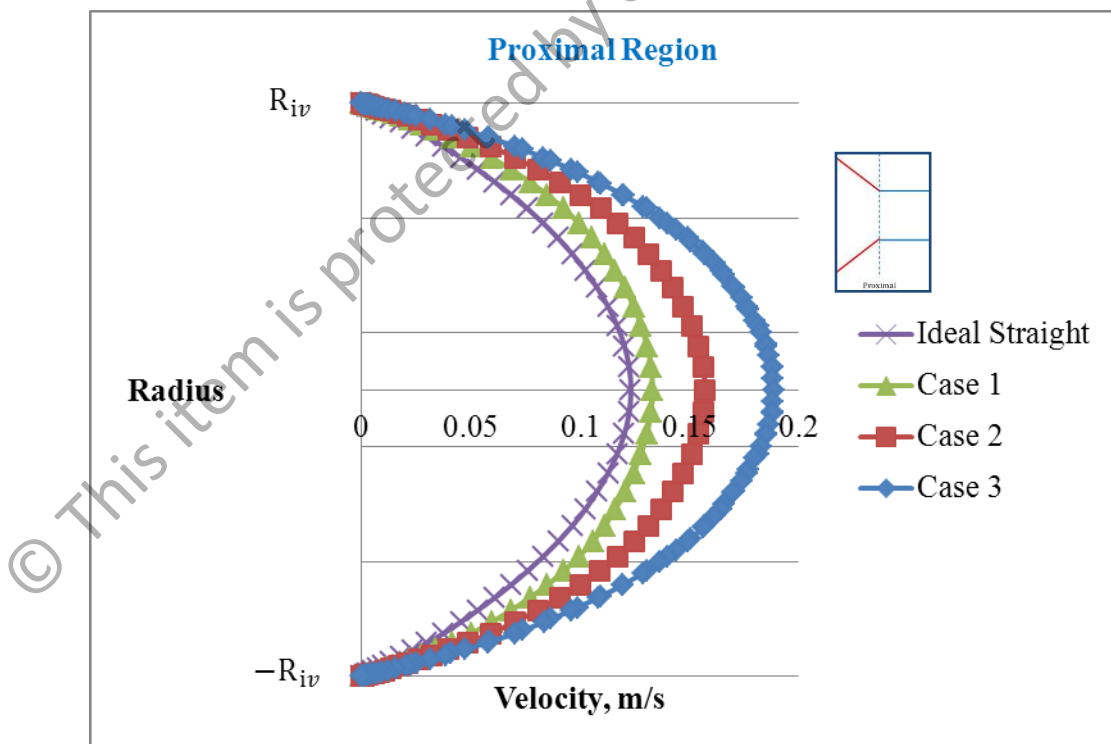


Figure 5.14: The velocity profile of blood flow at the Proximal Region in Ideal Straight, Case 1, Case 2 and Case 3.

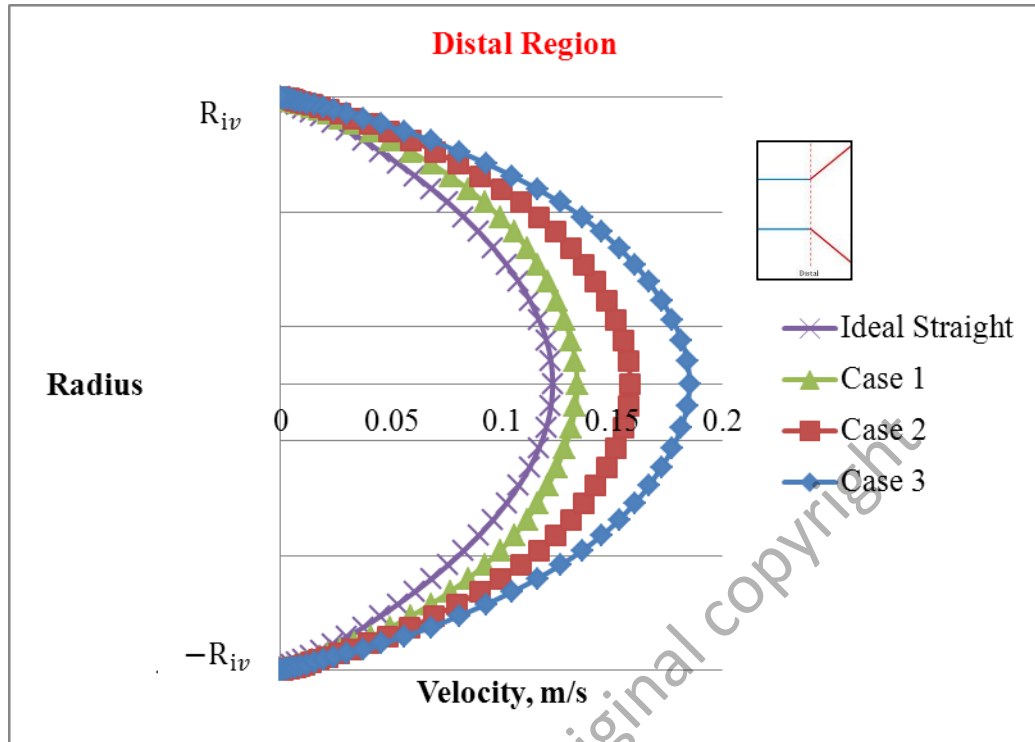


Figure 5.15: The velocity profile of blood flow at the Distal Region in Ideal Straight, Case 1, Case 2 and Case 3.

Table 5.4 : A summary of the centre velocity of blood at the Proximal and Distal Region for Ideal Straight, Case 1, Case 2 and Case 3.

	Centre Velocity, $v_o$ (m/s)	
	Proximal	Distal
Ideal Straight	0.1232	0.1231
Case 1	0.1331	0.1342
Case 2	0.1570	0.1583
Case 3	0.1888	0.1852

Figure 5.14 and Figure 5.15 show the velocity profile of blood flow at the Proximal and Distal Region in the vein graft model of Ideal Straight, Case 1, Case 2 and Case 3. Based on Table 5.4, the highest velocity of blood flow occurs in Case 3 vein graft model and gradually decreases in Case 2, Case 1 and Ideal Straight Case. The increase of the centre velocity is due to the increase of mismatched percentage.

Table 5.5 shows the summary of dimension for the Over Length Kinked Vein Graft Models. For the model of the Ideal Straight Case, Case A, Case B and Case C are constructed with the same diameter, 0.1cm but are different in lengths. For the Ideal Straight Case model, 10 cm length of the vein graft is attached to the artery. For Case A, 10.01 cm length of the vein graft is attached to the artery. For Case B and Case C, 10.02 cm and 10.03 cm length of the vein graft is attached to the artery, respectively. The amplitude of two cycled sinusoidal wavy veins with length differences are also shown in Table 5.5. The inlet velocity is 12.5 cm/s as the velocity is applied at the proximal of the vein graft model in all cases for this experiment.

Table 5.5: Summary of Dimension for the Over Length Kinked Vein Graft Models

	$D_{\text{artery}} = D_{\text{vein}}$ , cm	Vein Length, cm	Amplitude of two cycled sinusoidal wavy veins, cm
Ideal Straight	0.10	10	0
Case A	0.10	10.01	0.05
Case B	0.10	10.04	0.10
Case C	0.10	10.10	0.15

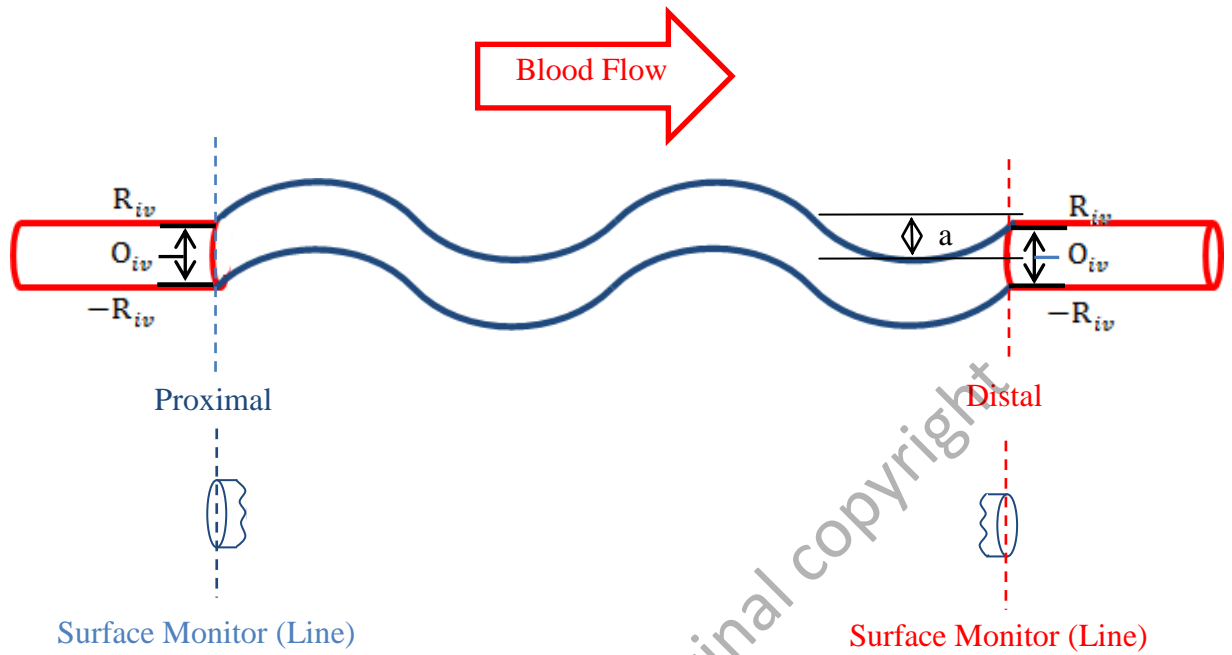


Figure 5.16: Schematic figure of the Over Length Kinked Vein Graft Models and the Surface Monitor. The applied types of Surface Monitors at the Proximal and Distal are Lines.

Figure 5.16 shows the schematic figure of the Over Length Kinked Vein Graft Model that represents the models of Ideal Straight, Case A, Case B and Case C. Where  $R_{iv}$  is the vein internal radius,  $O_{iv}$  is the centre of the vein,  $-R_{iv}$  is the vein internal radius and  $a$  is the amplitude. As also stated in Chapter 4, the Surface Monitors need to be set in the Fluent Pre-Processing to allow the flow variables such as velocity, pressure, wall shear stress and strain rate can be collected and analyzed. The applied Surface Monitors for velocity observation in these models are Lines. These lines are placed at the Proximal and Distal of the vein graft models.

Figure 5.17 and Figure 5.18 show the velocity profile of blood flow at the Proximal and Distal Region in the vein graft model of Ideal Straight, Case A, Case B and Case C. Based on Table 5.6, the Ideal Straight Case demonstrates the highest velocity in blood flow. On the contrary, Case A, Case B and Case C demonstrate low velocity. It happens due to curvature geometry.

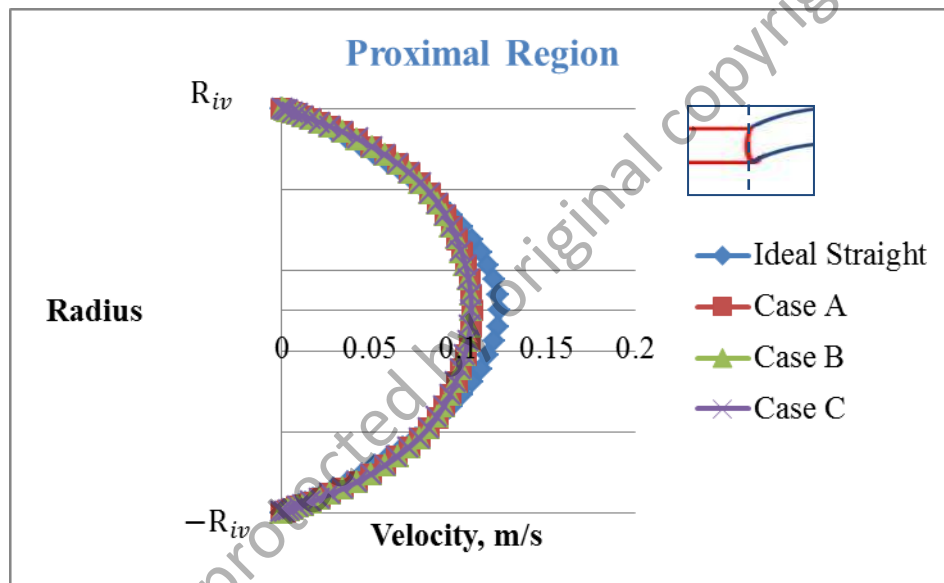


Figure 5.17: The velocity profile of blood flow at the Proximal Region in Ideal Straight, Case A, Case B and Case C.

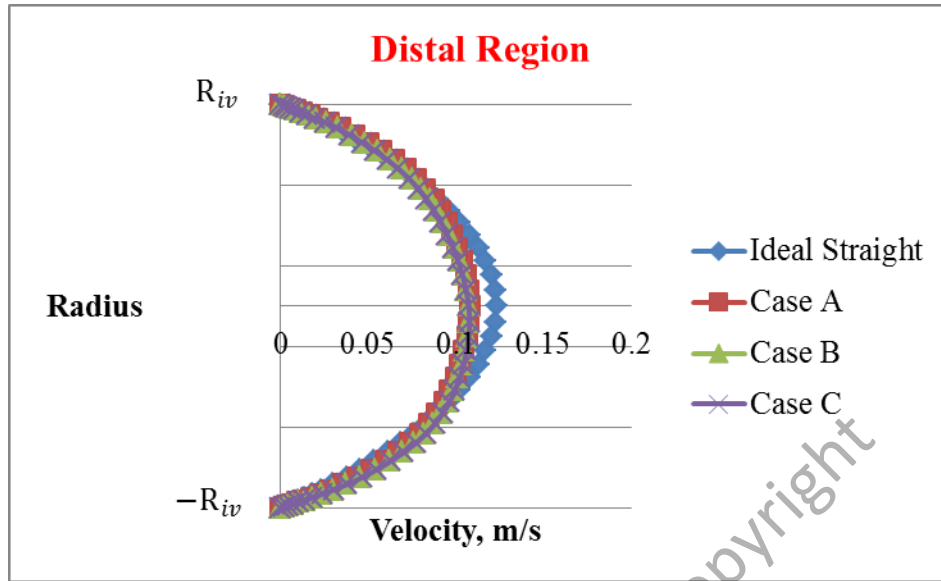


Figure 5.18: The velocity profile of blood flow at the Distal Region in Ideal Straight, Case A, Case B and Case C.

Table 5.6: The summary of the centre velocity of blood flow at the Proximal and Distal Region for Ideal Straight, Case A, Case B and Case C

	Centre Velocity, $v_o$ (m/s)	
	Proximal	Distal
Ideal Straight	0.1232	0.1231
Case A	0.1073	0.1074
Case B	0.1074	0.1074
Case C	0.1073	0.1073

#### 5.4.2 Results of Velocity Observation in the Laminar Pulsatile Flow

The experiment on the Irregular Vein Graft Models has been continued on the Laminar Pulsatile Flow. For this experiment, the same models in the steady flow experiment are used but with UDF flow and other types of surface monitor are applied

(Figure 5.19 and 5.26). In order to carry out this experiment, the UDF containing 6.25 cm/s for minimum velocity and 18.75 cm/s for maximum velocity is applied at the proximal in all cases as mentioned in previous sub-chapter 4.3.3.

All dimensions can be referred to Table 5.3. Figure 5.19 shows the schematic figure of the Internal Diameter Mismatched Vein Graft Model that represents the model of Ideal Straight, Case 1, Case 2 and Case 3. Where  $R_{ia}$  is the artery internal radius,  $O_{ia}$  is the centre of the artery,  $-R_{ia}$  is the artery internal radius,  $R_{iv}$  is the vein internal radius,  $O_{iv}$  is the centre of the vein,  $-R_{iv}$  is the vein internal radius,  $L_v$  is the vein length is constant. The Point is chosen as the Surface Monitors for the pulsatile velocity observation in these models because it is more suitable in monitoring the pulsatile velocity observation compare to Line. These points are placed at the Proximal and Distal of the vein graft models.

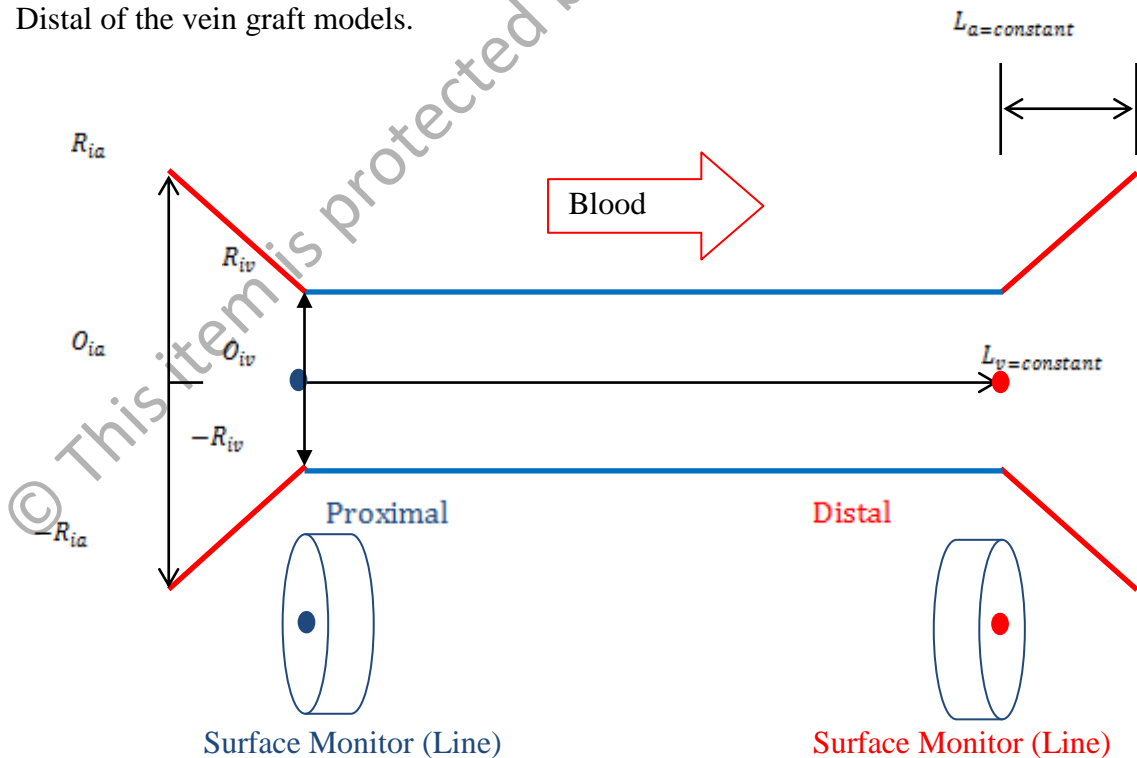


Figure 5.19: The schematic figure of the Internal Diameter Mismatched Vein Graft Model and the Surface Monitor. The applied types of the Surface Monitors at the Proximal and Distal are Point.



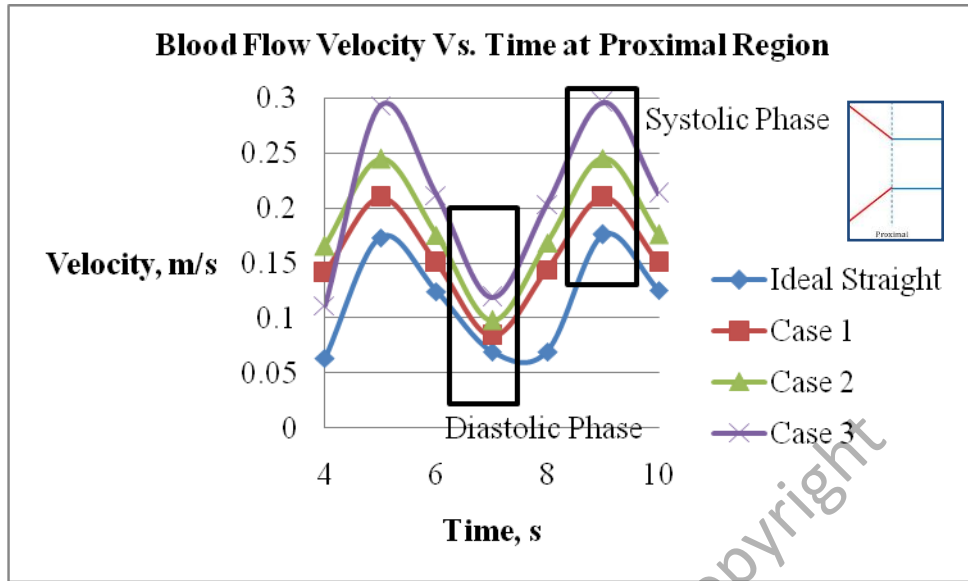


Figure 5.20: The pulsatile velocity at the Proximal Region in Ideal Straight, Case 1, Case 2 and Case 3.

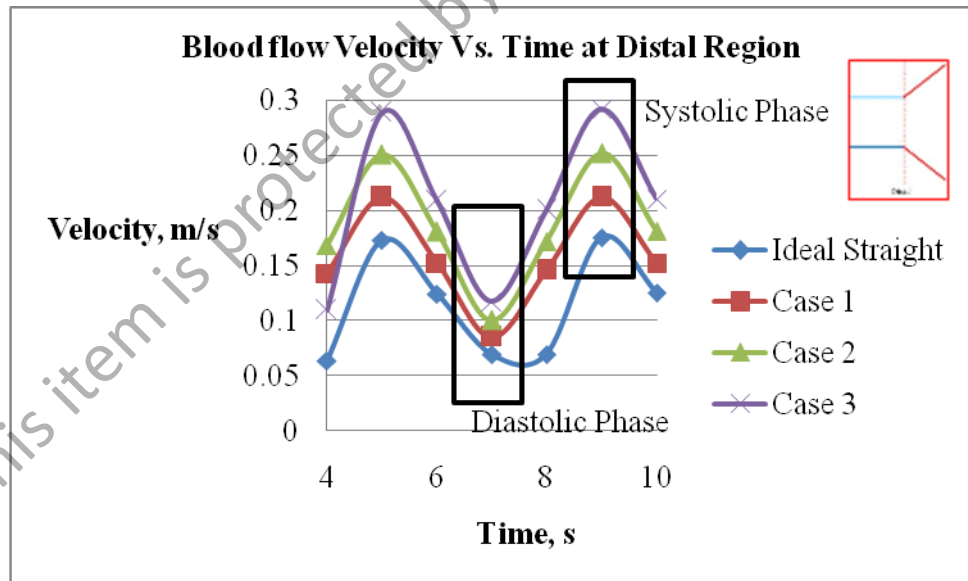


Figure 5.21: The pulsatile velocity at the Distal Region in Ideal Straight, Case 1, Case 2 and Case 3.

Table 5.7 : The Summary of the center of pulsatile velocity of blood flow at the Proximal and Distal Region for Ideal Straight, Case 1, Case 2 and Case 3.

	Centre Velocity, $v_o$ (m/s)			
	Proximal		Distal	
	Systolic Phase	Diastolic Phase	Systolic Phase	Diastolic Phase
Ideal Straight	0.1756	0.0633	0.1754	0.0636
Case 1	0.2097	0.1412	0.2113	0.1425
Case 2	0.2454	0.1657	0.2519	0.1683
Case 3	0.2961	0.1111	0.2919	0.1092

Figure 5.20 and 5.21 shows the center of the pulsatile velocity of blood flow at the Proximal and Distal Region in the vein graft model of Ideal Straight, Case 1, Case 2 and Case 3. The highest velocity of blood flow occurs in Case 3 of the vein graft model and the values of blood flow gradually decrease in Case 2, Case 1 and Ideal Straight Case at systolic phase as shown in Table 5.7. At diastolic phase, the vein graft model in Case 3 also demonstrates the highest velocity of blood flow and the values of blood flow gradually decrease in Case 2, Case 1 and Ideal Straight Case. The increase in velocity especially in Case 3 happens due to a decrease of the flow area in the vein. The tolerance velocity from clinical data is +/- 0.006 m/s for systolic phase and +/- 0.00375 m/s for diastolic phase. Based on table 5.7, a mismatched over than 10% should be avoided because of acceptable tolerance velocity.

This experiment work has been conducted further in details by capturing the velocity profile in blood flow at the proximal and distal region in all cases. In order to capture the velocity profile, the line has been chosen again as the type of monitoring surface as shown in Figure 5.13. The results of this experiment are shown in Figure 5.22, 5.23, 5.24 and 5.25. The summary of these results are shown in Table 5.8.

Figure 5.22, 5.23, 5.24 and 5.25 show the velocity profile of blood flow at the Proximal and Distal Region of the vein graft model in Ideal Straight Case, Case 1, Case

2 and Case 3. Based on Table 5.8, the highest velocity of blood flow occurs in Case 3 of the vein graft model and gradually decreases in Case 2, Case 1 and Ideal Straight Case.

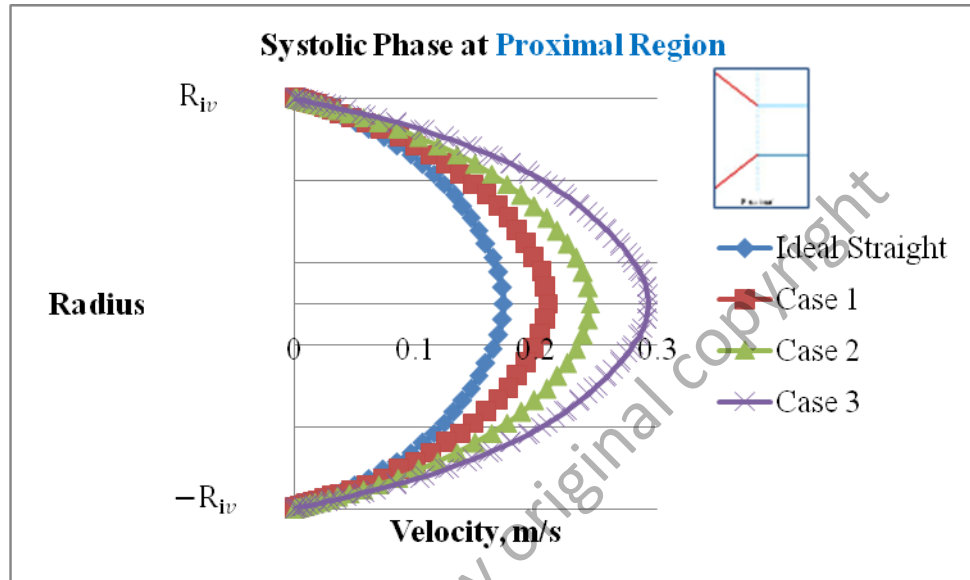


Figure 5.22: The velocity profile of blood flow at the proximal region in Ideal Straight, Case 1, Case 2 and Case 3 during systolic phase.

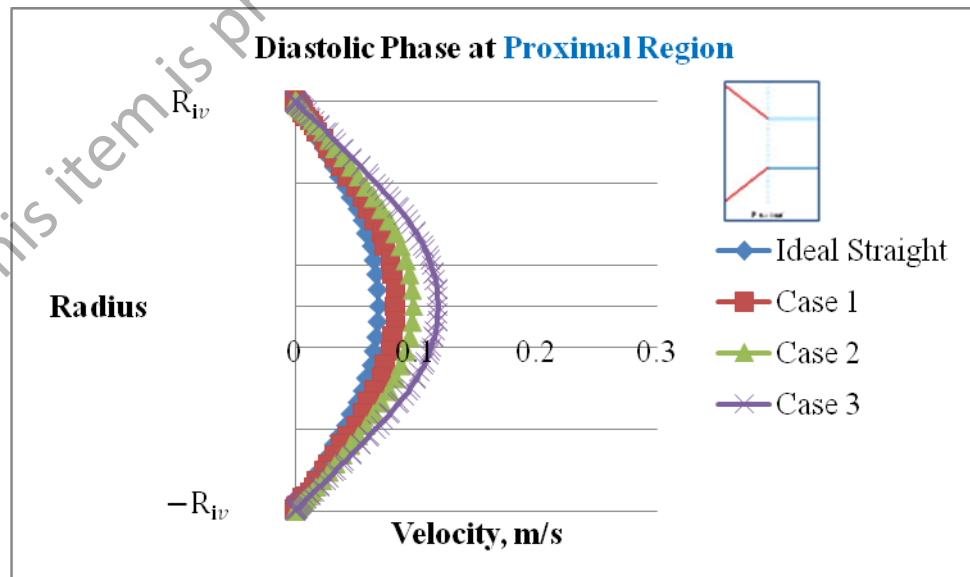


Figure 5.23: The velocity profile of blood flow at the proximal region in Ideal Straight, Case 1, Case 2 and Case 3 during diastolic phase.

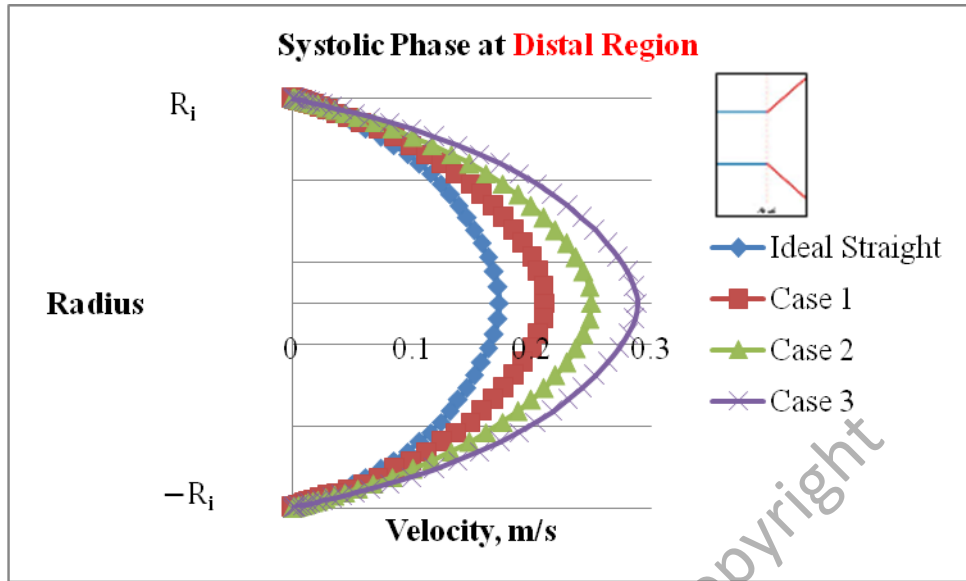


Figure 5.24: The profile of blood flow at the distal region in Ideal Straight, Case 1, Case 2 and Case 3 during systolic phase.

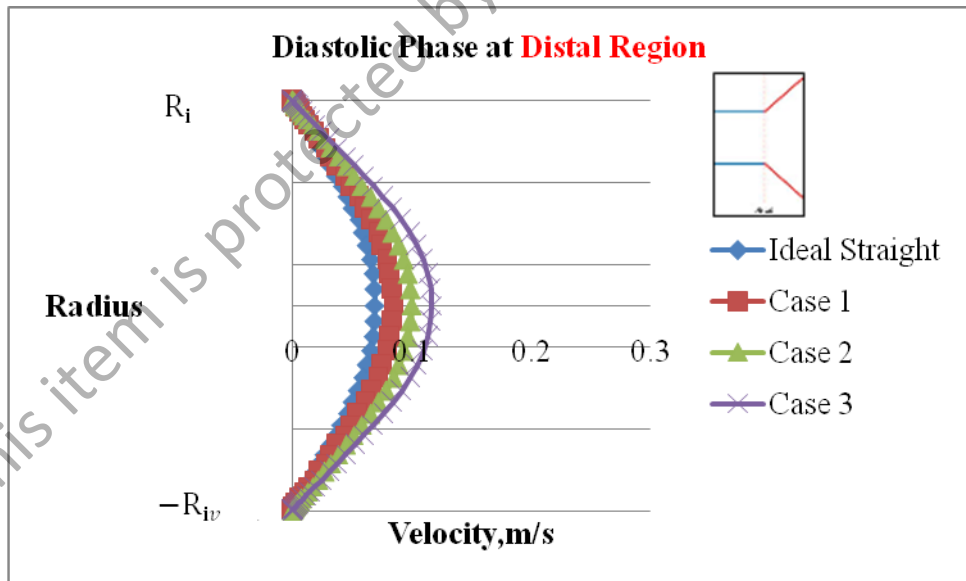


Figure 5.25: The velocity profile of blood flow at the distal region in Ideal Straight, Case 1, Case 2 and Case 3 during diastolic phase.

Table 5.8: Summary of the center of pulsatile velocity of blood at the Proximal and Distal Region in Ideal Straight, Case 1, Case 2 and Case 3 (Captured by velocity profiles).

	Centre Velocity, $v_o$ (m/s)			
	Proximal		Distal	
	Systolic Phase	Diastolic Phase	Systolic Phase	Diastolic Phase
Ideal Straight	0.1732	0.0693	0.1730	0.0694
Case 1	0.2095	0.0836	0.2118	0.0847
Case 2	0.2445	0.0976	0.2504	0.1003
Case 3	0.2930	0.1187	0.2887	0.1172

Figure 5.26 shows the schematic figure of the Over Length Kinked Vein Graft Model that represents the models of Ideal Straight, Case A, Case B and Case C. Where  $R_{iv}$  is the vein internal radius,  $O_{iv}$  is the centre of the vein,  $-R_{iv}$  is the vein internal radius and  $a$  is the amplitude. All dimensions can be referred in Table 5.5. The Point is also chosen as the Surface Monitors for pulsatile velocity observation in these models because it is more suitable in monitoring the pulsatile velocity observation compared to Line. These points are also placed at the Proximal and Distal of the vein graft models.

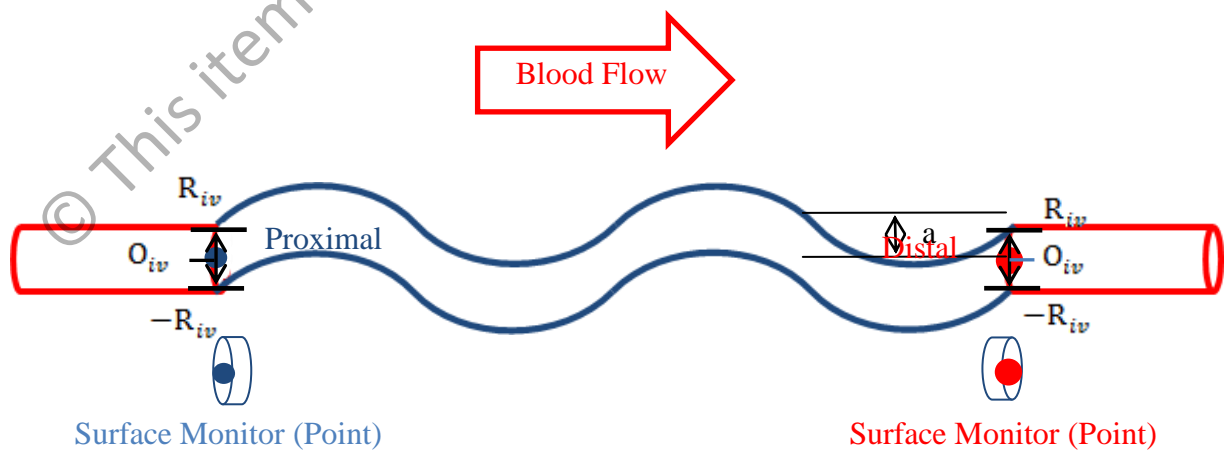


Figure 5.26: The schematic figure of the Over Length Kinked Vein Graft Models and the Surface Monitor. The applied types of Surface Monitors at the Proximal and Distal are Points.

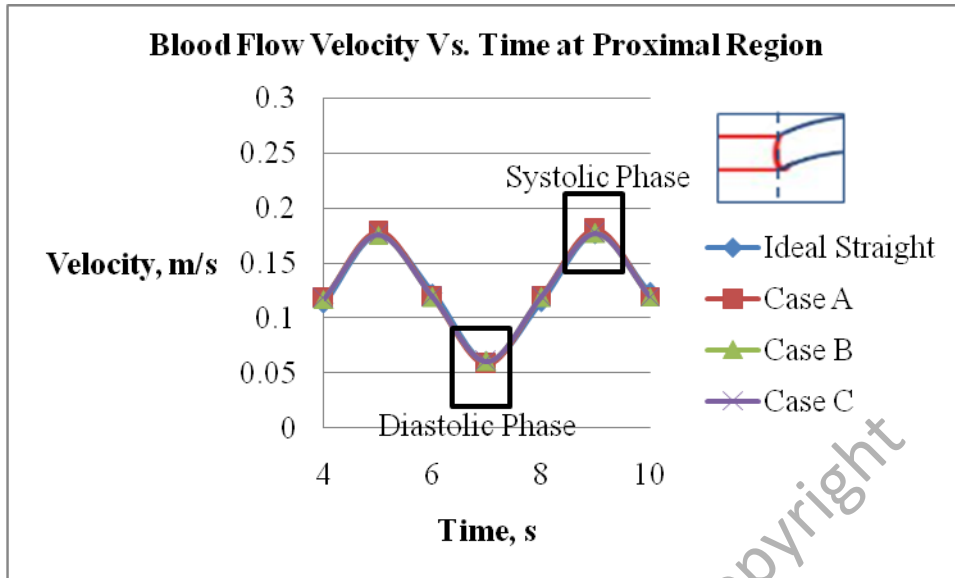


Figure 5.27: Pulsatile velocity at the Proximal Region in Ideal Straight, Case A, Case B and Case C.

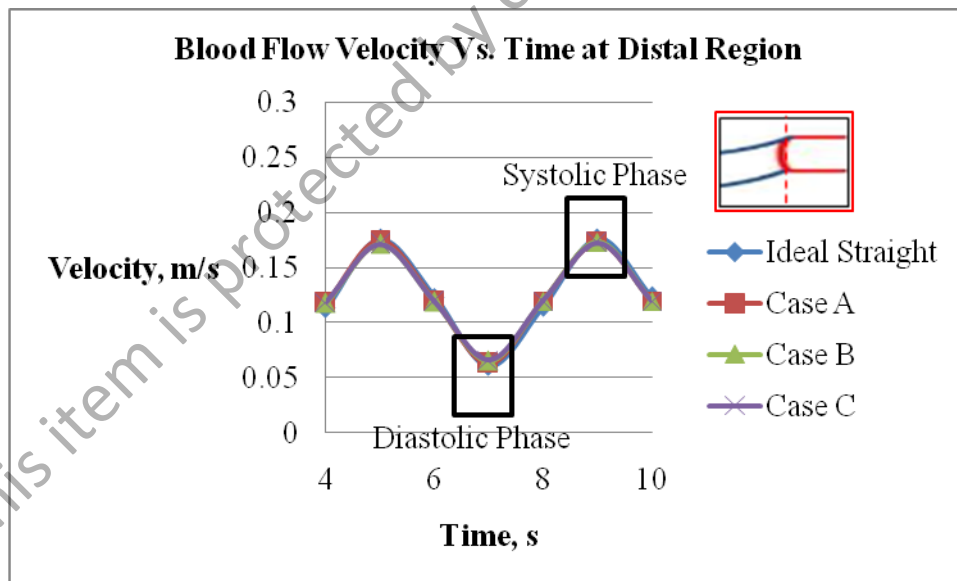


Figure 5.28: Pulsatile velocity at the Distal Region in Ideal Straight, Case A, Case B and Case C.

Table 5.9: Summary of the centre of pulsatile velocity of blood flow at the Proximal and Distal Region in Ideal Straight, Case A, Case B and Case C.

	Centre Velocity, $v_0$ (m/s)			
	Proximal		Distal	
	Systolic Phase	Diastolic Phase	Systolic Phase	Diastolic Phase
Ideal Straight	0.1756	0.0605	0.1756	0.0605
Case A	0.1721	0.0562	0.1721	0.0561
Case B	0.1721	0.0562	0.1721	0.0562
Case C	0.1720	0.0562	0.1720	0.0562

Figure 5.27 and Figure 5.28 show the centre of pulsatile velocity of blood flow at the Proximal and Distal Region of the vein graft model in Ideal Straight, Case A, Case B and Case C. From the observation, all cases demonstrate no obviously different in velocity values at all positions in Table 5.9 and even in all phases. However, based on clinical data, all kinking cases cannot be applied for surgery because the blood that flow through those models are too slow and also out of acceptable ranges. In other words, kinked wavy sinusoidal veins must be below than 0.0005 m height.

This experimental work also has been carried further in details by capturing the velocity profile in blood flow at the proximal and distal region in Ideal Straight, Case A, Case B and Case C as performed in previous internal mismatch cases. In order to capture the velocity profile, the line has also been chosen as the types of monitoring surface as shown in Figure 5.13. The results of this experiment are shown in Figure 5.29, 5.30, 5.31 and 5.32. The summary of these results are shown in Table 5.10.

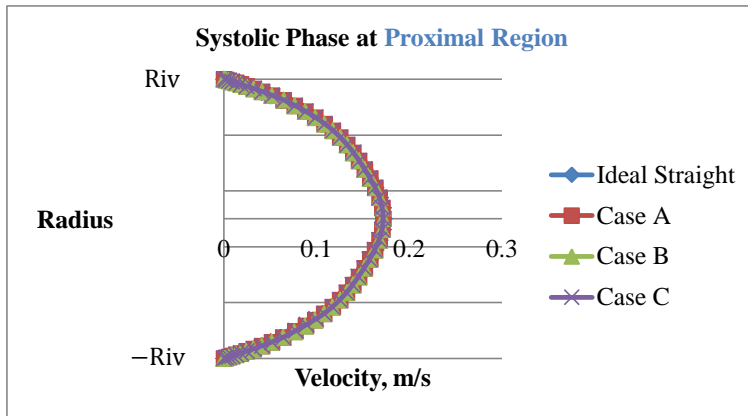


Figure 5.29: The velocity profile of blood flow at the proximal region in Ideal Straight, Case A, Case B and Case C during systolic phase.

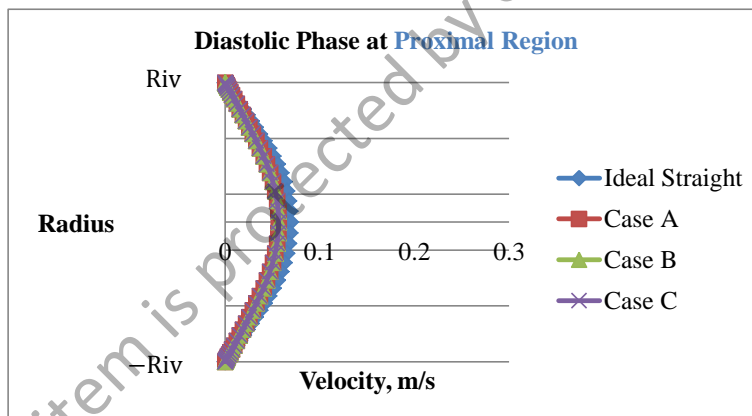


Figure 5.30: The velocity profile of blood flow at the proximal region in Ideal Straight, Case A, Case B and Case C during diastolic phase.



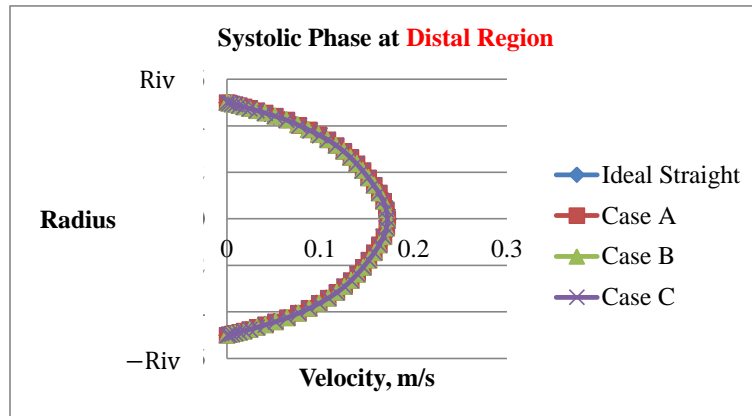


Figure 5.31: The velocity profile of blood flow at the distal region in Ideal Straight, Case A, Case B and Case C during systolic phase.

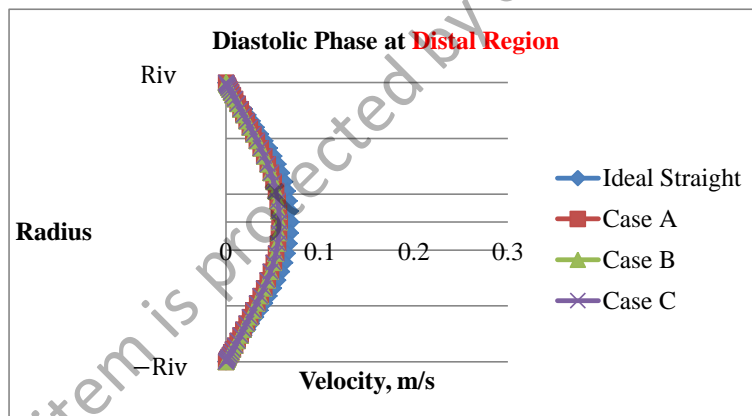


Figure 5.32: The velocity profile of blood flow at the distal region in Ideal Straight, Case A, Case B and Case C during diastolic phase.

Table 5.10: Summary of the centre of pulsatile velocity of blood flow at the Proximal and Distal Region for Ideal Straight, Case A, Case B and Case C (Captured the velocity profile).

	Centre Velocity, $v_o$ (m/s)			
	Proximal		Distal	
	Systolic Phase	Diastolic Phase	Systolic Phase	Diastolic Phase
Ideal Straight	0.1732	0.0693	0.1730	0.0693
Case A	0.1721	0.0561	0.1721	0.0561
Case B	0.1721	0.0562	0.1721	0.0562
Case C	0.1720	0.0562	0.1720	0.0558

Figure 5.29, 5.30, 5.31 and 5.32 show the velocity profile of blood flow at the Proximal and Distal Region of the vein graft model in Ideal Straight Case, Case A, Case B, Case C. From table 5.10, all cases also demonstrate no obviously different in velocity values at all positions and even in all phases.

#### 5.4.3 Results of Pressure Gradient Observation in the Laminar Steady State Flow

The experiment has been extended by monitoring on the pressure gradient in the laminar steady state flow. This variable has also received considerable in vascular surgery and predictive value for long-term survival of the vein graft model. The experiment has been performed on the same models that applied in the velocity observation. The schematic figure, the monitoring surface and the dimension for the vein graft models can be referred in Figure 5.13 and Table 5.3. The inlet velocity of 12.5 cm/s as the velocity is also applied at the proximal of the vein graft model in all cases for this experiment.

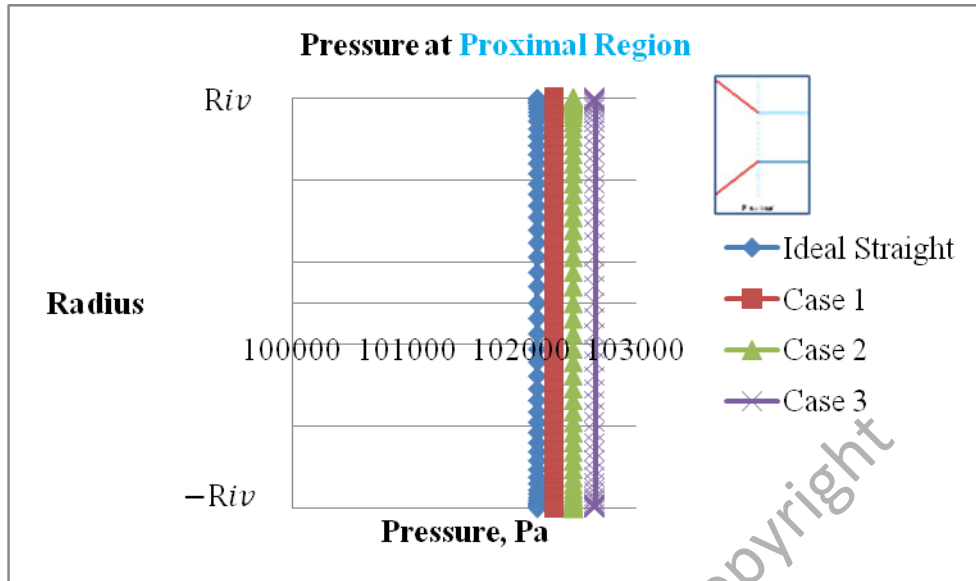


Figure 5.33: The proximal pressure in Ideal Straight, Case 1, Case 2 and Case 3.

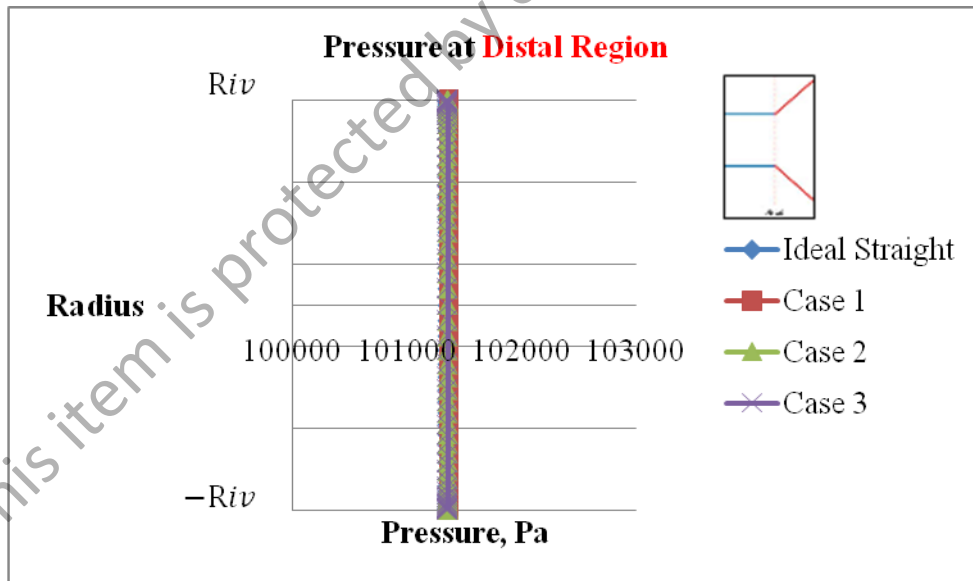


Figure 5.34: The distal pressure in Ideal Straight, Case 1, Case 2 and Case 3.

Table 5.11: Summary of the centre pressure of blood flow at the Proximal and Distal region in Ideal Straight, Case 1, Case 2 and Case 3

	Centre Pressure, $P_o$ (Pa)	
	Proximal	Distal
Ideal Straight	102136	101360
Case 1	102281	101362
Case 2	102449	101360
Case 3	102644	101359

Figure 5.33, Figure 5.34 and Table 5.11 show the proximal and distal pressure in Ideal Straight, Case 1, Case 2 and Case 3. All cases in Figure 5.33 and Figure 5.34 show the highest value in the pressure contribution occur in Case 3.

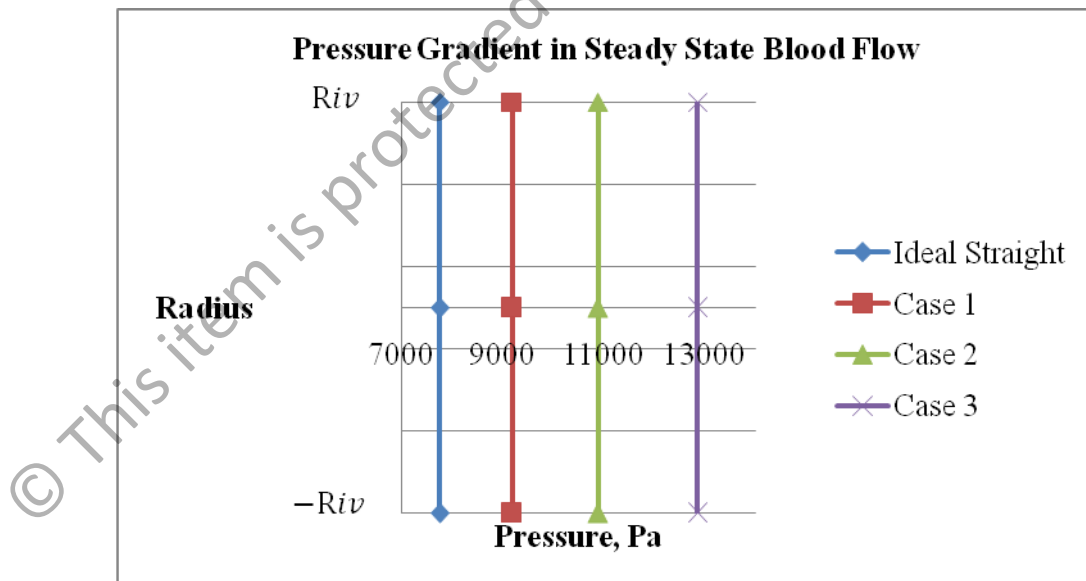


Figure 5.35: The pressure gradient in Ideal Straight, Case 1, Case 2 and Case 3.

Table 5.12 : Summary of the centre of pressure gradient in Ideal Straight, Case 1, Case 2 and Case 3.

	Centre of Pressure Gradient, $\Delta P_o$ (Pa/m)
Ideal Straight	7760
Case 1	9190
Case 2	10890
Case 3	12850

Figure 5.35 shows the pressure gradient in all cases. Based on Table 5.12, the ideal straight demonstrates the lowest pressure gradient. The increase of pressure gradient value is due to the increase of mismatched ratio.

Pressure gradient on the over length kink models have also been monitored. The applied models are also the same as applied for the velocity observation. The blood velocity of 12.5 cm/s is also applied at the proximal region in every vein graft models. For details of the dimension, the schematic figure and the monitoring surface are shown in Table 5.5 and Figure 5.16.

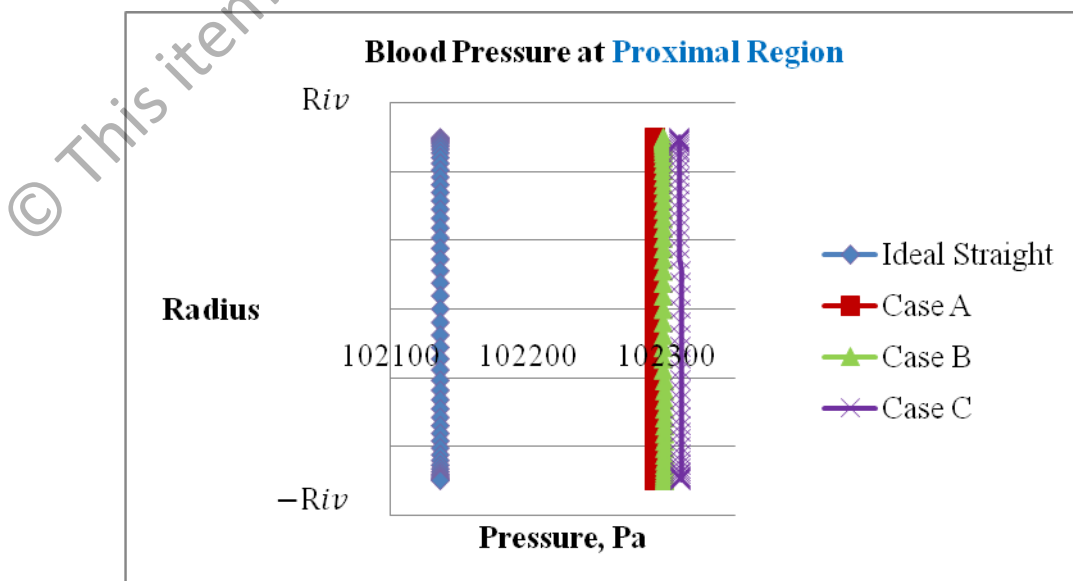


Figure 5.36: The proximal pressure in Ideal Straight, Case A, Case B and Case C.

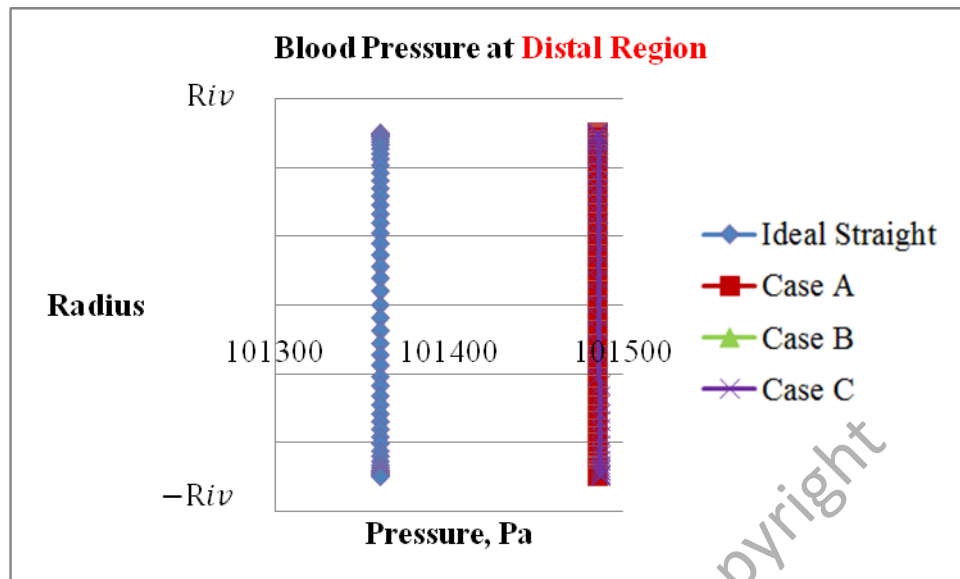


Figure 5.37: The distal pressure in Ideal Straight, Case A, Case B and Case C.

Table 5.13: Summary of the centre pressure of blood flow at the Proximal and Distal region in Ideal Straight, Case A, Case B and Case C

	Centre Pressure, $P_o$ (Pa)	
	Proximal	Distal
Ideal Straight	102135.6	101360.3
Case A	102292	101486
Case B	102298	101486
Case C	102311	101487

Figure 5.36, Figure 5.37 and Table 5.13 show the proximal and distal pressure in Ideal Straight, Case A, Case B and Case C. All cases in Figure 5.33 and 5.34 show the pressure contribution is in vertical form. The lowest value in pressure contribution happens at ideal straight case.

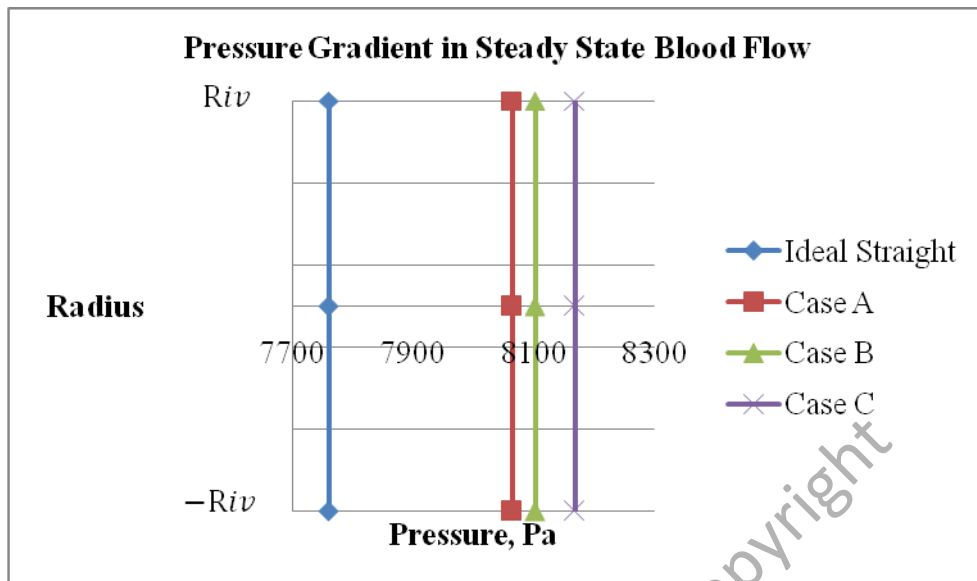


Figure 5.38: The pressure Gradient in Ideal Straight, Case A, Case B and Case C.

Table 5.14: Summary of the centre of pressure gradient for Ideal Straight, Case A, Case B and Case C

	Centre of Pressure Gradient, $\Delta P_o$ (Pa/m)
Ideal Straight	7754
Case A	8052
Case B	8088
Case C	8158

Figure 5.38 shows the pressure gradient in all cases. Based on Table 5.14, the ideal straight still demonstrates the lowest pressure gradient. The increase of amplitude of sinusoidal two cycled wavy RSVG causes the increase of pressure gradient.

#### 5.4.4 Results of Pressure Observation in the Laminar Pulsatile Flow

The experiment has been continued by monitoring the pressure gradient in the laminar pulsatile flow as stated in previous subtopic on velocity observation. In this experiment, the same models in the steady flow experiment are also utilized but the UDF flow and Points surface monitor are applied. The UDF containing 6.25 cm/s for minimum velocity and 18.75 cm/s for maximum velocity is also applied in this experiment at the proximal in all cases.

All dimensions can be referred in Table 5.3. The vein graft model with the point surface monitor is chosen. The schematic figure of the vein graft model that represents models of all cases can be referred in Figure 5.19. The Point is also chosen as the Surface Monitors for pulsatile pressure observation in these models because it is more suitable in monitoring the pulsatile pressure observation compared to Line. These points are placed at the Proximal and Distal of the vein graft models.



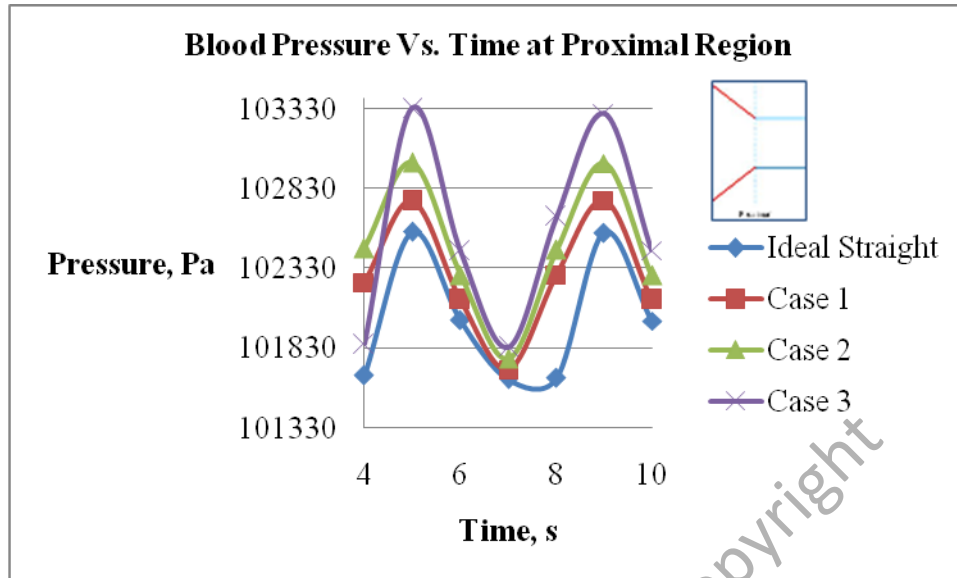


Figure 5.39: The proximal pressure in Ideal Straight, Case 1, Case 2 and Case 3.

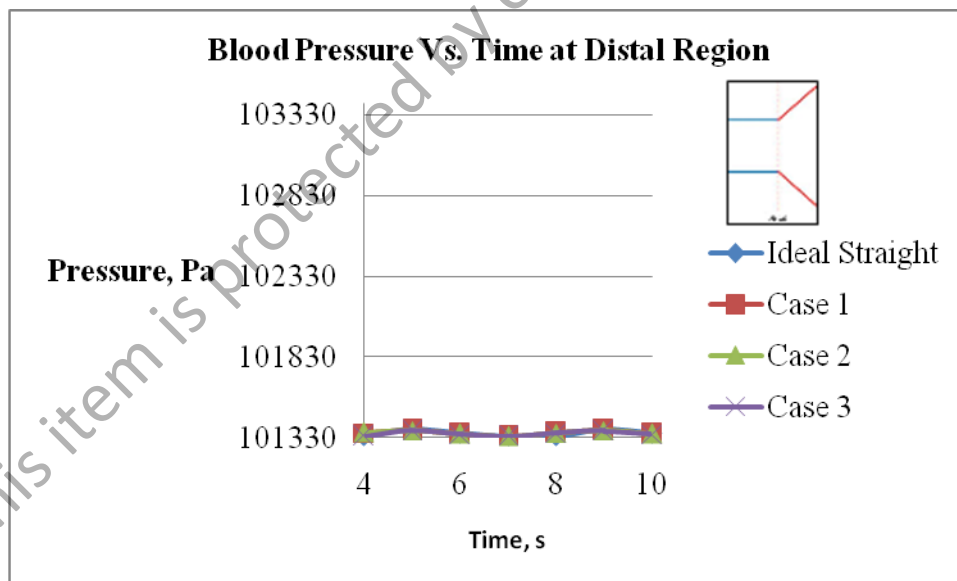


Figure 5.40: The distal pressure in Ideal Straight, Case 1, Case 2 and Case 3.

Table 5.15: Summary of the centre of the pulsatile blood pressure at the Proximal and Distal Region for Ideal Straight, Case 1, Case 2 and Case 3

	Centre Pressure, $P_o$ (Pa)			
	Proximal		Distal	
	Systolic Phase	Diastolic Phase	Systolic Phase	Diastolic Phase
Ideal Straight	102558	101635	101384	101340
Case 1	102754	101695	101379	101339
Case 2	102996	101763	101375	101339
Case 3	103334	101836	101373	101338

Figure 5.39 and Figure 5.40 show the centre of pulsatile blood pressure at the Proximal and Distal region in the vein graft model of all cases. The centre pulsatile blood pressure at the proximal region in Case 3 demonstrates the highest value in this experiment as shown in Table 5.15.

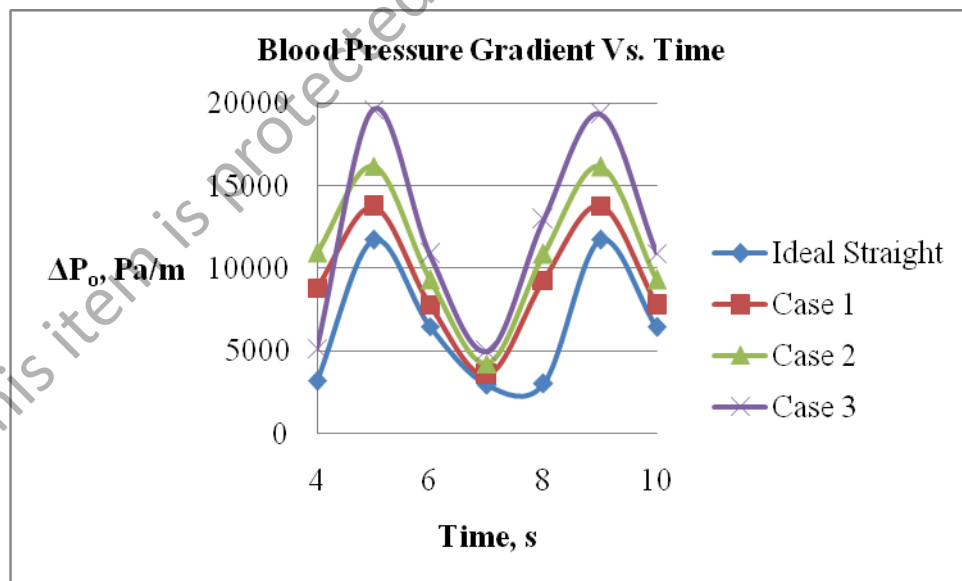


Figure 5.41: The pressure gradient in Ideal Straight, Case 1, Case 2 and Case 3.

Table 5.16: Summary of the centre of pulsatile blood pressure gradient between the Proximal and Distal Region for Ideal Straight, Case 1, Case 2 and Case 3

	Gradient of Centre Pressure, $\Delta P_o$ (Pa/m)	
	Systolic Phase	Diastolic Phase
Ideal Straight	11740	2950
Case 1	13750	3560
Case 2	16210	4240
Case 3	19610	4980

Figure 5.41 shows the pulsatile pressure gradient in all cases. Based on Table 5.16, Case 3 shows the highest reduction at systolic phase in the amplitude of flow wave compared to other cases even in diastolic phase. The mismatched in attachment leads over high speed and high pressure gradient. The ratio of mismatched attachment over than 1:1.1 should be avoided due to out of acceptable tolerance in pressure gradient.

Monitoring in pressure gradient on the Over Length Kink Models was carried out by generating the UDF flow and selecting points as the monitor surface to be used. These points were located at the proximal and distal of the vein graft models. Figure 5.26 and Table 5.5 show the schematic figure and all dimensions of the vein graft model of all cases.

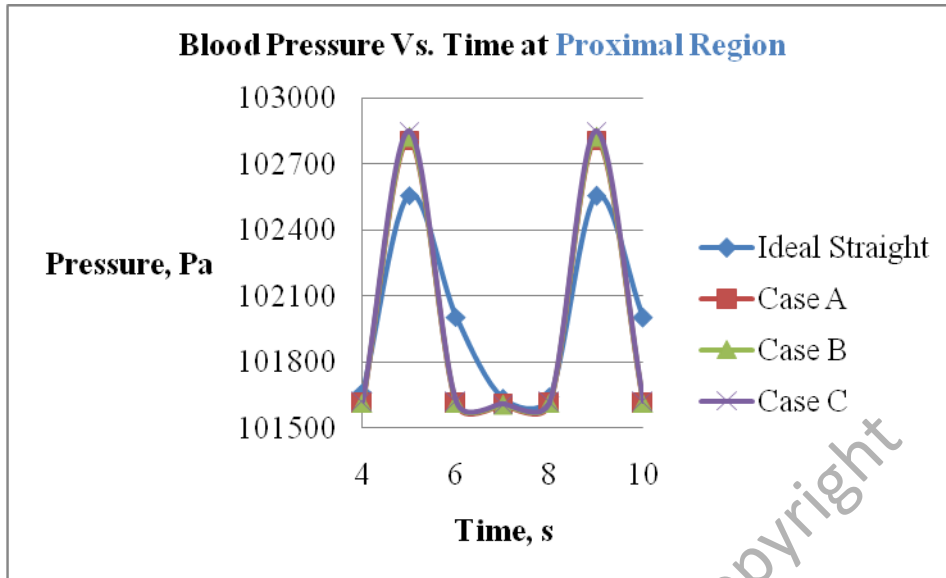


Figure 5.42: The proximal pressure in Ideal Straight, Case A, Case B and Case C

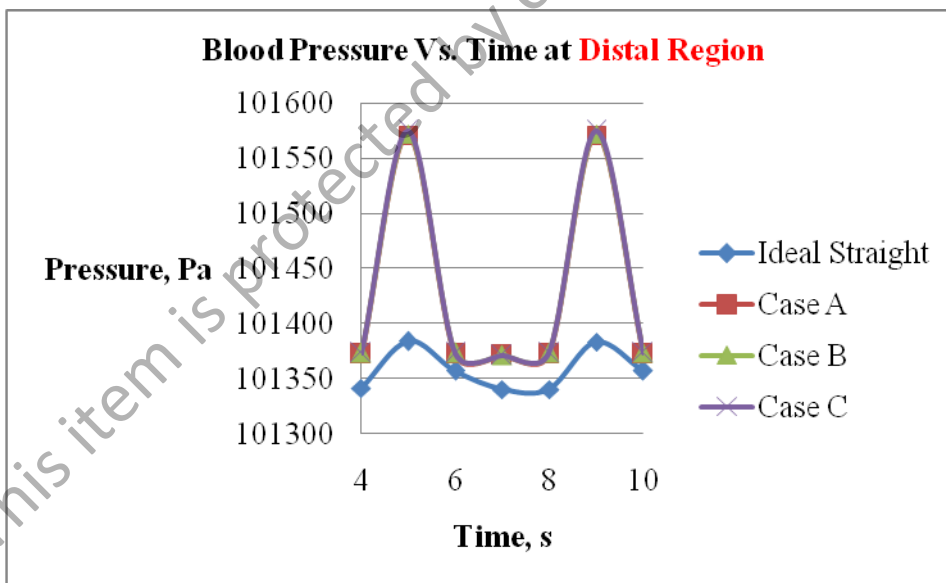


Figure 5.43: The Distal pressure in Ideal Straight, Case A, Case B and Case C

Table 5.17: Summary of the centre of pulsatile blood pressure at the Proximal and Distal Region for Ideal Straight, Case A, Case B and Case C

	Centre Pressure, $P_o$ (Pa)			
	Proximal		Distal	
	Systolic Phase	Diastolic Phase	Systolic Phase	Diastolic Phase
Ideal Straight	102558	101635	101384	101340
Case A	102808	101604	101571	101571
Case B	102822	101604	101572	101572
Case C	102848	101608	101575	101575

Figure 5.42 and Figure 5.43 show the centre of pulsatile blood pressure at the Proximal and Distal region in the vein graft model of all cases. Based on Table 5.17, all irregular vein graft models demonstrate high pressure in systolic phase at the proximal and low pressure in diastolic phase compared to ideal straight case. However, all irregular cases demonstrate high pressure at distal region in systolic and diastolic phase.

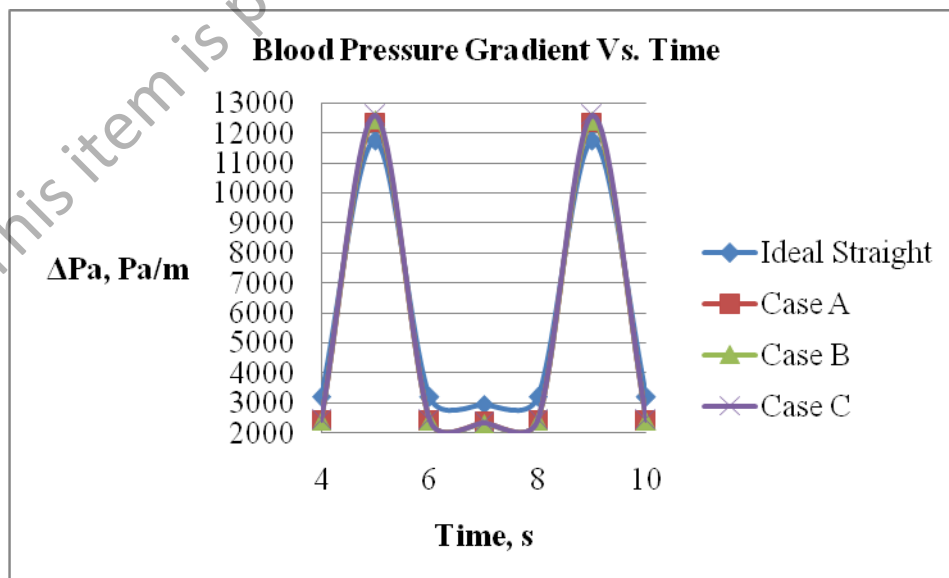


Figure 5.44: The Pressure Gradient in Ideal Straight, Case A, Case B and Case C.

Table 5.18: Summary of the centre of pulsatile blood pressure gradient between the Proximal and Distal Region for Ideal Straight, Case A, Case B and Case C

	Gradient of Centre Pressure, $\Delta P_o$ (Pa/m)	
	Systolic Phase	Diastolic Phase
Ideal Straight	11740	2950
Case A	12358	2328
Case B	12450	2321
Case C	12604	2347

Figure 5.44 shows the pulsatile pressure gradient in all cases. Based on Table 5.18, all irregular geometry cases demonstrate high value in the pressure gradient at systolic phase and low value in the pressure gradient at diastolic phase compared to ideal straight geometry. High pressure gradient at systolic phase and low pressure gradient at diastolic phase in all irregular geometry happen due to curvature geometry and the existing of flow resistance. All kinking cases are not applicable in the procedure because all of them demonstrate high pressure gradient compared to ideal straight case.

#### 5.4.5 Results of the WSS Observation in the Laminar Steady State Flow

The observation is furthered on the wall shear stress in the laminar steady state flow. The WSS also has considerable clinical relevance in vascular surgery and predictive value for long-term survival of the vein graft model (i.e. pressure gradient). This is due to the fact that it provides information about the magnitude of force that the blood exerts on the vessel wall as well as the force exerted by one fluid layer on another which has been debated for several years.

Figure 5.45 shows the schematic figure of the Internal Diameter Mismatched Vein Graft Model that represents the models of Ideal Straight, Case 1, Case 2 and Case C.  $R_{ia}$  is the Artery internal radius,  $O_{ia}$  is the Centre of the artery,  $-R_{ia}$  is the Artery internal radius,  $R_{iv}$  is the Vein internal radius,  $O_{iv}$  is the Centre of the vein,  $-R_{iv}$  is the Vein internal radius and  $L_v$  is the Vein length and it is constant. For the WSS Observation in the Laminar Steady State Flow, a Wall is chosen. The wall is placed at the wall of the vein graft models. The summary of dimension and ratio of attachments for the internal diameter mismatched vein graft models can be referred in Table 5.3 and the inlet velocity of 12.5 cm/s as velocity is also applied at the proximal of the vein graft model in all cases for this experiment.

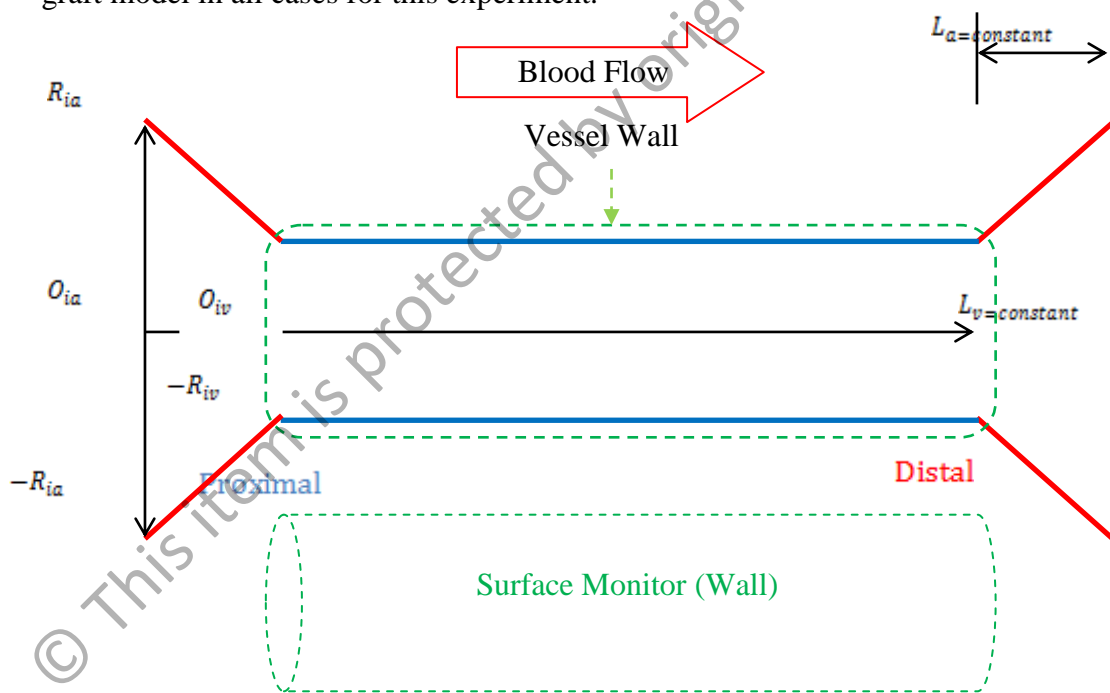
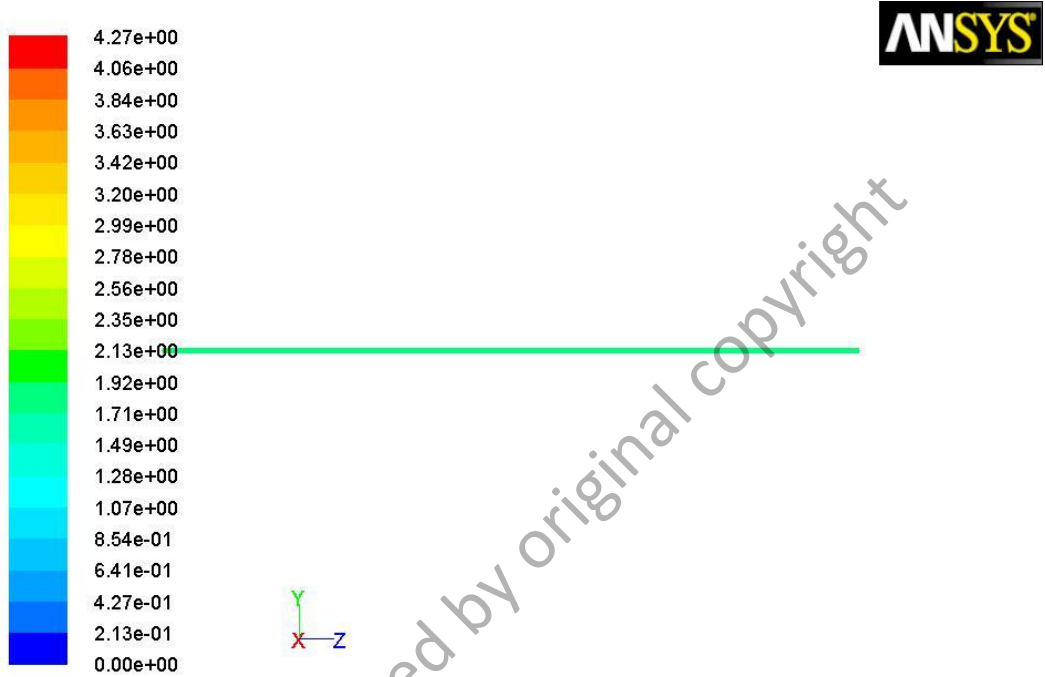


Figure 5.45: The schematic figure of Internal Diameter Mismatched Vein Graft Models and Surface Monitor. The applied type of Surface Monitor at the vessel wall is Wall.

Figure 5.46, 5.47, 5.48 and 5.49 show the WSS in Ideal Straight, Case 1, Case 2 and Case 3. Based on Table 5.19, the highest value of the WSS occurs in Case 3 of the vein graft model and the values of the WSS gradually decrease in Case 2, Case 1 and

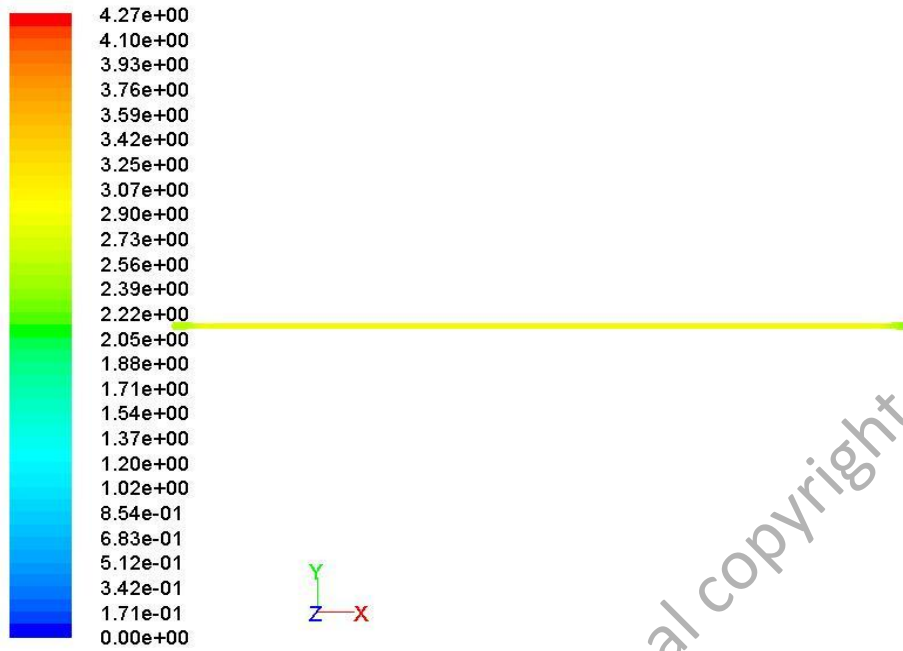
Ideal Straight Case. The increase of the mismatch percentage leads to the increase of pressure gradient.



Contours of the Wall Shear Stress in Ideal Straight Case

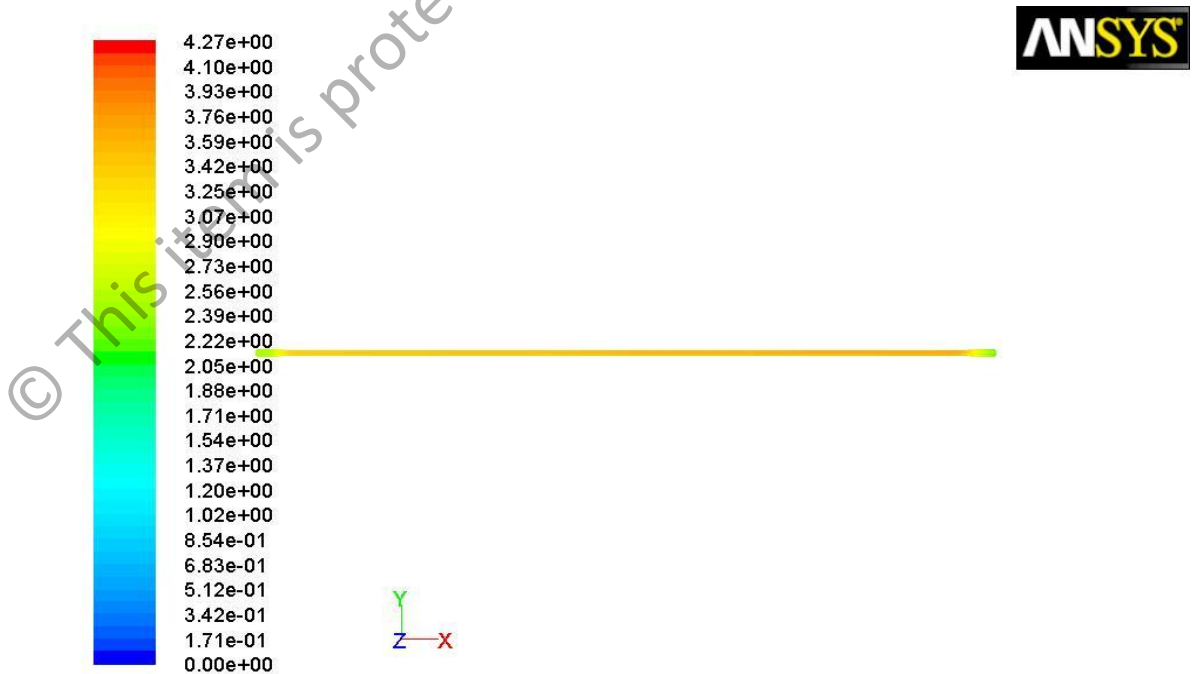
Figure 5.46: Contours of the Wall Shear Stress in the Ideal Straight Case





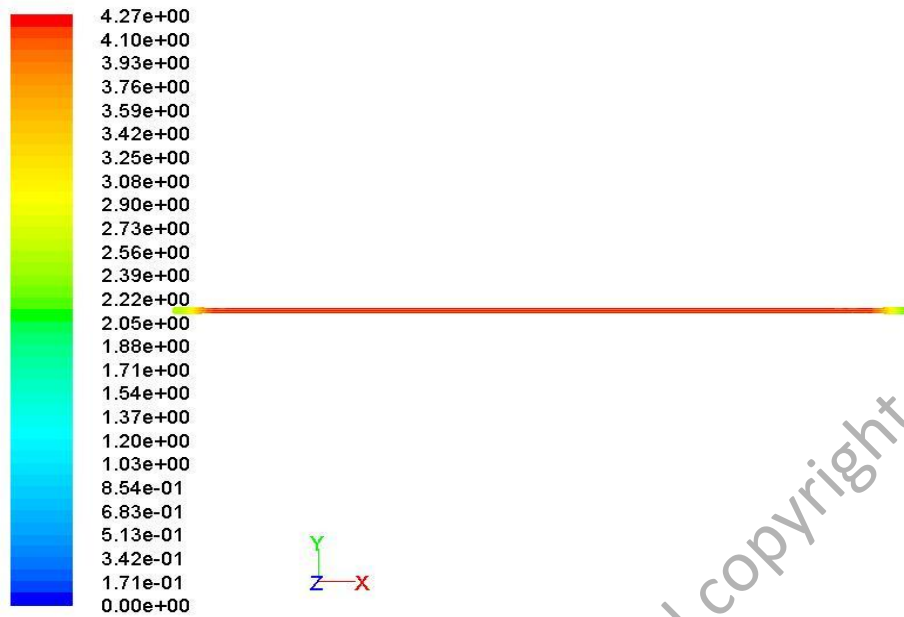
Contours of the Wall Shear Stress in Case 1

Figure 5.47: Contours of the Wall Shear Stress in Case 1



Contours of the Wall Shear Stress in Case 2

Figure 5.48: Contours of the Wall Shear Stress in Case 2



Contours of the Wall Shear Stress in Case 3

Figure 5.49: Contours of the Wall Shear Stress in Case 3

Table 5.19: Summary of the steady WSS at the Wall Region for Ideal Straight, Case 1, Case 2 and Case 3.

	Wall Shear Stress, $\tau_w$ (Pa)
Ideal Straight	2.125
Case 1	3.062
Case 2	3.767
Case 3	4.272

The experiment was furthered on the over length kink models. The 12.5 cm/s is also applied at the proximal region in every vein graft model. For the details of dimensions, the schematic figure and the monitoring surface are shown in Table 5.5 and Figure 5.50. Where  $R_{iv}$  is the Vein internal radius,  $O_{iv}$  is the Centre of the vein,  $-R_{iv}$  is the Vein internal radius and  $a$  is the amplitude height.

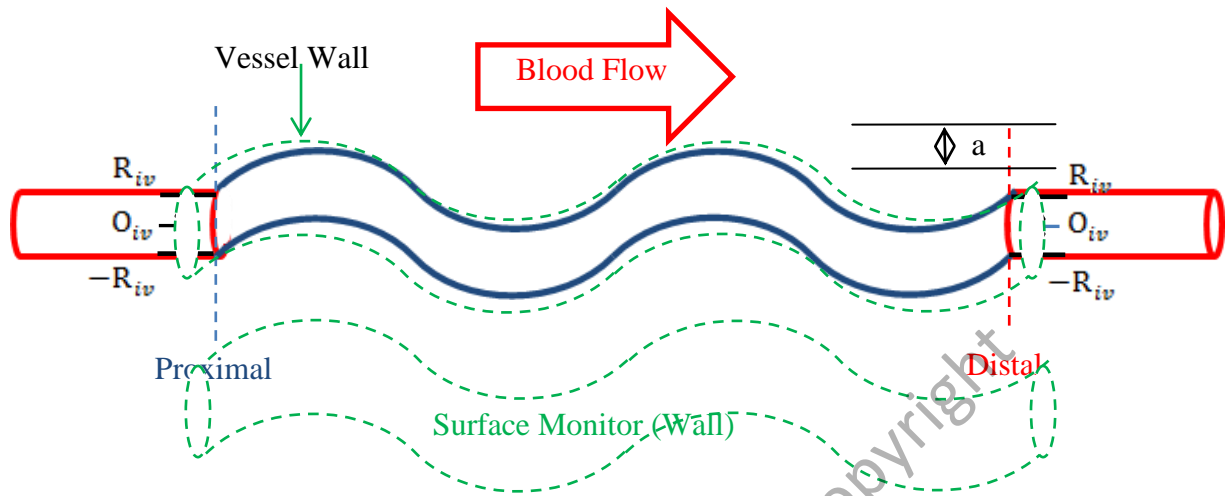
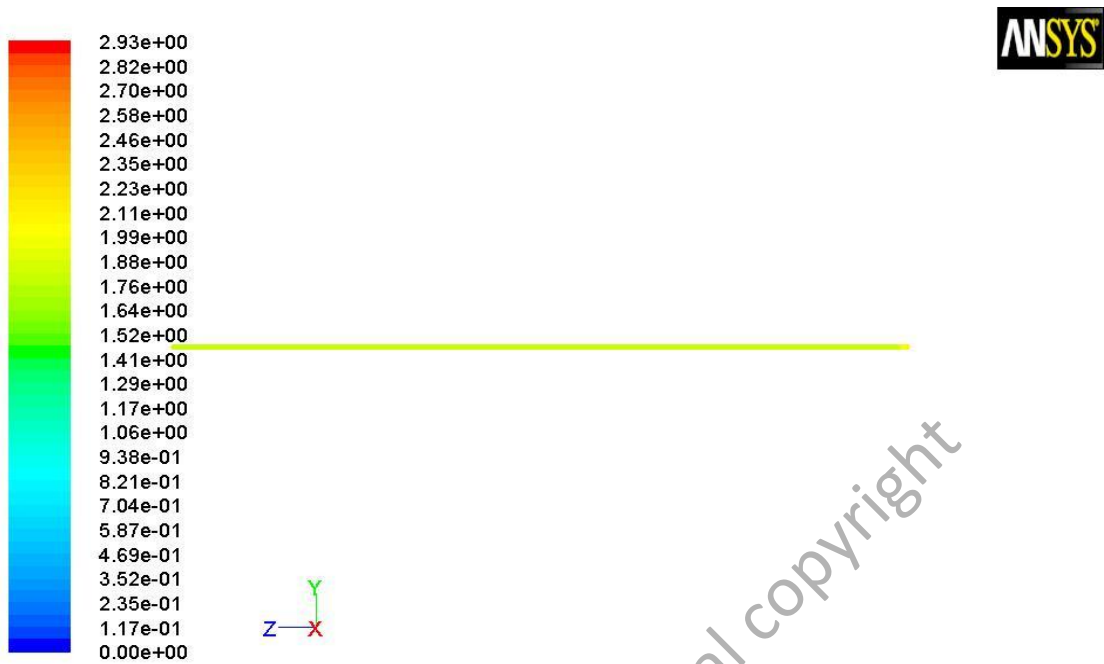


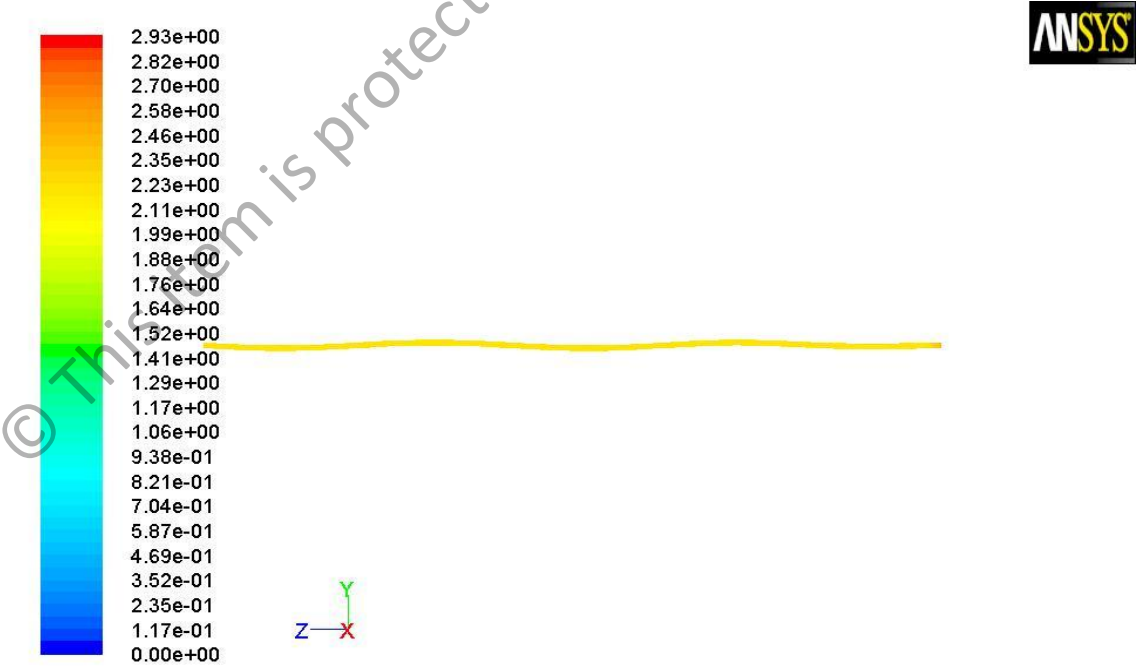
Figure 5.50: The Schematic Figure of the Over Length Kinked Vein Graft Models and the Surface Monitor. The applied type of Surface Monitors at the Proximal and Distal is Wall.

Figure 5.51, 5.52, 5.53 and 5.54 show the WSS in Ideal Straight, Case A, Case B and Case C. Based on Table 5.20, the lowest value of the WSS occurs at ideal straight case of the vein graft model and the values of the WSS gradually increase in Case A, Case B and Case C. The increase of the WSS value is due to the increase in the blood flow resistance or amplitude height of the curvature and pressure gradient.



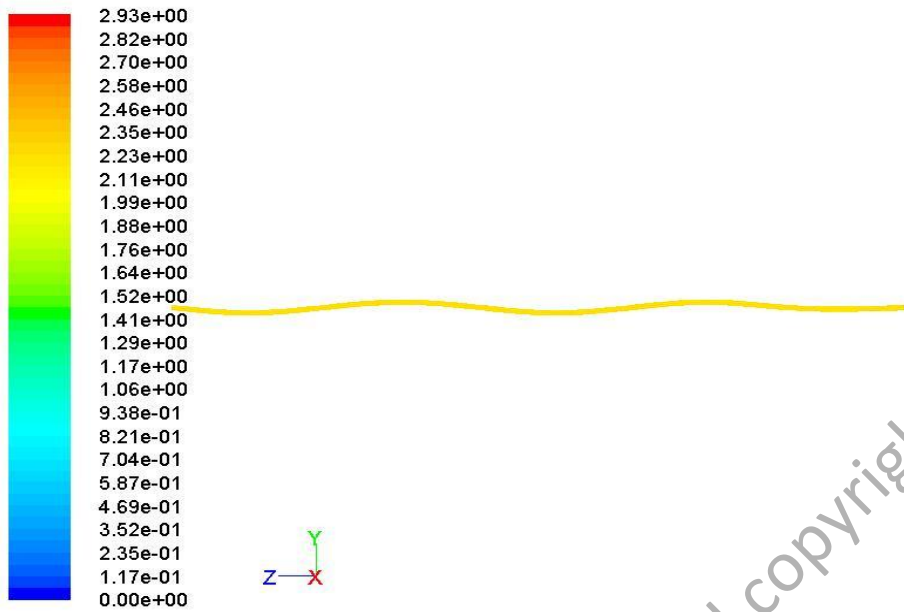
Contours of the Wall Shear Stress in Ideal Straight Case

Figure 5.51: Contours of the Wall Shear Stress in Ideal Straight Case



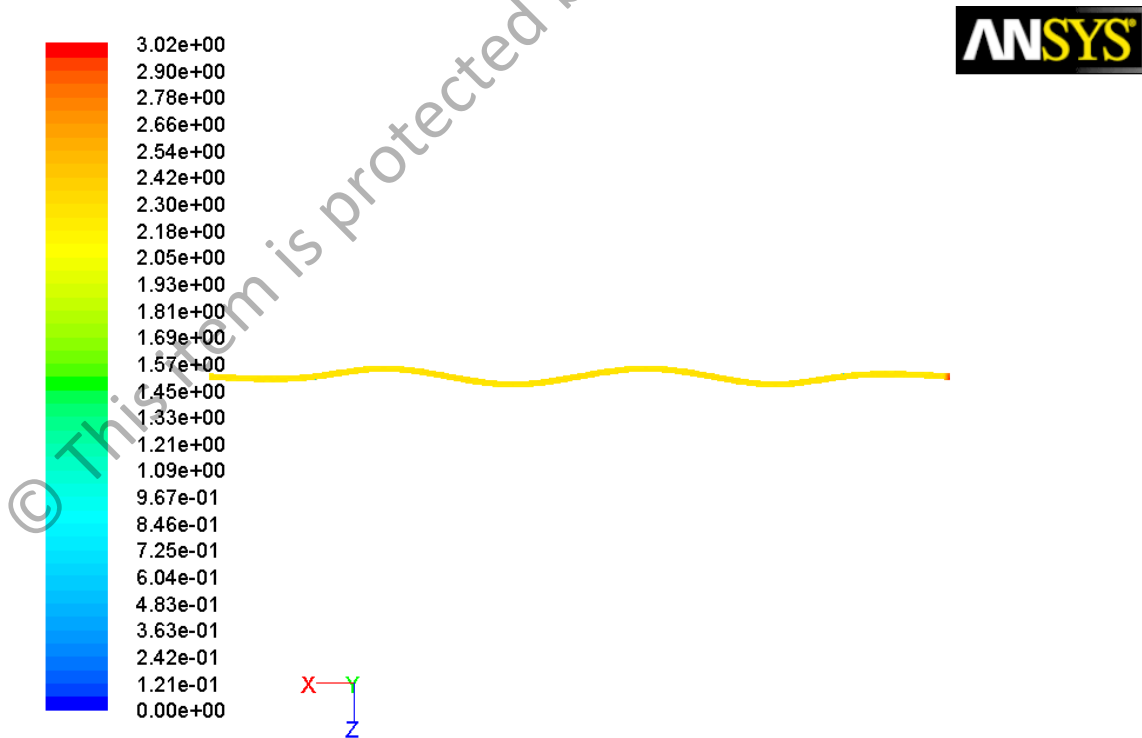
Contours of the Wall Shear Stress in Case A

Figure 5.52: Contours of the Wall Shear Stress in Case A



Contours of the Wall Shear Stress in Case B

Figure 5.53: Contours of the Wall Shear Stress in Case B



Contours of the Wall Shear Stress in Case C

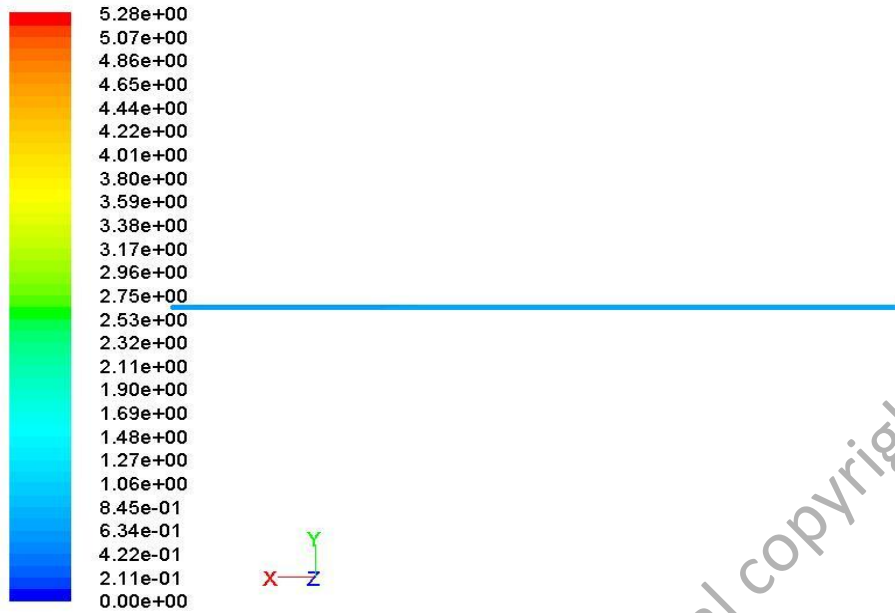
Figure 5.54: Contours of the Wall Shear Stress in Case C

Table 5.20: Summary of the steady WSS at the Wall Region for Ideal Straight, Case A, Case B and Case C.

	Wall Shear Stress, $\tau_w$ (Pa)
Ideal Straight	2.125
Case A	2.521
Case B	2.514
Case C	2.563

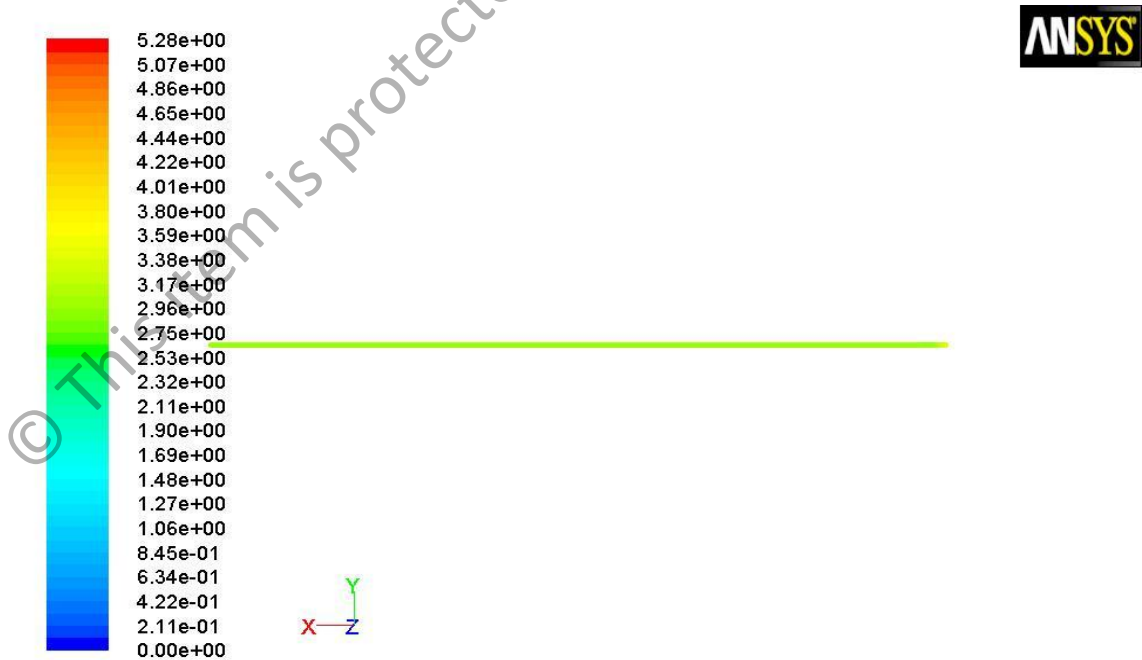
#### 5.4.6 Result of the WSS Observation in the Laminar Pulsatile Flow

The experiment on Internal Diameter Mismatched Vein Graft Models has been continued on the WSS Observation in the Laminar Pulsatile Flow. In this experiment, the same models and surface monitor in the WSS Steady Flow experiment are used but the UDF flow is applied. The schematic figure, the surface monitor and the ratio of attachments for the vein graft model that represents the models of all cases can be referred in Figure 5.3 and Table 5.3. The UDF containing 6.25cm/s for minimum velocity and 18.75 cm/s for maximum velocity for maximum is also applied in this experiment at the proximal in all cases as previous laminar pulsatile flow experiment.



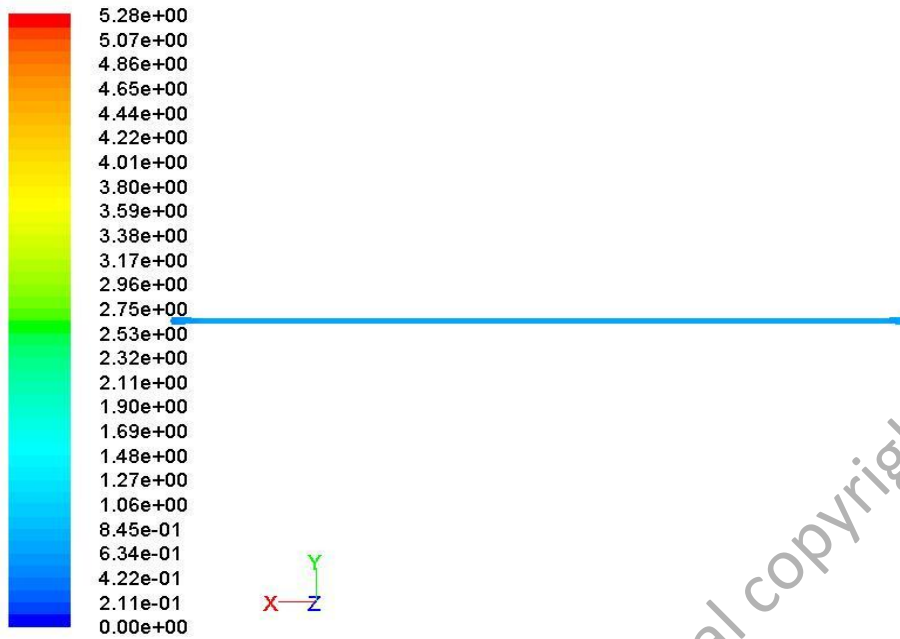
Contours of the Wall Shear Stress at Diastolic Phase in Ideal Straight Case

Figure 5.55: Contours of the Wall Shear Stress in Ideal Straight Case at Diastolic



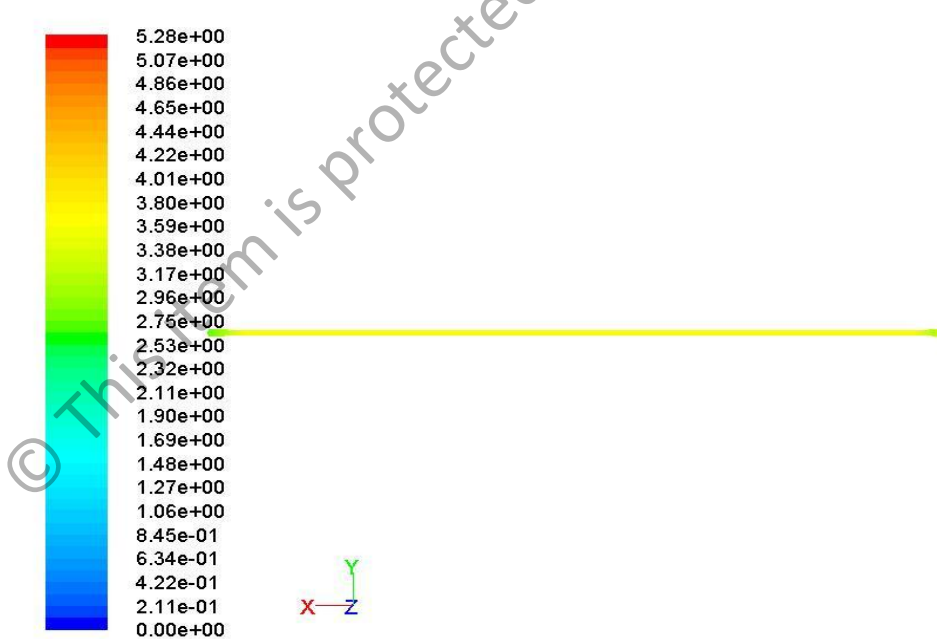
Contours of the Wall Shear Stress at Systolic Phase in Ideal Straight Case

Figure 5.56: Contours of the Wall Shear Stress in Ideal Straight Case at Systolic Phase



Contours of the Wall Shear Stress at Diastolic Phase in Case 1

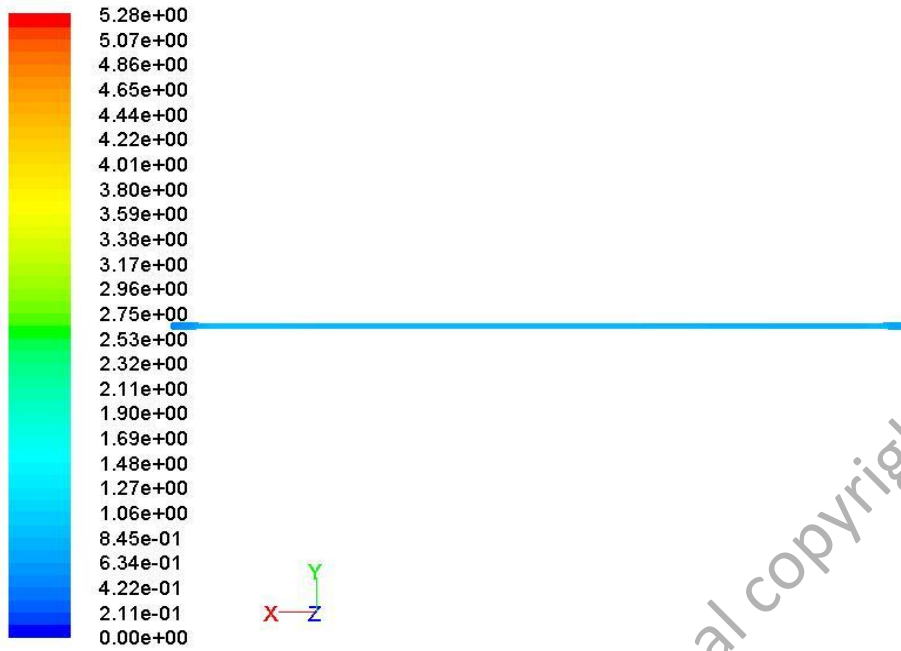
Figure 5.57: Contours of the Wall Shear Stress in Case 1 at Diastolic Phase



Contours of the Wall Shear Stress at Systolic Phase in Case 1

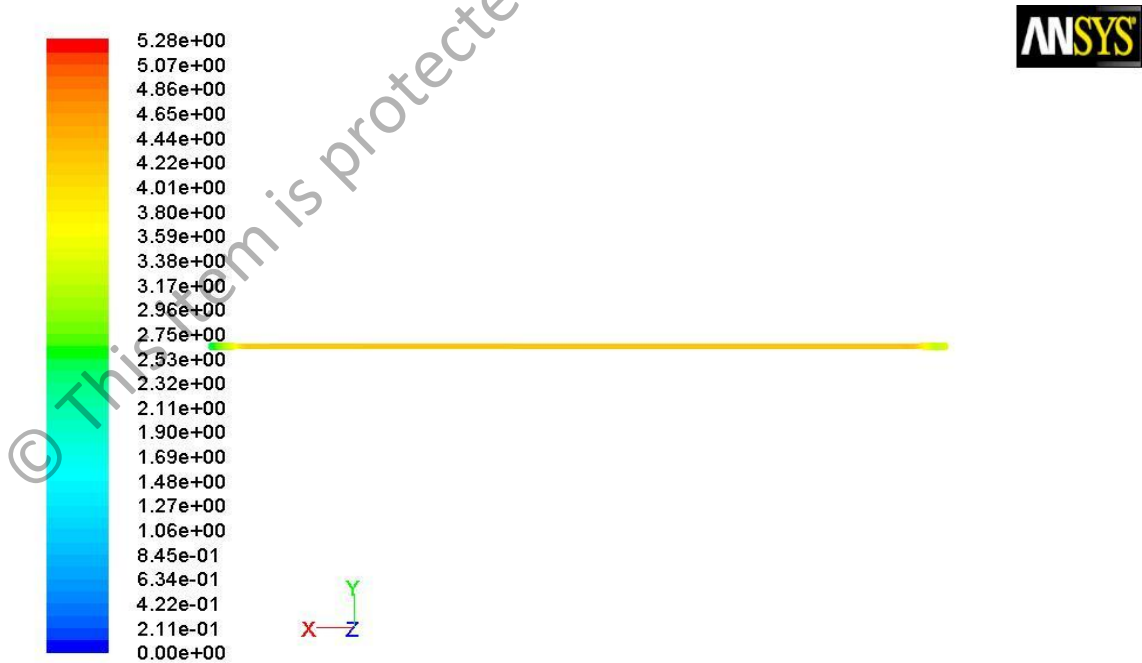
Figure 5.58: Contours of the Wall Shear Stress in Case 1 at Systolic Phase





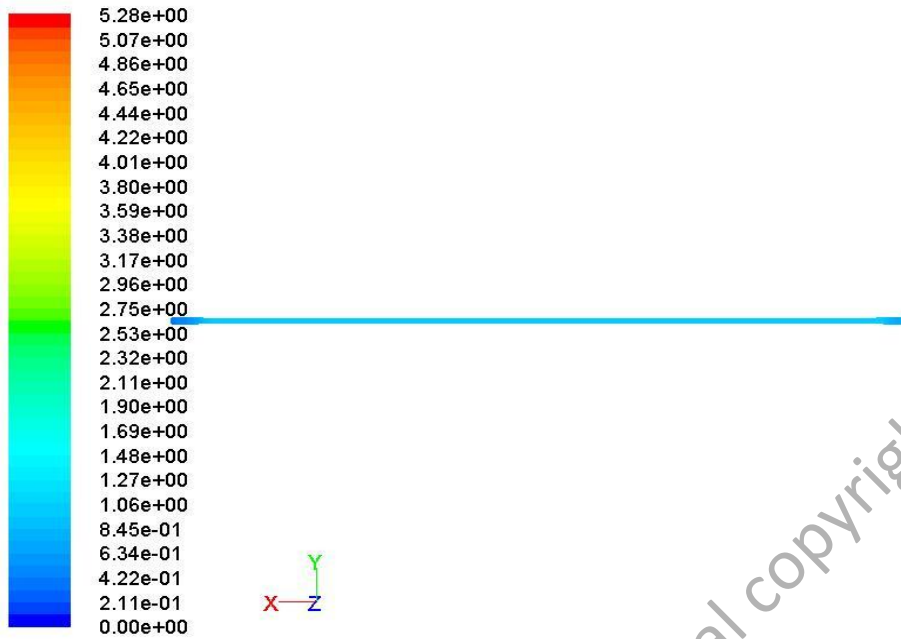
Contours of Wall Shear Stress at Diastolic Phase in Case 2

Figure 5.59: Contours of Wall Shear Stress in the Case 2 at Diastolic Phase



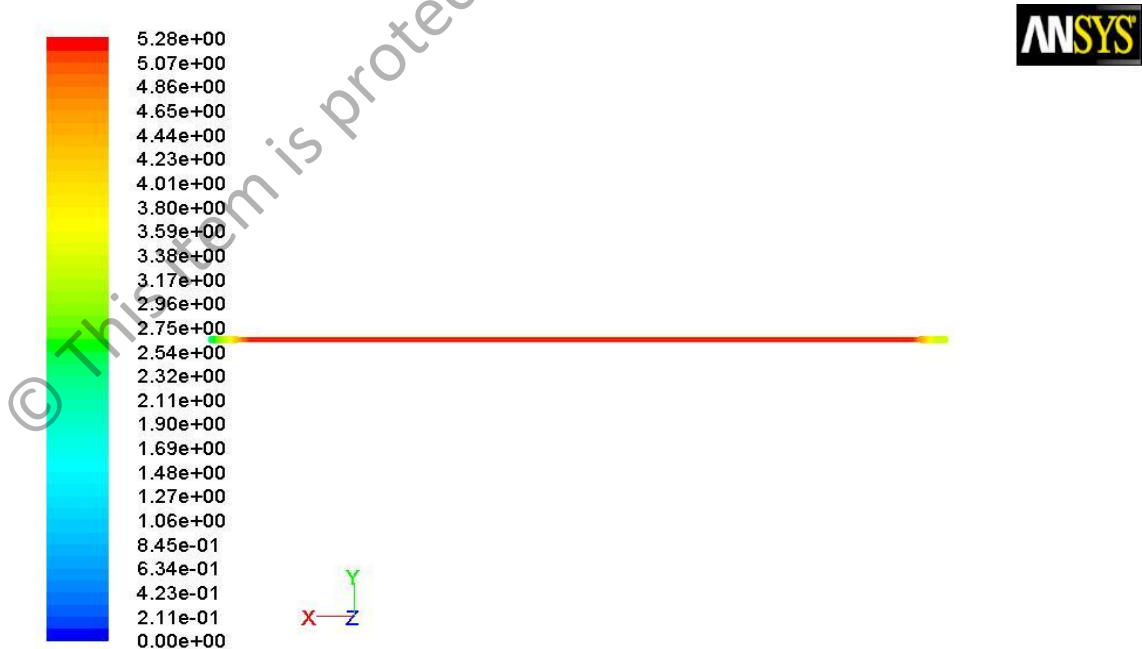
Contours of the Wall Shear Stress at Systolic Phase in Case 2

Figure 5.60: Contours of the Wall Shear Stress in Case 2 at Systolic Phase



Contours of the Wall Shear Stress at Diastolic Phase in Case 3

Figure 5.61: Contours of the Wall Shear Stress in Case 3 at Diastolic Phase



Contours of the Wall Shear Stress at Systolic Phase in Case 3

Figure 5.62: Contours of the Wall Shear Stress in Case 3 at Systolic Phase

Table 5.21: Summary of the pulsatile WSS at the Wall Region for Ideal Straight, Case 1, Case 2 and Case 3.

	Wall Shear Stress, $\tau_w$ (Pa)	
	Systolic Phase	Diastolic Phase
Ideal Straight	3.636	1.005
Case 1	3.640	0.906
Case 2	4.362	0.957
Case 3	5.283	1.073

Figure 5.55, 5.56, 5.57, 5.58, 5.59, 5.60, 5.61 and 5.62 show the WSS in Ideal Straight, Case 1, Case 2 and Case 3. Based on Table 5.21, the highest value of the WSS occurs in Case 3 of the vein graft model at systolic phase. However, there were no significant difference in values of the WSS in Ideal Straight Case, Case A, Case B and Case C at diastolic phase. The over speed (out of acceptable range) in blood flow and high pressure gradient will affect the WSS values.

Monitoring in the WSS was carried on the Over Length Kink Models. The generation of the UDF flow and selection of walls as monitor surface are also used. Figure 5.50 and Table 5.5 show the schematic figure and all dimensions of the vein graft model for all cases.

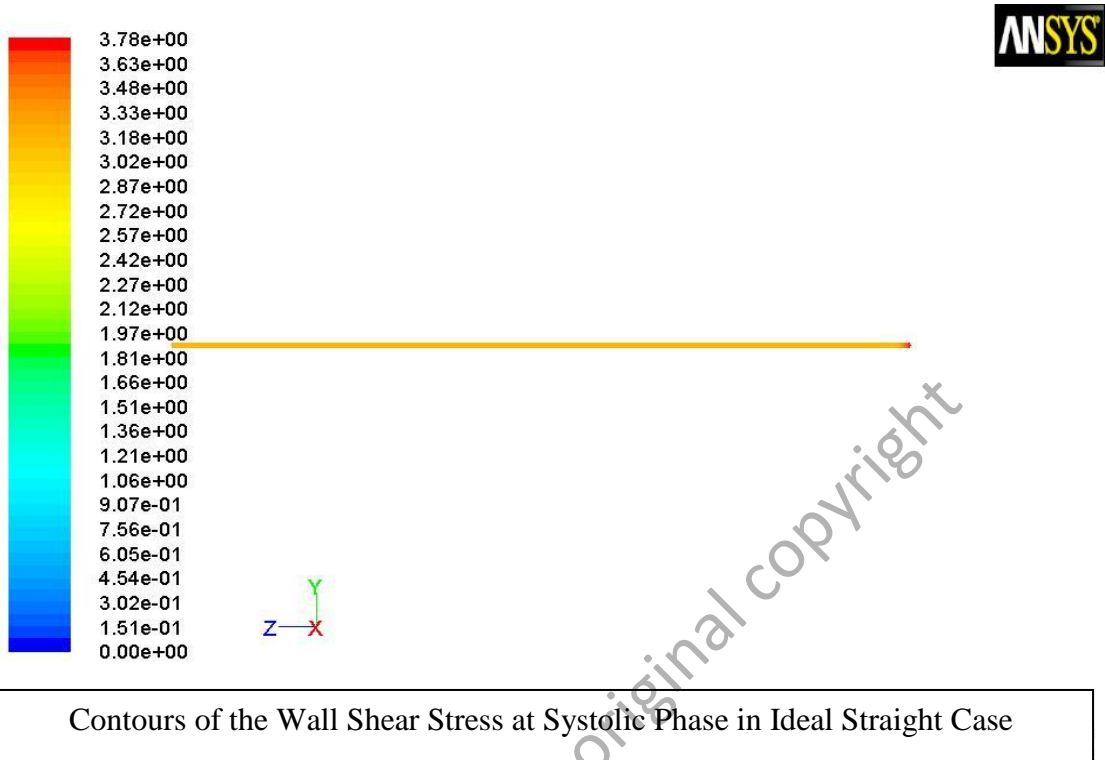


Figure 5.63: Contours of the Wall Shear Stress in Ideal Straight Case at Systolic Phase.

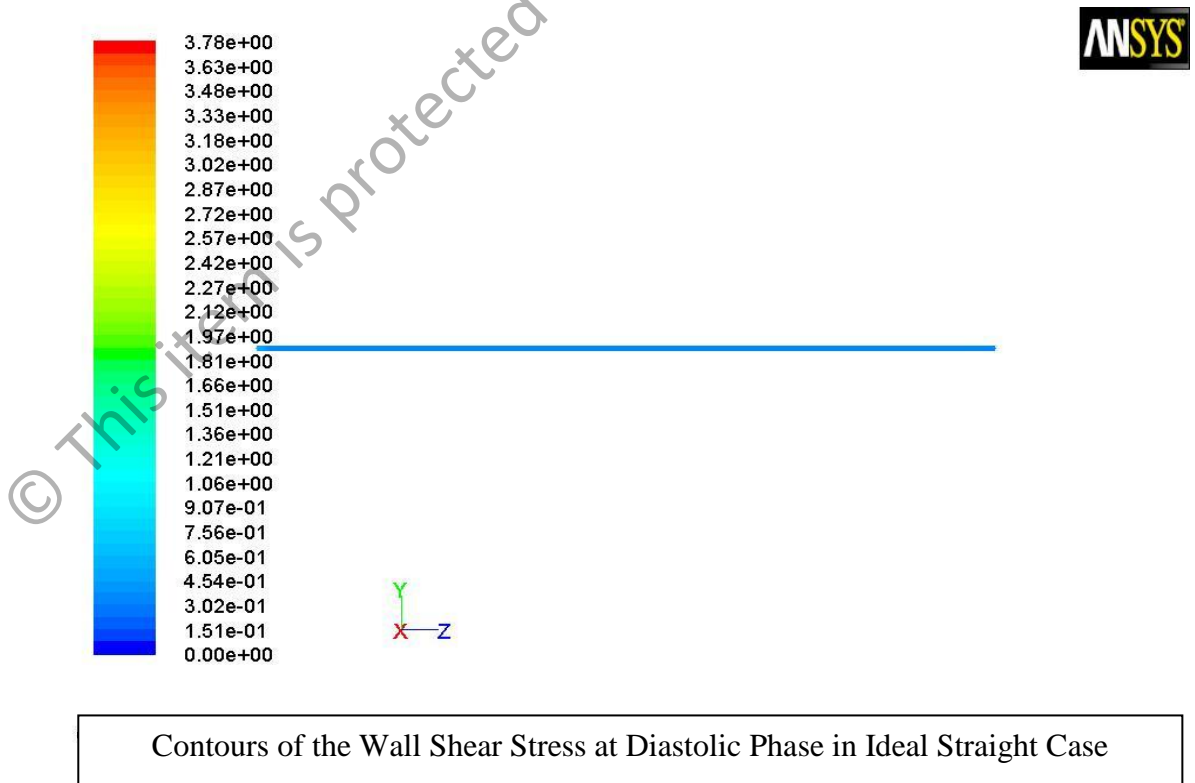
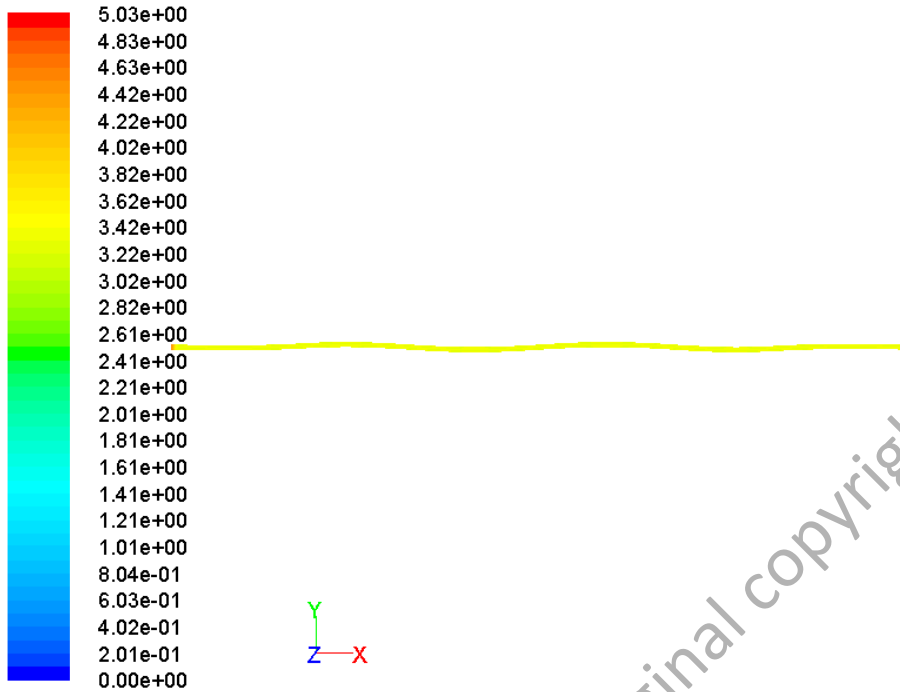


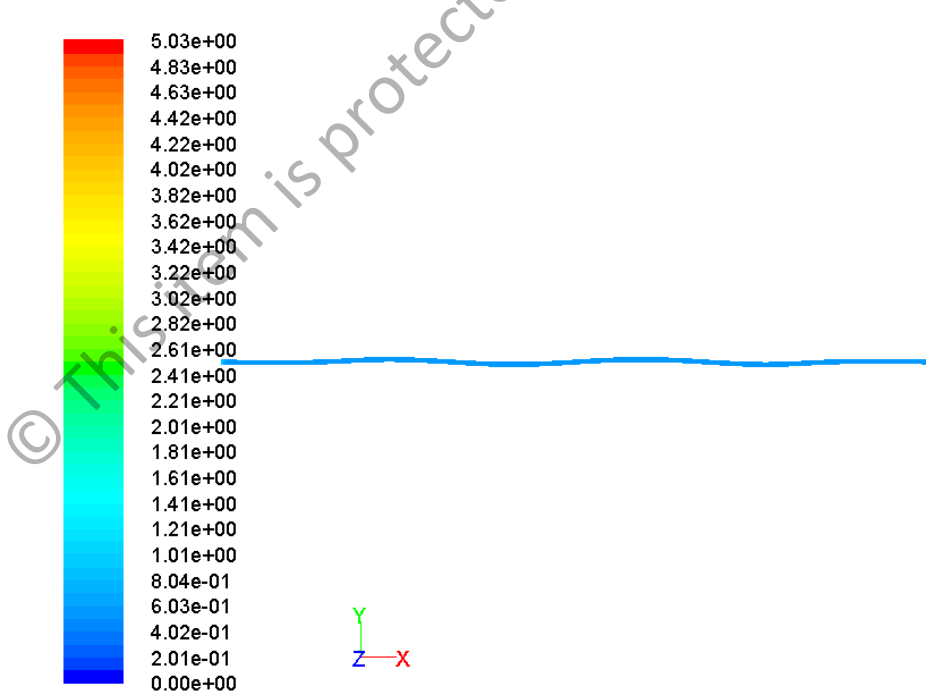
Figure 5.64: Contours of the Wall Shear Stress in Ideal Straight Case at Diastolic

Phase.



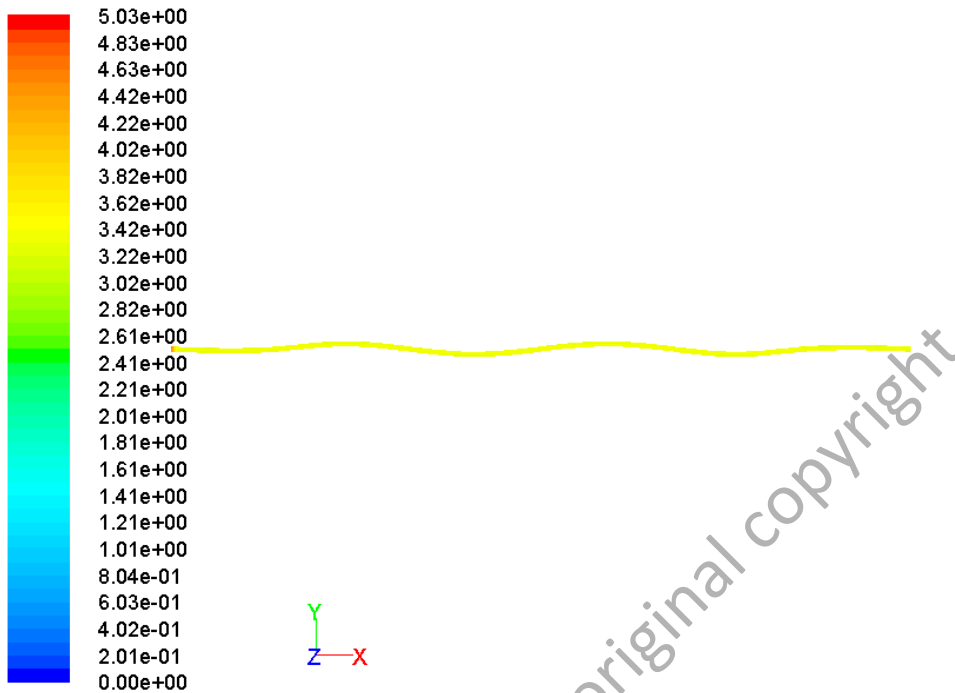
Contours of the Wall Shear Stress at Systolic Phase in Case A

Figure 5.65: Contours of the Wall Shear Stress in Case A at Systolic Phase.



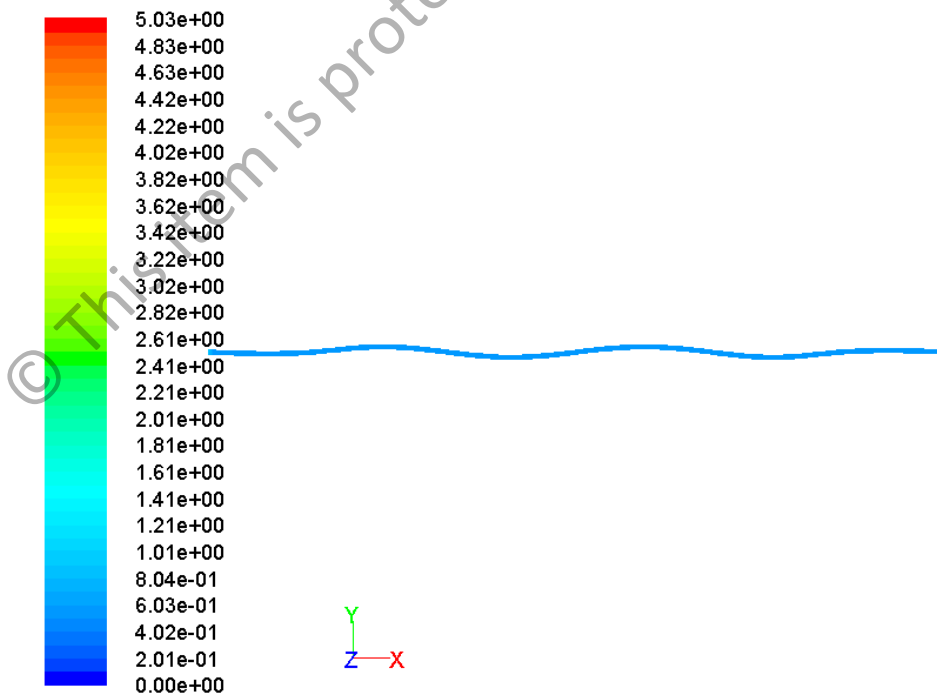
Contours of the Wall Shear Stress at Diastolic Phase in Case A

Figure 5.66: Contours of the Wall Shear Stress in Case A at Diastolic Phase



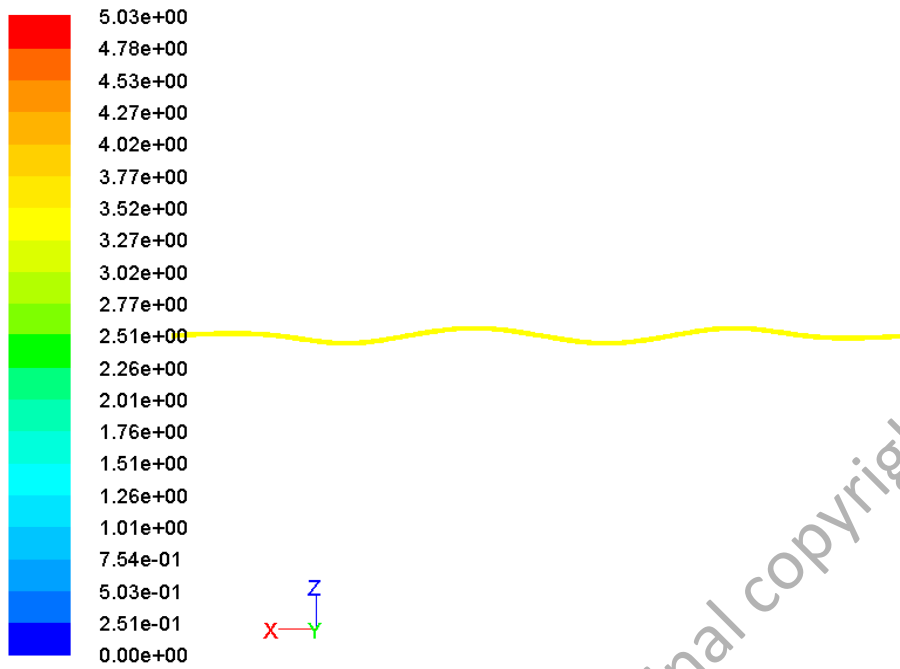
Contours of the Wall Shear Stress at Systolic Phase in Case B

Figure 5.67: Contours of the Wall Shear Stress in Case B at Systolic Phase



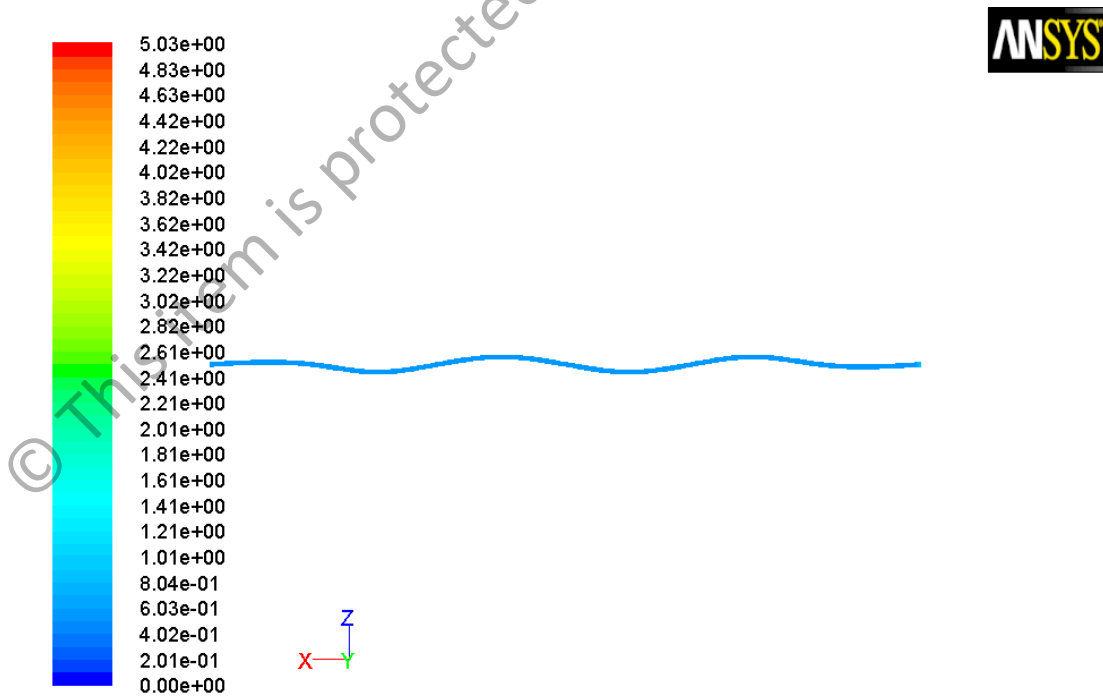
Contours of the Wall Shear Stress at Diastolic Phase in Case B

Figure 5.68: Contours of the Wall Shear Stress in Case B at Diastolic Phase



Contours of the Wall Shear Stress at Systolic Phase in Case C

Figure 5.69: Contours of the Wall Shear Stress in Case C at Systolic Phase.



Contours of the Wall Shear Stress at Diastolic Phase in Case C

Figure 5.70: Contours of the Wall Shear Stress in Case C at Diastolic Phase.

Table 5.22 : Summary of the pulsatile WSS at the Wall Region for Ideal Straight, Case A, Case B and Case C.

	Wall Shear Stress, $\tau_w$ (Pa)	
	Systolic Phase	Diastolic Phase
Ideal Straight	3.636	1.0050
Case A	4.023	0.7250
Case B	4.030	0.7310
Case C	4.120	0.7530

Figure 5.63, 5.64, 5.65, 5.66, 5.67, 5.68, 5.69 and 5.70 show the pulsatile WSS in all cases. Based on Table 5.22, all irregular cases demonstrate higher WSS value compare to ideal straight case at systolic phase, but lower WSS value at diastolic phase compare to ideal straight case. From the observation, the curvature in geometry causes high pressure gradient which leads to high WSS value.

### 5.5 Result and Discussion of the Irregular Vein Graft Models

The discussion of results focuses on the blood velocity, blood pressure gradient and the WSS in irregular vein graft models and the long-term effects in thrombosis re-formation. Ideal Straight Case, Case 1, Case 2 and Case 3 are presented in mismatched percentage. Ideal Straight Case is represented by mismatched percentage 0%. Case 1, Case 2 and Case 3 are represented by 10%, 20% and 30% respectively.

Meanwhile, for the Ideal Straight Case, Case A, Case B and Case C are presented in amplitude height. The amplitude height of 0R, 1R, 2R and 3R represents the Ideal Straight Case, Case A, Case B and Case C, respectively, where R is 0.05cm.



## 5.5.1 Result and Discussion on the Velocity Observation in Irregular Vein Graft

### Models

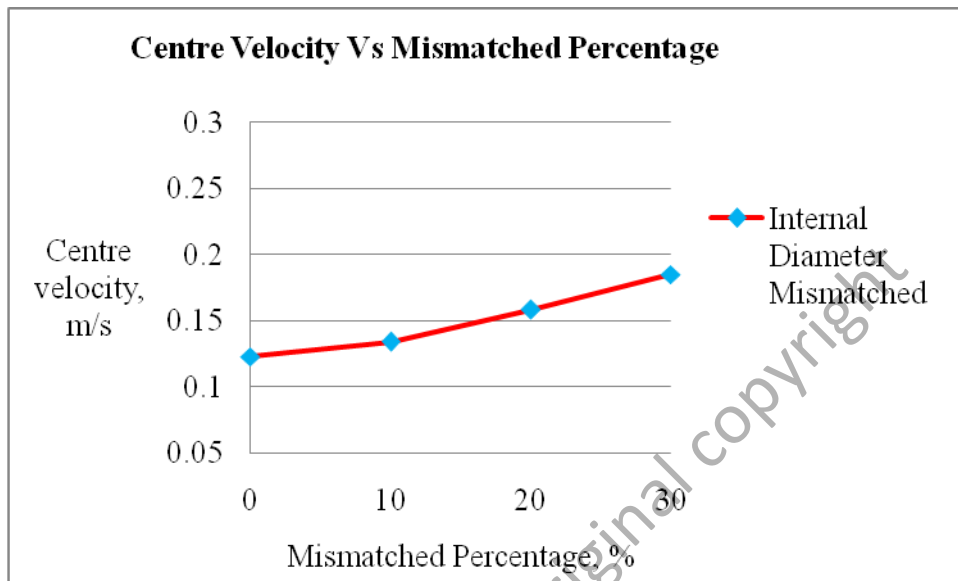


Figure 5.71: The Centre velocity in different percentage or cases of the internal diameter mismatched model

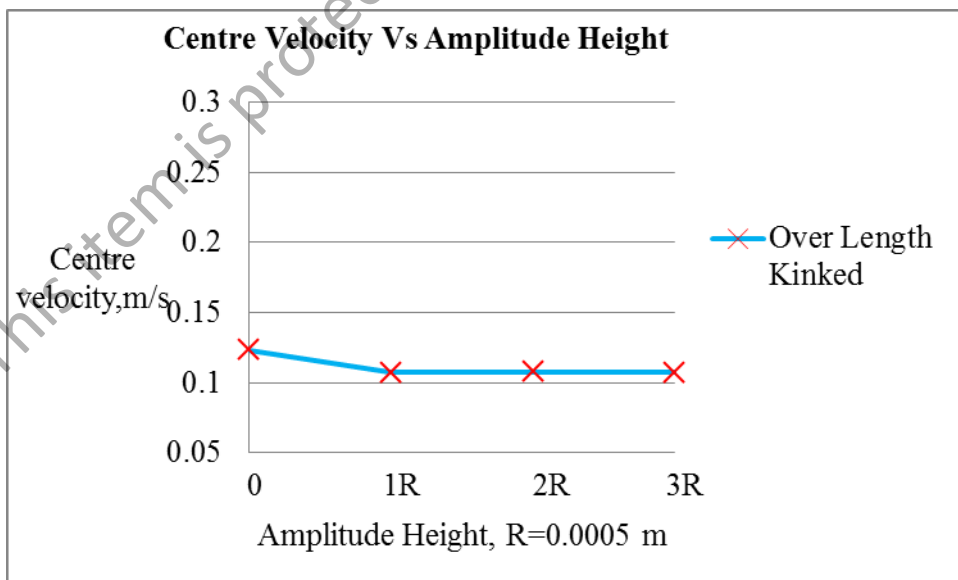


Figure 5.72: The Centre velocity in different amplitude or cases of the over length kinked model

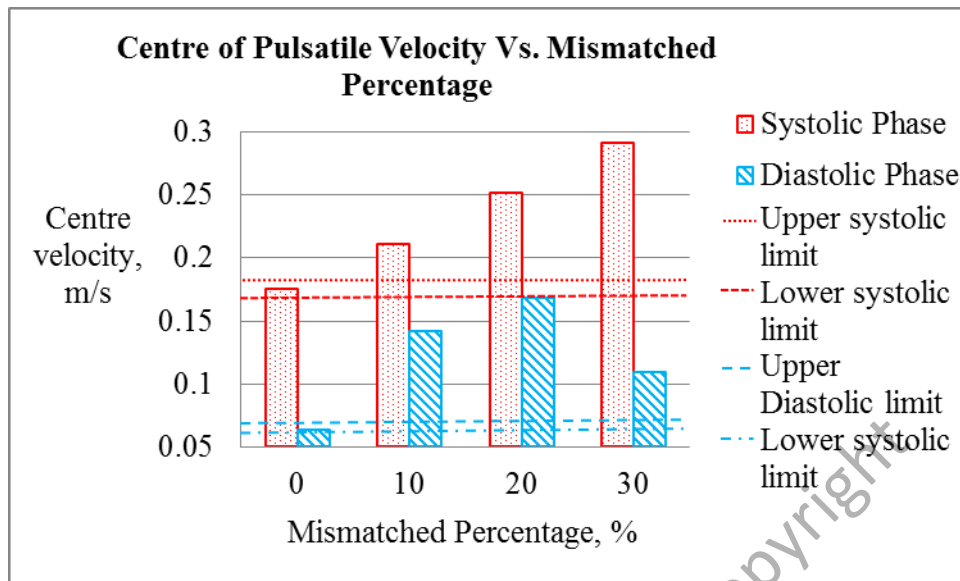


Figure 5.73 : The Centre pulsatile velocity in different percentage or cases of the internal diameter mismatched model.

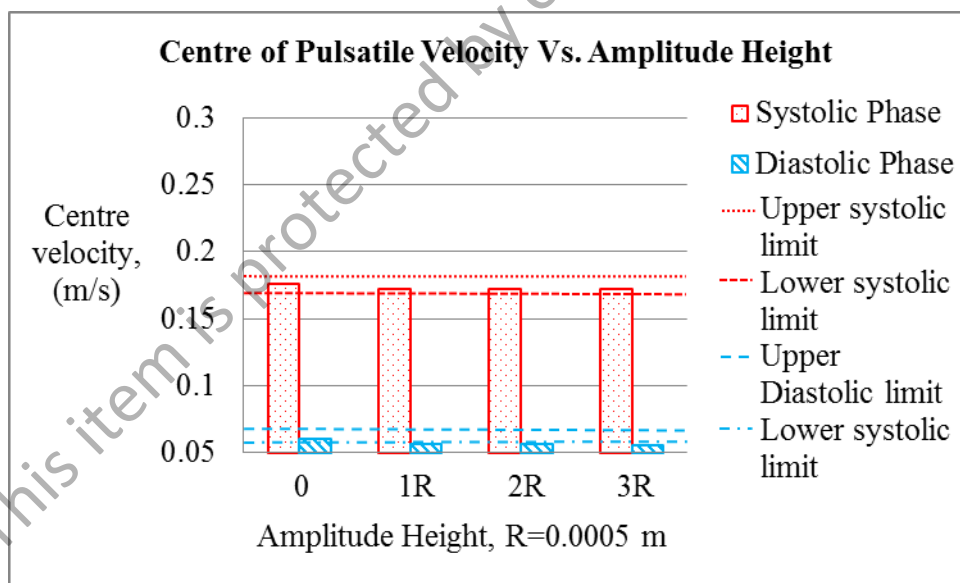


Figure 5.74 : The Centre pulsatile velocity in different amplitude or cases of the over length kinked model

All mismatched cases demonstrate high value in velocity due to discrepancy in the cross section between the artery and vein as shown in Figure 5.71 and Figure 5.73. It happens because the blood being pushed (force through) at higher speed from the

wide arterial vessel to the narrow vein (Wilmer et al., 1998). Meanwhile, all kinking cases demonstrate low value in velocity due to similarity in the cross section between the artery-vein attachment and the curvature geometry as shown in Figure 5.72 and Figure 5.74.

The mismatched and kinked wavy sinusoidal veins should reach below than 10% and 1R amplitude height in order to ensure it is applicable for the vein grafting procedure. This is because the blood flows through those models are too fast in over than 10% mismatched models at systolic and diastolic phase and too slow in over than 1R amplitude height of the kinking model at diastolic phase.

### 5.5.2 Result and Discussion on the Pressure Gradient Observation in the Irregular Vein Graft Models

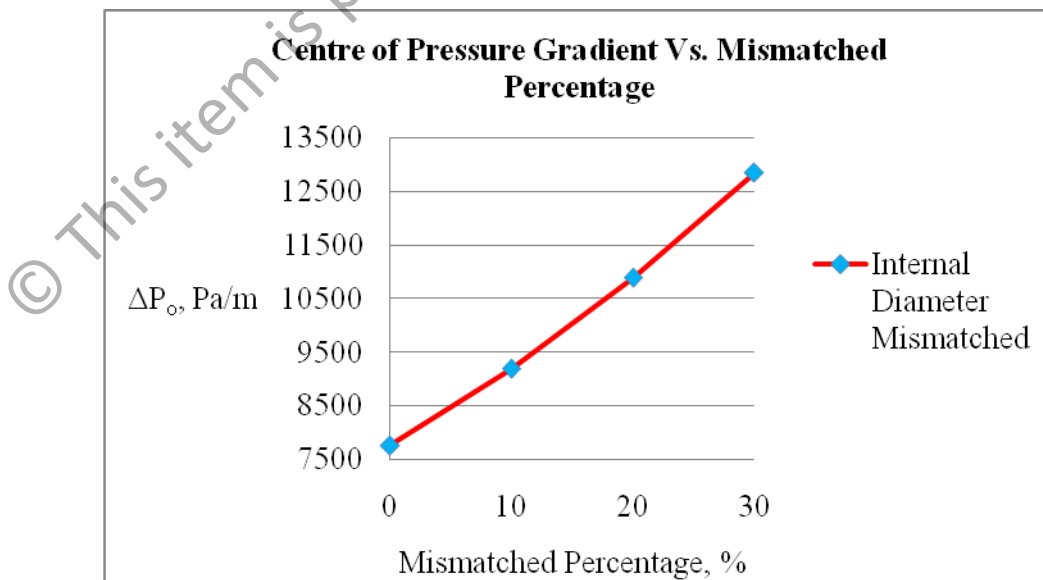


Figure 5.75 : The centre of pressure gradient in different percentage or cases of the internal diameter mismatched model.

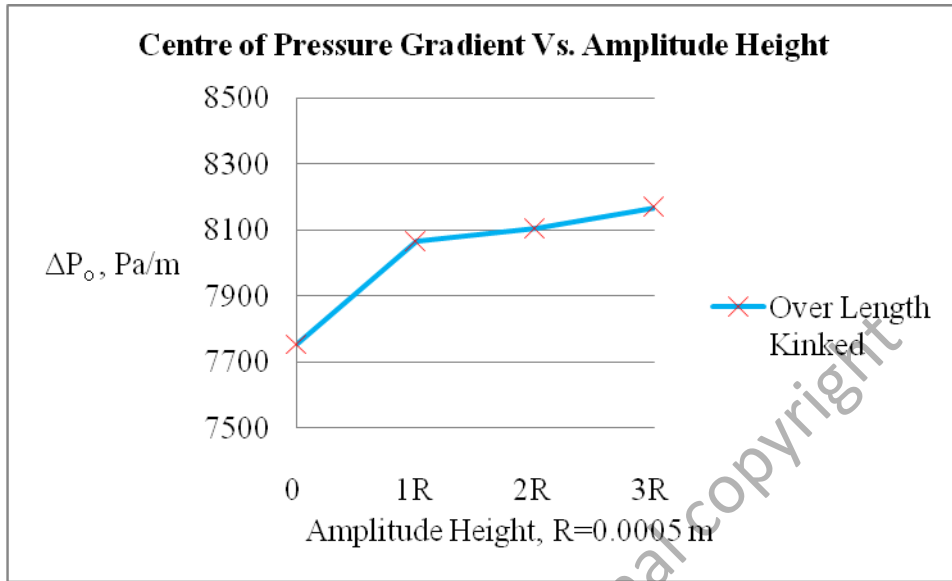


Figure 5.76: The centre of pressure gradient in different curvatures or cases of over the length kinked model.

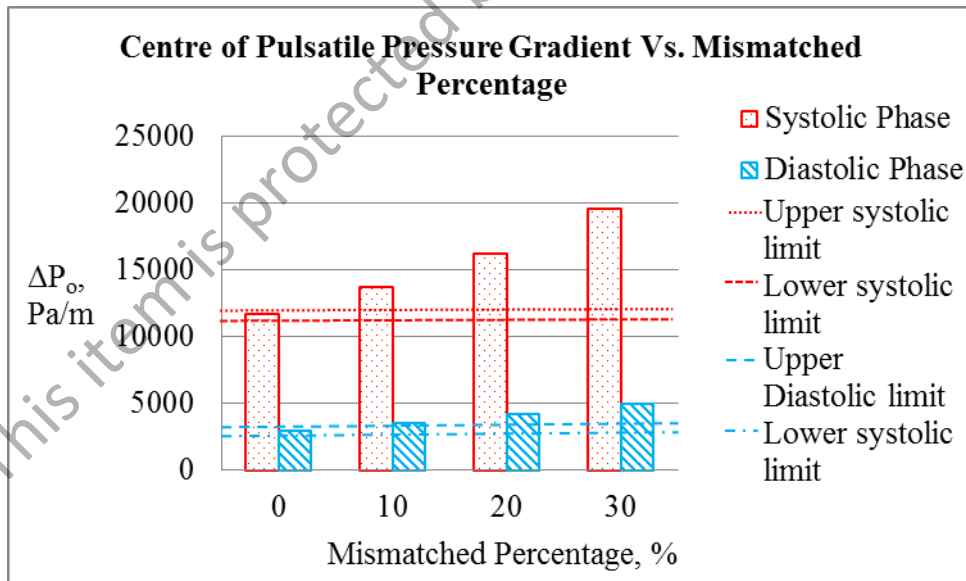


Figure 5.77 : The centre of pulsatile pressure gradient in different percentage or cases of the internal diameter mismatched model.

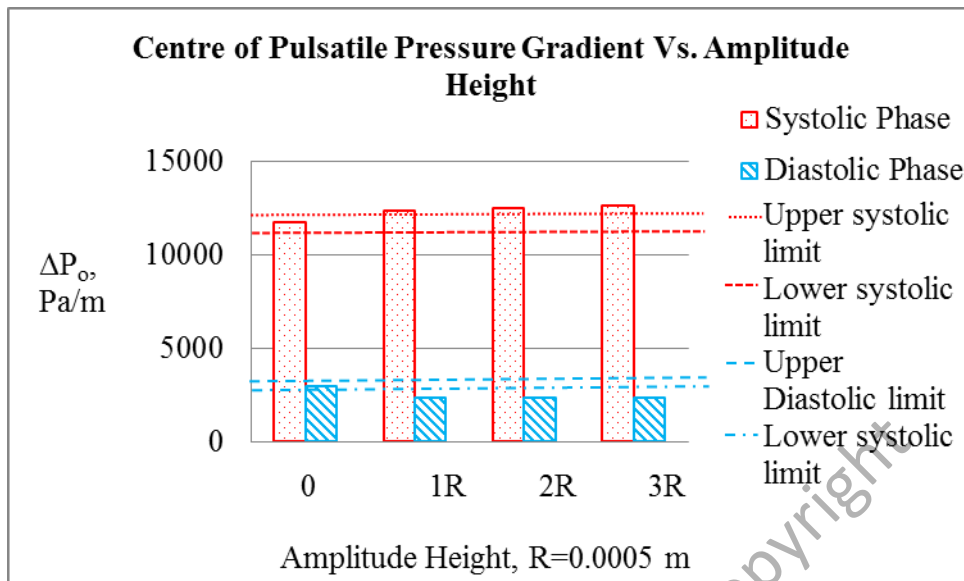


Figure 5.78 : The centre of pulsatile pressure gradient in different curvature or cases of the over length kinked model.

High blood pressure gradient is shown in Figure 5.75 and Figure 5.77 due to the cross section discrepancy between the cross section of the arteries and veins leading to high velocity flow. All kinking cases also demonstrate high blood pressure gradient at systolic phase and low blood pressure at diastolic phase due to the curvature geometry which leads to high and low velocity flow as shown in Figure 5.76 and Figure 5.78.

All irregular models should be below than 10% mismatched and 1R amplitude height to ensure prolonging survival. This is because the alteration of biological pulsatile pressure gradient is strongly related to the vein graft life span and this is supported by Christopher L. Skelly (2001).

### 5.5.3 Result and Discussion on the WSS Observation in Irregular Vein Graft

#### Models

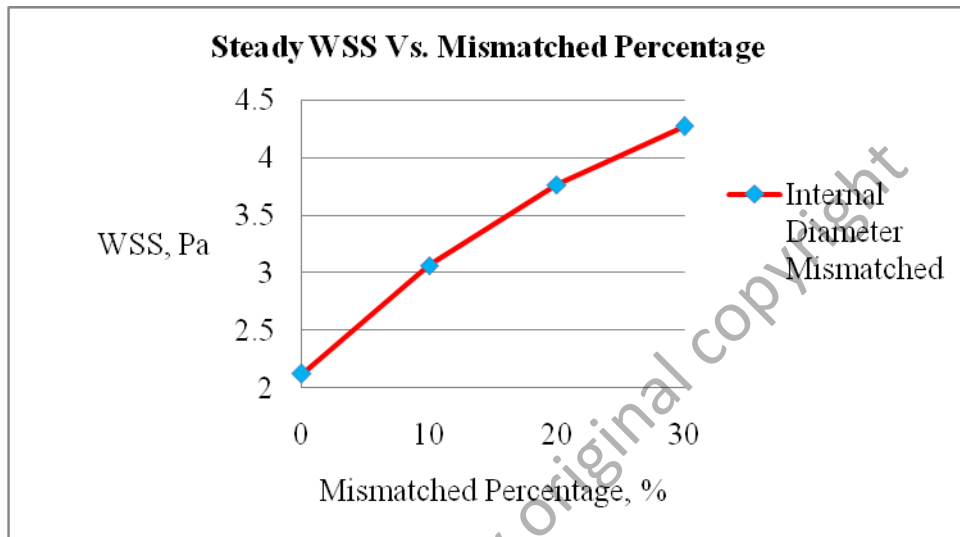


Figure 5.79 : The steady WSS in different percentage or cases of the internal diameter mismatched model.

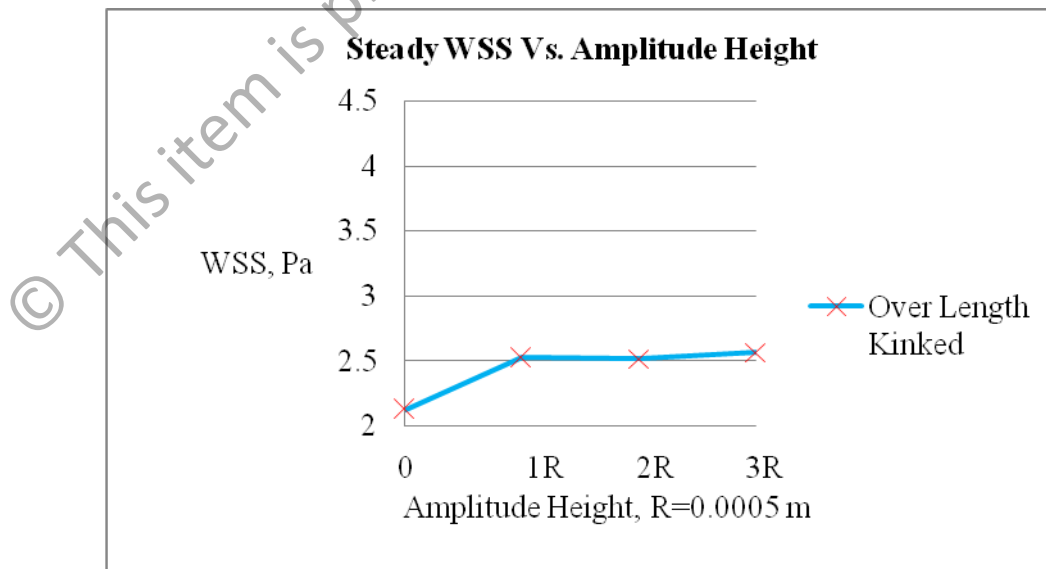


Figure 5.80 : The steady WSS in different curvatures or cases of the over length kinked model.

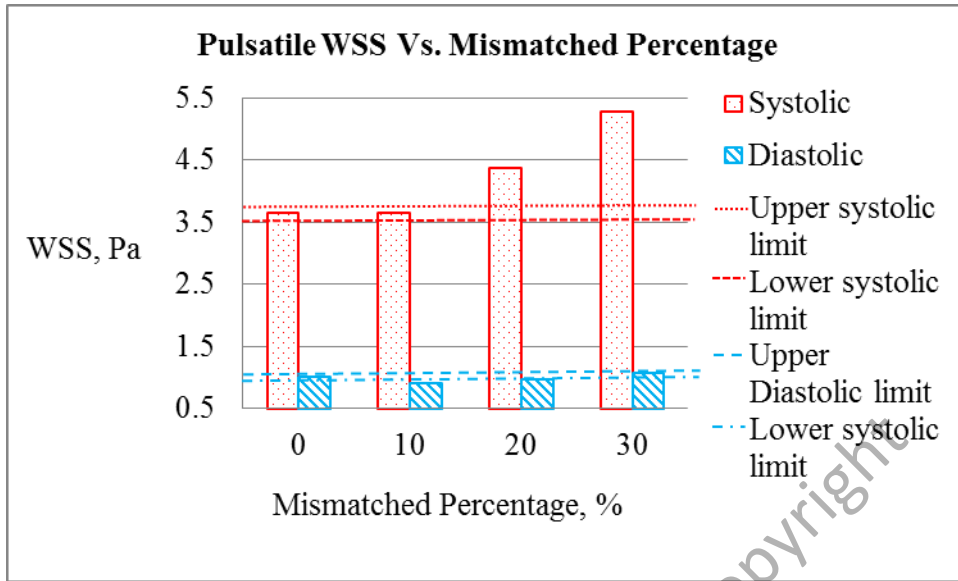


Figure 5.81 : The pulsatile WSS in different percentage of cases of the internal diameter mismatched model.

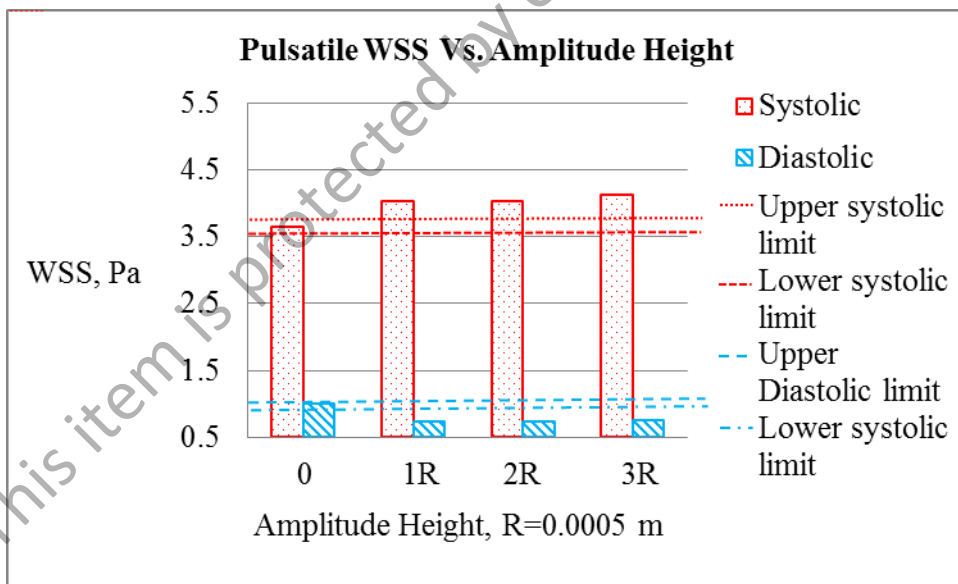


Figure 5.82 : The Pulsatile WSS in different curvatures or cases of the over length kinked model.

High pressure gradient at systolic and diastolic phases causes high WSS in all mismatched cases because of high pressure gradient. Meanwhile, high WSS was only

seen at systolic phase in all kinking cases because of the existing of high pressure gradient.

The abnormal shear stresses impact, such as very high or low pulsatile shear stresses may also lead to the thrombus formation. It happens due to a change of the biological behavior of platelet in the blood flow. Wilmer W. Nichols et al. (1998) and Krishnan B. Chandran et al. (2007) also suggested that the thrombus formation involves regulation of the release by the Endothium-Derived Relaxing Factor (EDRF), which believed to be nitric oxide. The modulation of the EDRF released by the WSS also influences the development of atherosclerosis via another mechanism and reduces the vein graft life span.

© This item is protected by original copyright



## CHAPTER 6

### CONCLUSION

#### 6.1 Summary

It is noted that the unpredicted failure in the vein graft can occur after the procedure was performed. Most defected fingers were pale and become cool as reported from previous studies. It happens because the flow of blood is blocked due to the formation of thrombus. The irregular vein geometry is believed to be the initiation of the thrombus formation. Based on several studies conducted previously, the irregular vein graft geometry occurs due to mismatching in internal diameter between the vein graft and the recipient artery as well as kinking because of the over size in length of the vein graft.

In biofluid studies, the abnormal behavior of the blood flow in velocity, pressure gradient and the WSS impact in the vessel wall will cause the growth of thrombus. In this study, we decided to mechanically analyze the behavior of blood flow and focus on velocity, pressure gradient and the WSS impact on the wall of vein graft. The 3D CFD Analysis was chosen as an experimental method since it provides high accuracy result. Furthermore, the 3D Analysis is one of reliable and acceptable methods that are still being applied by most researchers. The GAMBIT and the ANSYS Fluent commercial software were used in this simulation work as they receive good feedbacks based on reviews. The details of the vein graft geometry were decided after reading

clinical data in medical journals and having discussion with the surgeons. The 3D vein graft geometries were constructed in the GAMBIT software by assuming the vein graft geometries are cylindrical in shape. At this stage, we were dealing with the meshing drawing of the vein graft geometry. The quantity of cells possibly needs to be more but it still yield good results. The useless quantities of cell might affect the calculation of time at the simulation stage. For the analysis part, the created vein graft models were imported from the GAMBIT software into the ANSYS Fluent software. In the ANSYS Fluent software, the desired location and types of results monitoring and preferred parameter can be set. In this simulation work, the proximal, distal and wall of the vein grafts were selected as the location of the result monitoring. The point, plane and wall were applied as the types of monitoring views. The experiment results were presented in contours and graphs. The decision for all locations and types of monitoring views, and collected results are based on previous research works. In order to achieve our research goals, the pulsatile flow types were simulated on the vein graft models. However, the steady state flow is still needed and it plays an important role for result verification. Even though the latest and the best commercial software (i.e. GAMBIT and ANSYS Fluent) were implemented in this simulation work but it still requires some verification works. Thus, the experiment results were verified by using theoretical results. In this study, the error percentages were low and within the acceptable ranges.

The pulsatile laminar blood flow demonstrates an abnormal blood flow pattern in the model of irregular formation geometries compared to an ideal straight model (well matched in internal diameter and length). The vein graft models with the mismatching in internal diameter problem demonstrate high value in velocity of the blood flow, pressure gradient of blood flow between the proximal and distal, and the WSS impact on the wall of the vein grafts. Meanwhile, low value in velocity of the

blood flow, pressure gradient of the blood flow between the proximal and distal, and the WSS impact on the wall geometries can be seen in the vein graft models with the over length kinking problem.

The simulated models of irregular formation geometries have high possibility and potential in the re-formation of thrombus since a reduction in the vein graft area sizes (i.e. internal diameter mismatched problem) produced high value in velocity of the blood, pressure gradient and the WSS compare to simulated models of ideal straight. Even though the over length kink problem models demonstrate low value in velocity of blood and the WSS but, low pressure also initiates the re-formation of thrombus.

In conclusion, all geometries have been validated by simulating in the steady state blood flow before furthering analysis in the pulsatile flow. The simulations in the pulsatile blood flow type have been done in order to imitate the real environment. Critical ranges of geometry dimension have been identified. The only acceptable range of the RSVGs sizes mismatching less than 10% and kinking (amplitude height) less than 0.0005 m for 6.25 cm/s diastolic velocity blood flow. The simulation results reveal that irregular geometry formation models could reduce the lifespan of the RSVG by performing abnormal results in the blood flow velocity, pressure gradient and the WSS.

In the future, the well matched size in internal diameter and length of the RSVG is suggested for the recipient artery to avoid any failures in the revascularization procedure. Based on the experiment results of this research, it has been proven that the well matched size in internal diameter and length of the RSVG shows good and reasonable velocity of the blood flow, gradient pressure of the blood flow and the WSS impact on the wall of the vein graft.

## 6.2 Future Work

With regards to the future work, some recommendations on simulation are listed below as well as in experiment.

- Simulation works should be carried out for more complex geometry such as a real extracted Magnetic Resonance Imaging (MRI) 3D geometry, not by assuming that vein graft model only in cylindrical in shape.
- Simulation works can be extended by setting the vein graft wall as porous wall not only just rigid wall.

© This item is protected by original copyright

## REFERENCES

- A., Jafari, P., Zamankhan, S.M., Mousavi&P., Kolari (2009). Numerical investigation of blood flow. Part II: In capillaries. *Commun.Nonlinear Sci. Numer.Simul.* 14,1396–1402.
- Christopher L., Skelly, Shari L., Meyerson, Micheal A., Curi, Francis, Loth, & Lewis B., Schwartz (2001). The Hemodynamics of Vein Graft: Measurement and Meaning. *Ann of VascSurg*, vol. 15, 110-122.
- C.M., Grondin & R., Limet (1977). Sequential anastomoses in coronary artery grafting: technical aspects and early and late angiographic results. *Annals of Thoracic Surgery*, " 23, 1-8.
- C., Minale, N. P., Bourg, P., Bardos & B. J., Messmer (1984). Flow characteristics in single and sequential aorto-coronary bypass grafts. *Journal of cardiovascular Surgery (Torino)*, vol. 25, 12-15.
- Chuang, DC, Jeng, SF, Chen, HT, et al. (1982). Experience of 73 free groin flaps. *Br j PlastSurg* 45:81.
- Cole, JS, Watterson, JK & O'Reilly, M.J.G. (2003). Blood flow characteristics in a femoral artery bypass graft. *Dev. Chem. Eng. Miner. Process.* 11, 15–28.
- David S., Ruch, L. Andrew, Koman & Thomas L., Smith (2001). Chronic Vascular Disorders Of The Upper Extremity. *American Society for Surgery of the Hand*, Vol. 1, No. 1, February 2001.
- Doddi, S.K. & Bagchi, P. (2009). Three-dimensional computational modeling of multiple deformable cells flowing in microvessels. *Phys. Rev. E* 79 (046318) (14).
- Donald F., Young, Bruce R., Munson, Theodore H., Okiishi and Wade W., Huebsch (2003). *A Brief Introduction to Fluid Mechanics 4th Edition*. USA: John Wiley & Sons Inc..
- Dumanian GA, Segalman K, Buehner JW, Koontz CL, Hendrickson MF and Wilgis EF (1998). Analysis of digital pulse-volume recordings with radial and ulnar artery compression, *Plast Reconstr Surg*, Nov; 102(6), 1993-8.
- Ferziger, J. H. & Peric, M. (2002). *Computational methods for fluid dynamics*. 3<sup>rd</sup> edition. New York: Springer-Verlag Berlin Heidelberg.
- Filipovic, N., Tsuda, A., Lee, G.S., Miele, L.F., Lin, M., Konerding, M.A. & Mentzer, S.J. (2009). Computational flow dynamics in a geometric model of intussusceptive angiogenesis. *Microvasc. Res.* 78, 286–293.
- George D., Chloros, Robert M., Lucas, Zhongyu, Li, Martha B., Holden, AAS & L. Andrew, Koman (2008). Post-Traumatic Ulnar Artery Thrombosis: Outcome of Arterial Reconstruction Using Reverse Interpositional Vein Grafting at 2 Years Minimum Follow-Up. *J Hand Surgery*, vol. 33A, 932-940.

- GJ, Tangelder, DW, Slaaf, AM, Muijtjems, T, Arts, MG oude Egbrink & RS Reneman (1986). Velocity profiles of blood platelets and red blood cells following in arterioles of rabbit mesentery. *Circ Res.* 59:505-514.
- H., Piza-Katzer (1979). Analysis of Complications in Digital Vein Grafts. *Chirurgia plastic* by Springer-Verlag.
- I.G., Currie (2003). *Fundamental Mechanics of Fluids 3rd Edition*. USA: Marcel Dekker, Inc..
- Jocelyn A., Segall & Gregory L., Moneta (2007). Noninvasive Diagnosis of Upper Extremity Vascular Disease. *Section IV*, Pages 312-324.
- Sabik, JF (2011). Understanding Saphenous Vein graft Patency. *American Heart Association Journals, Circulation* 2011; 124: 273-275.
- Jung, J. and Hassanein, A. (2008). Three-phase CFD analytical modeling of blood flow. *Med. Eng. Phys.* 30, 91–103.
- Klyszcz T., Jünger M., Jung F. & Zeintl H. (1997). Cap image – a new kind of computer assisted video image analysis system for dynamic capillary microscopy (in German). *Biomed. Tech. (Berl)* 42, 168–175.
- Krishnan B. Chandran, Ajit P. Yoganathan and Stanley E. Rittgers (2007). *Biofluid Mechanics*. Taylor & Francis Group, LLC.
- Lee, Waite (2005). *Biofluid Mechanics in Cardiovascular Systems*. McGraw-Hill's Biomedical Engineering.
- M. N. Rahman, Y., Shahrman, A.B., Siti Khadijah, ZA'ABA, Roohi, S.A., Khairunizam, WAN & A.H., Ismail (2012). Computational Analysis of Hemodynamic Effect on Mismatch End-to-end Reverse Saphenous Vein Graft Diameters. *The 2nd International Malaysia-Ireland Joint Symposium on Engineering, Science and Business (IMiEJS 2012)*, 83.
- Meena, S., Dhanjoo N, Ghista, Poh, Chua & Tan, Yong Seng (2006). Numerical Investigation of Blood Flow in a Sequential Aorta-Coronary Bypass Graft Model. *Conf Proc IEEE Eng Med Biol Soc.*, 1:875-8.
- Mette S., Olufsen, Charles S., Peskin, Won Yong, Kim, Erik M., Pedersen, Ali, Nadim & Hesper Larsen (2000). Numerical Simulation and Experimental Validation of Blood Flow in Arteries with Structured-Tree Outflow Conditions. *Annals of Biomedical Engineering*, Vol. 28, pp.1281–1299.
- Minh Tuan Nguyen & Sang-Wook Lee (2012). Effect of secondary curvature on mixing characteristics within constant circular tubes. *World Academy of Science, Engineering and Technology*, Vol:6 2012-08-26.
- Muhammad Nur Rahman, Yahya, Shahrman, Abu Bakar, SK, Zaaba, Sharifah Roohi, Syed Waseem Ahmad, Wan Khairunizam, Wan Ahmad, M. Nasir, Ayob et al. (2012). Computational Analysis on Upper Extremity Vein Graft: Simulation on Kinked Vein Graft. *International Symposium on Robotics and Intelligent Sensors 2012 (IRIS 2012)*, *Procedia Engineering* 41, page 694 – 699.

- P., Berg, S., Schmitz, V., Lens & H., Farghadani (2007). Upper Extremity Occlusive Disease. *European Manual of Medicine. part 3*, 219-236.
- Qin, Liu, David, Mirc & Bingmei M., Fu (2008). Mechanical mechanism of thrombosis in intact bent microvessels of rat mesentery. *Journal of Biomechanics 41* 2726-2734.
- Raafat, Shalabi, Yoysifh, Al Amri & Elham, Khoujah (2006). Vascular injuries of the upper extremity. *J Vasc Brass. vol. 5*, No. 4.
- Rory F., Rickard, Chris, Meyer & Don A., Hudson (2009). Computational Modeling of Microarterial Anastomoses With Size Discrepancy ( Small-to-Large). *J Surg Res. 2009 May 1;153(1)*:1-11.
- Sang-Wook, Lee, Micheal A., Curi, Zachary K., Baldwin, Viji, Balasubramaniam, Francis, Loth & Lewis B., Schwartz (2003). Theoretical hydraulic consequences of vein graft taper. *J Vasc Surg, vol. 38*, 785- 792.
- Secomb, T.W., Styp-Rekowska, B., & Pries, A.R. (2007). Two-dimensional simulation of red blood cell deformation and lateral migration in microvessels. *Ann. Biomed. Eng. 35*, 755–765.
- Shahriman, A.B., M.N. Rahman, Y., Siti Khadijah, ZA'ABA, Khairunizam, WAN, Abdul Halim, ISMAIL, & Khairul, A.H., et al. (2012). Hemodynamic Study On Upper Extremity: Simulation On Straight Reverse Saphenous Vein Graft. *2012 International Conference on Biomedical Engineering (ICoBE)*, pp 207-210.
- Rainald Lohner (2008). Applied Computational Fluid Dynamics Techniques. *John Wiley & sons Ltd, the Atrium, Southern Gate, Chichester, West Sussex PO19 8SQ, England.*
- Texon M. (1957). The Hemodynamic Concept Of Atherosclerosis. *Bulletin of the New York Academy of Medicine Vol. 36, No. 4, April 1960.*
- Tu, J., Yeoh, G. H., & Liu, C. (2008). *Computational fluid dynamics*. Butterworth-Heinemann: Elsevier Inc.
- Tzu-Ching, Shih, Geoffrey, Zhang, Chih-Chieh, Wu, Hung-Da, Hsiao, Tsung-Hsin, Wu, Kang-Ping, Lin & Tzung-Chi, Huang (2011). Hemodynamic analysis of capillary in finger nail-fold using computational fluid dynamics and image estimation. *Microvascular Research 81*, 68-72.
- Van Carrel, A. & Guthrie, CC. (1906). Uniterminal and biterminal venous transplantations. *Surg Gynecol Obstet 2*, 266.
- Versteeg, H.K., & Malalasekara, W. (1995). *An Introduction To Computational Fluid Dynamics: The Finite Volume Method*. New York: John Wiley & Sons Inc.
- W. W. Jeong and K. Rhee (2009). Effect of surface and non-newtonian viscosity on the flow field in arterial stenoses. *Journal of Mechanical Science and Technology 23*, 2424-2433.
- Wilmer W., Nichols, Micheal F., O'rourke, & Craig, Hartley (1998). *McDonald's Flow in Arteries: Theoretical, experimental and clinical principles 4th Edition.*

Fourth Edition published in 1998 by Arnold, a member of the Hodder Headline Group, 338 Euston Road, London NW1 3BH

Ying, He, Hao, Liu, & Ryutaro, Himeno (2004). A one-dimensional thermo-fluid model of blood circulation in the human upper limb. *International Journal of Heat and Mass Transfer* 47, 2735-2745.

Zol B., Kryger, Vinay, Rawlani, & Gregory A., Dumanian (2007). Treatment of Chronic Digital Ischemia With Direct Microsurgical revascularization. *J Hand Surg* 2007; 32A:1466-1470.

© This item is protected by original copyright



## LIST OF PUBLICATION

- \*Muhd Nur Rahman Yahya, Shahrman Abu Bakar, SK Zaaba, Sharifah Roohi Syed Waseem Ahmad, Wan Khairunizam Wan Ahmad, M. Nasir Ayob, A.H. Ismail (2012). Computational Fluid Dynamic Analysis Of The Effect Of Kink Conduit In Microvascular Vein Grafting. *IJMME: International Journal of Mechanical & Mechatronics Engineering*. Vol. 12 Issue: 06 December 2012. Impact Factor : 0.9387 (2012).
- \*M. N. Rahman Y., Shahrman A.B., Siti Khadijah ZA'ABA, Roohi S.A., Khairunizam WAN (2012) Theoretical Approach On Vein Graft Survival: Simulation On Vein Graft. *International Journal of Medical Engineering and Informatics (IJMEI)*. Vol. 5 No. 4. 279-288.
- \*M. N. Rahman Y., SHAHRIMAN, A.B., SK Za'aba, Khairunizam WAN, SA Roohi M.D., HAZRY, D, Ahmad Helmy Abdul Karim M.D., SHAFRIZA, N.B, E.MCheng, MOHD AFENDI (2013) CFD Analysis On Mismatched End-to-end Internal Diameter of RSVG Models. *Journal of Advances in Environmental Biology* (have been accepted to be published in *Journal of Advances in Environmental Biology*)
- Shahrman A.B., \*M.N. Rahman Y., Siti Khadijah ZA'ABA, Khairunizam WAN, Abdul Halim ISMAIL, Khairul A.H., SA Roohi (2012). Hemodynamic Study On Upper Extremity: Simulation On Straight Reverse Saphenous Vein Graft. *2012 International Conference on Biomedical Engineering (ICoBE)*. 207-210.

- \*M. N. Rahman Y., Shahrman A.B., Siti Khadijah ZA'ABA, Roohi S.A., Khairunizam WAN, A.H. Ismail (2012). Computational Analysis of Hemodynamic Effect on Mismatch End-to-end Reverse Saphenous Vein Graft Diameters. *The 2nd International Malaysia-Ireland Joint Symposium on Engineering, Science and Business (IMiEJS 2012)*. 466-474.
- \*Muhd Nur Rahman Yahya, Shahrman Abu Bakar, SK Zaaba, Sharifah Roohi Syed Waseem Ahmad, Wan Khairunizam Wan Ahmad, M. Nasir Ayob, A.H. Ismail (2012). Computational Analysis on Upper Extremity Vein Graft: Simulation on Kinked Vein Graft. *International Symposium on Robotics and Intelligent Sensors 2012 (IRIS 2012)*, Procedia Engineering 41. 694-699.
- \*M. N. Rahman Y., Shahrman A.B., Siti Khadijah ZA'ABA, Roohi S.A., Khairunizam WAN, A.H. Ismail (2012). Computational Fluid Dynamic Analysis On Microvascular Vein Grafting: Effect of Mismatched Conduit Diameters. *2012 IEEE EMBS International Conference on Biomedical Engineering and Sciences (IECBES 2012)*. 978-1-4673-1666-8.
- \*M. N. Rahman Y., SHAHRIMAN, A.B., SK Za'aba, Khairunizam WAN, SA Roohi M.D., HAZRY, D, Ahmad Helmy Abdul Karim, SHAFRIZA, N.B, E.MCheng, MOHD AFENDI (2013). CFD Analysis on Mismatched End-to-end Internal Diameter of RSVG Models. *Proceedings of the 2nd International Conference on International Conference on Robotic Automation System (ICORAS 2013)*. In publishing.

## LIST OF AWARD

1. Best paper award for 2nd Int Conference on Eng Tech ICET 2013, for paper entitled "CFD ANALYSIS ON MISMATCHED END TO END INTERNAL DIAMETER OF RSVG MODELS"

© This item is protected by original copyright

## APPENDIX A

### Step of vein graft model geometry construction in GAMBIT 2.4.6.

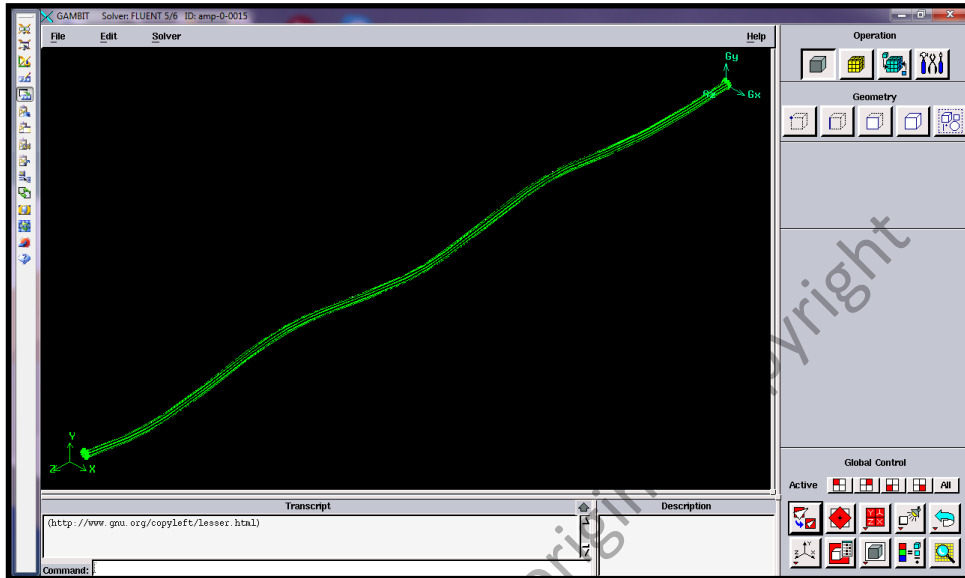


Figure A.1 : Geometry construction of vein graft model.

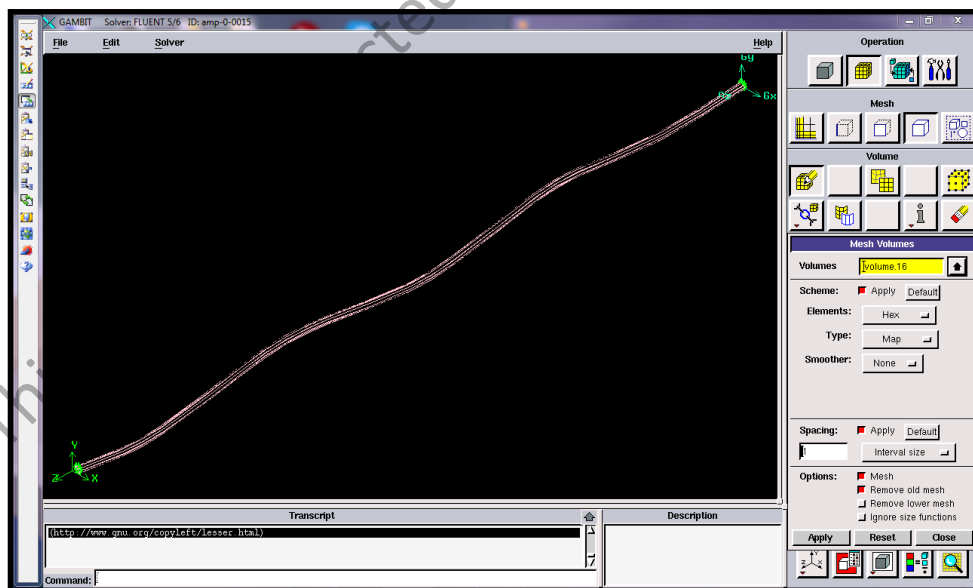


Figure A.2 : Geometry meshing construction of vein graft model.

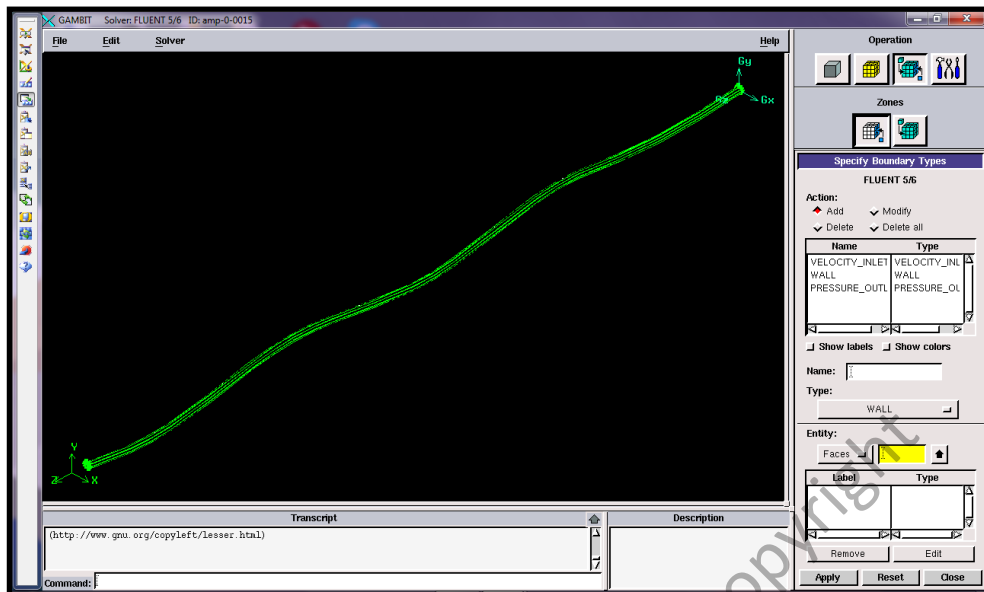


Figure A.3 : Geometry boundary condition setting of vein graft model.

Velocity inlet as Proximal region (inlet), wall of vein graft model as Wall region (wall) and pressure outlet as Distal Region (outlet).

© This item is protected by Original Copyright

## APPENDIX B

### Analysis of vein graft model in ANSYS Fluent V12.1.

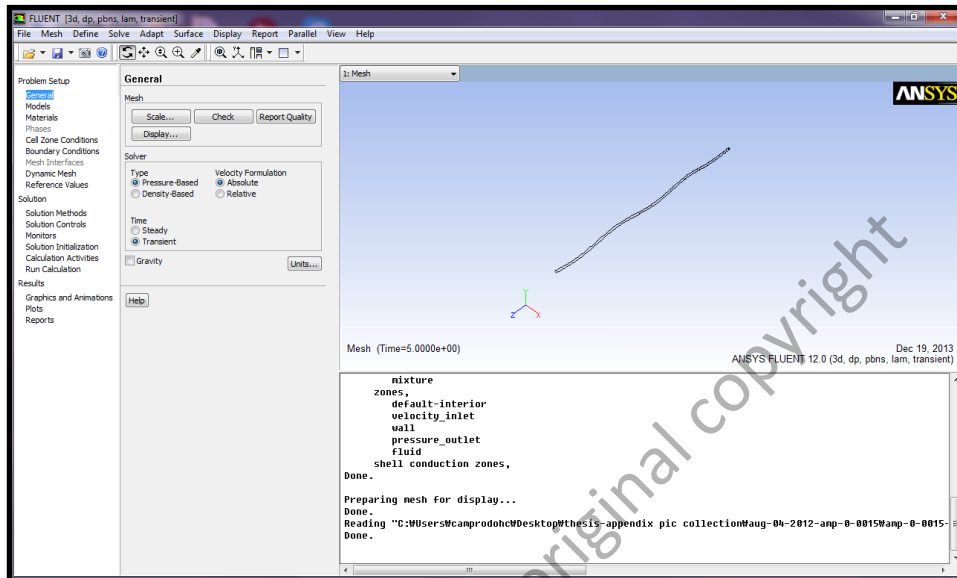


Figure B.1 : Problem Setup. Mesh ; Check icon for geometry volume status whether in error or good. Solver ; Pressure-Based is selected since this simulation deal with low speed flow and absolute is selected in Velocity Formulation. Steady time is chosen for steady state flow and Transient time is chosen for pulsatile state flow.

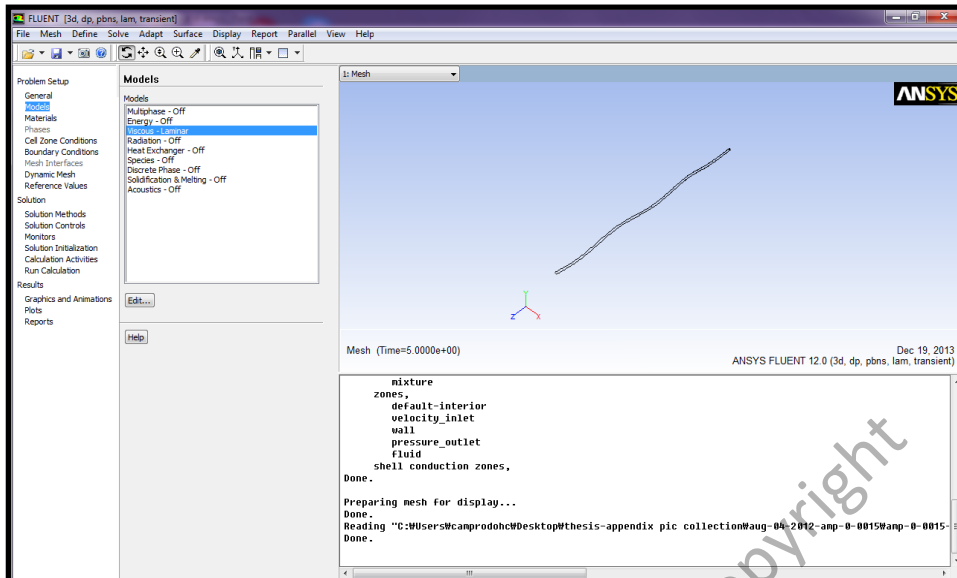


Figure B.2 : Problem Setup. Models ; Laminar is chosen as Viscous since all simulations deal with laminar blood flow.

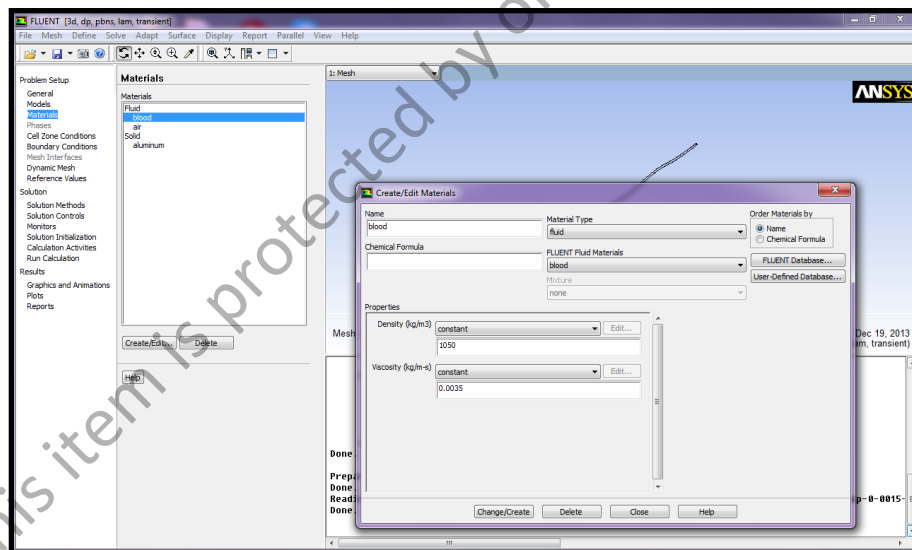


Figure B.3 : Problem Setup. Materials ; Fluid (Blood) properties are inserted.

Fluid (air) and solid (aluminium) material are default setting by Fluent ANSYS and no need to be defined.

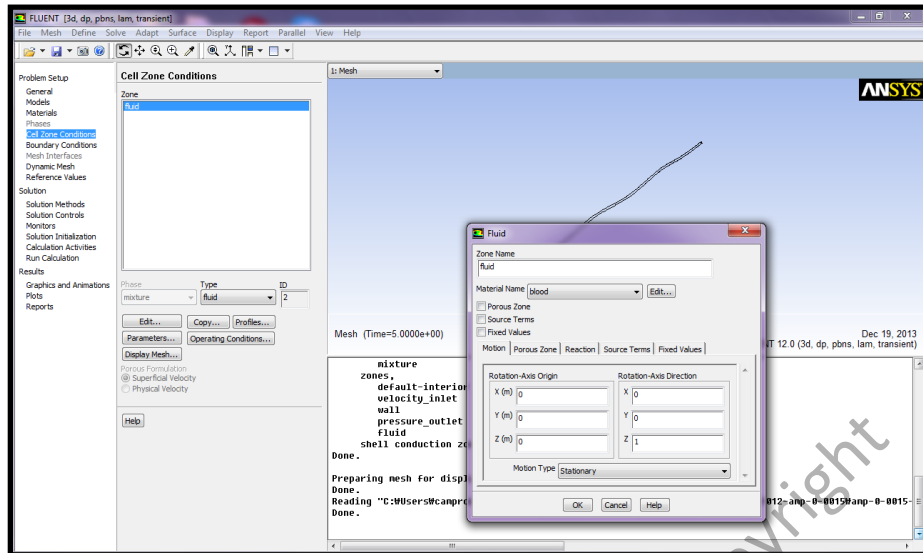


Figure B.4 : Problem Setup. Cell Zone Conditions ; Fluid (zone) is selected.

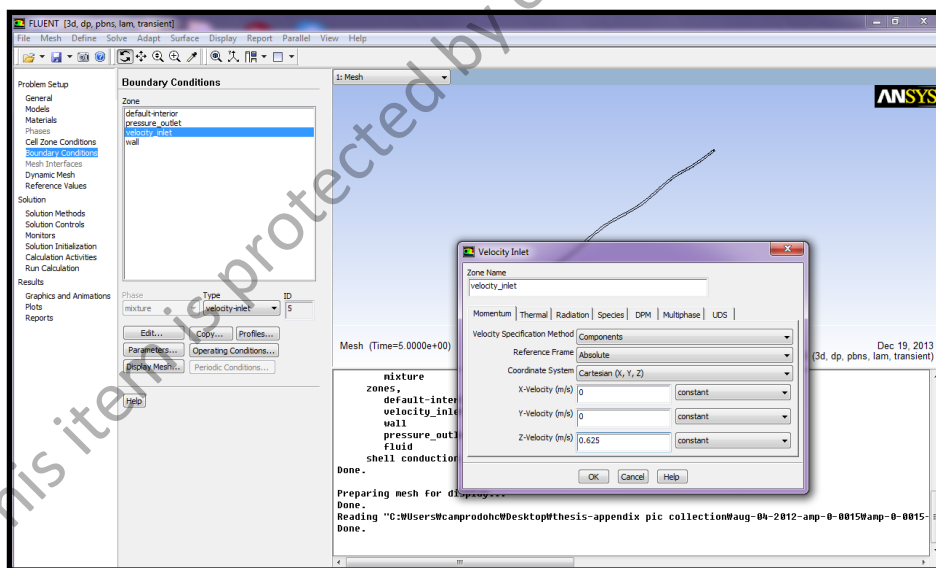


Figure B.5 : Problem Setup. Boundary Conditions ; Velocity Inlet (zone) is selected and desired velocity of blood flow is set. For the steady state flow, velocity is constant.



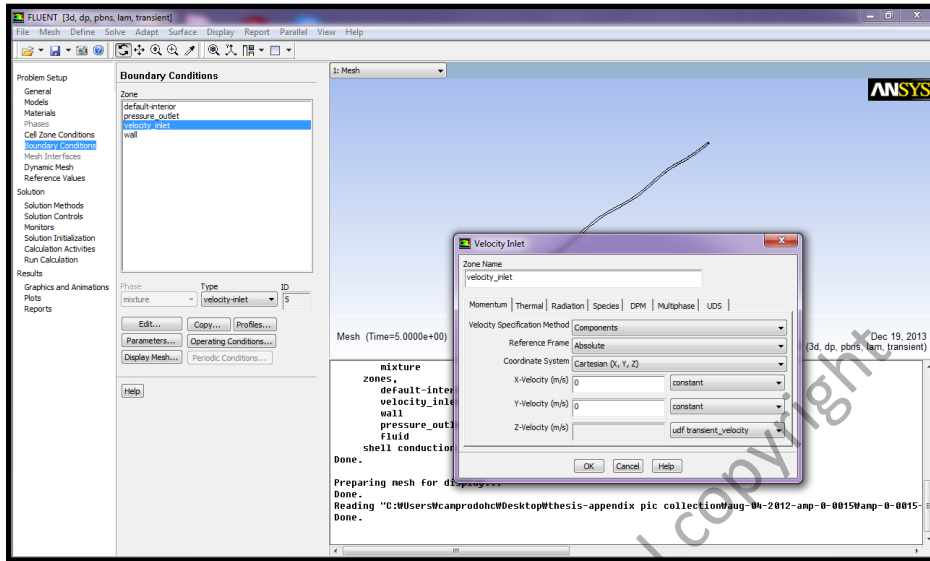


Figure B.6 : Problem Setup. Boundary Conditions ; For the pulsatile state flow, velocity is interpreted from udf file (see Appendix C) based on desired axis direction.

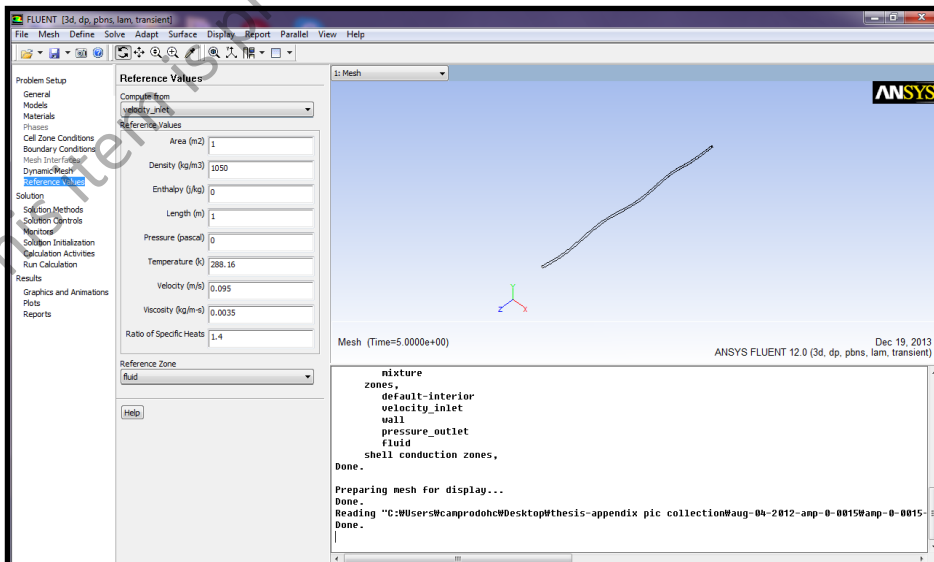


Figure B.7 : Problem Setup. Reference Values ; Computation from velocity inlet (Proximal region) and Fluid is selected as Reference Zone as well.

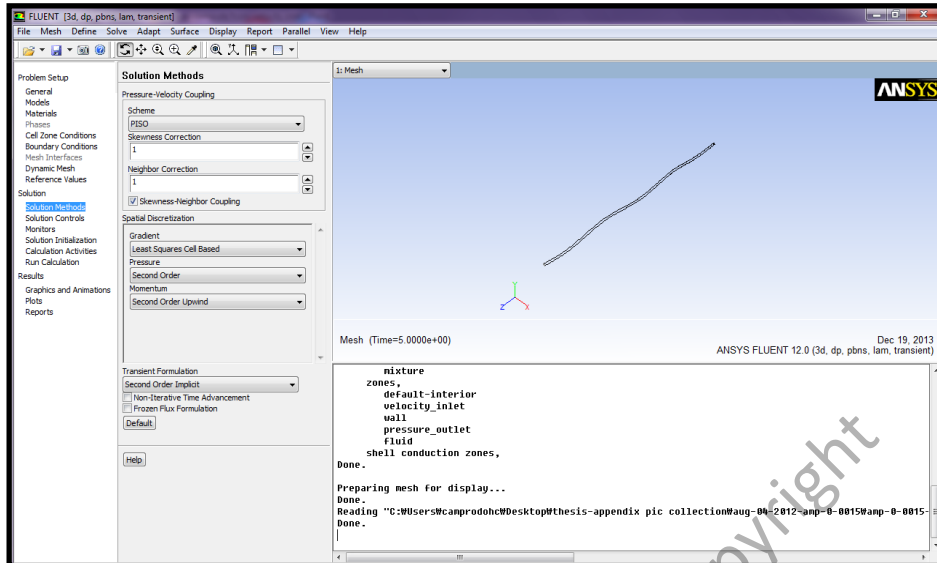


Figure B.8 : Solution. Solution Methods ; PISO is selected as Scheme. In order to optimize in calculating, Least Square Cell Based in Gradient, Second Order in Pressure and Second Order Upwind in Momentum are selected as well.

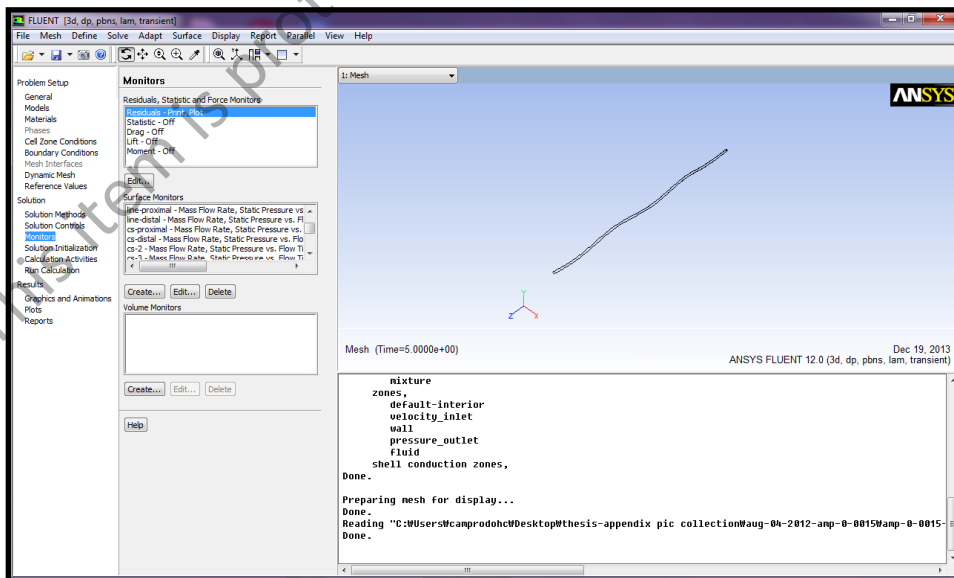


Figure B.9 : Solution. Surface Monitors ; In order to collect analysis data, we can create type of surface monitor and position.

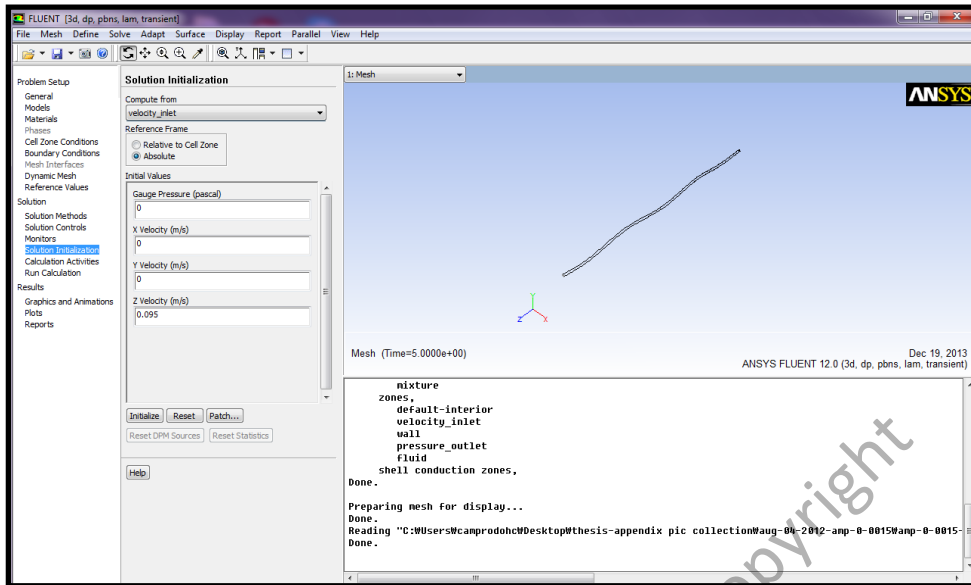


Figure B.10 : Solution. Solution Initialization.

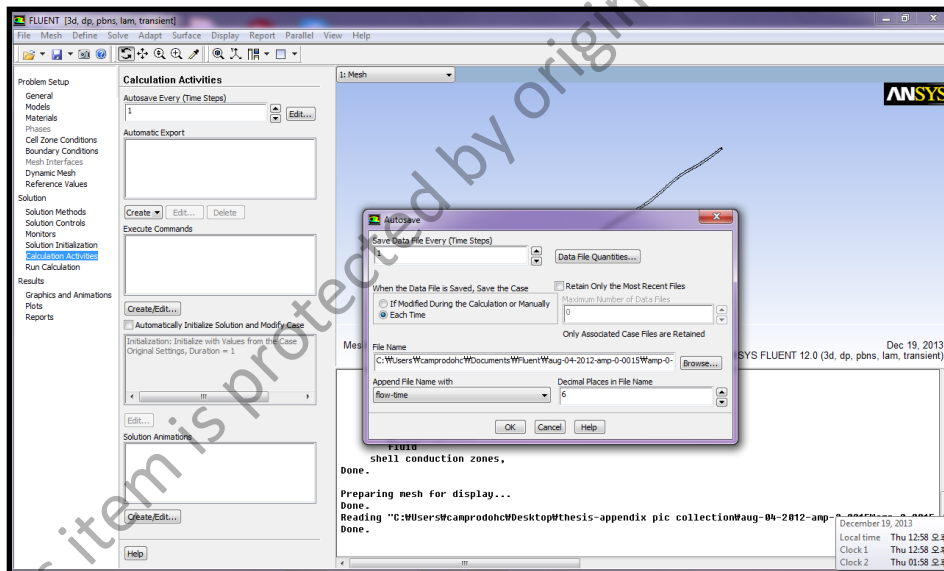


Figure B.11 : Solution. Calculation Activities ; We can save data file every time step or desired iterations.

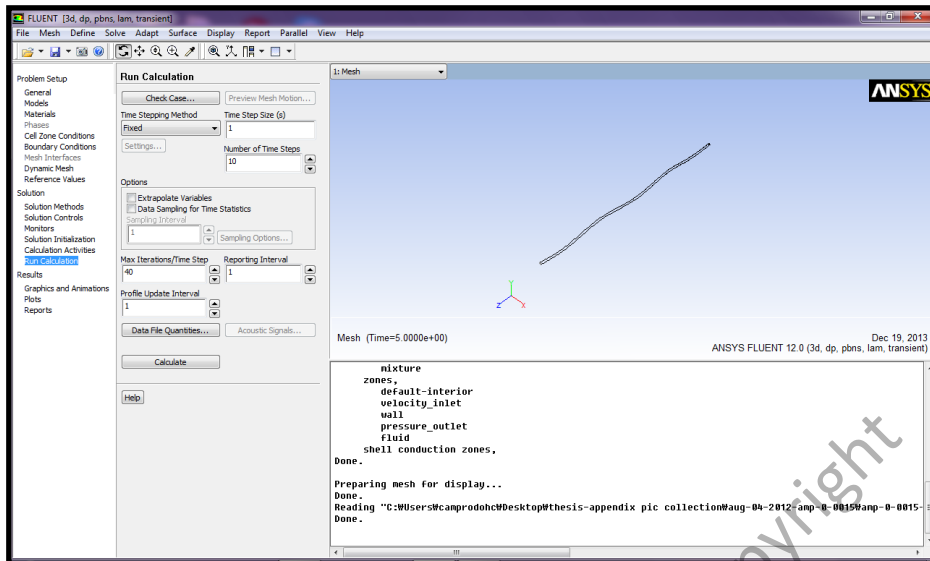


Figure B.12 : Solution. Run calculation ; Time Step Size is set as 1 and the Number of Time Steps are 10 since only 10 seconds are required for this simulation (applicable only for pulsatile flow).

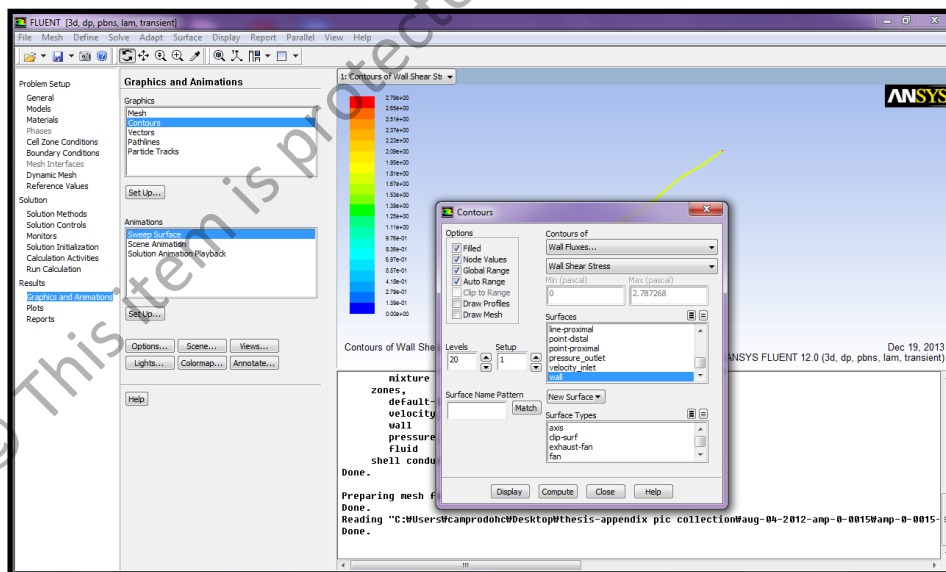


Figure B.13 : Result. Graphics and Animations ; For example, for the wall of vein graft model, Contour of result is selected for graphics and there is legend of value also available for reference.

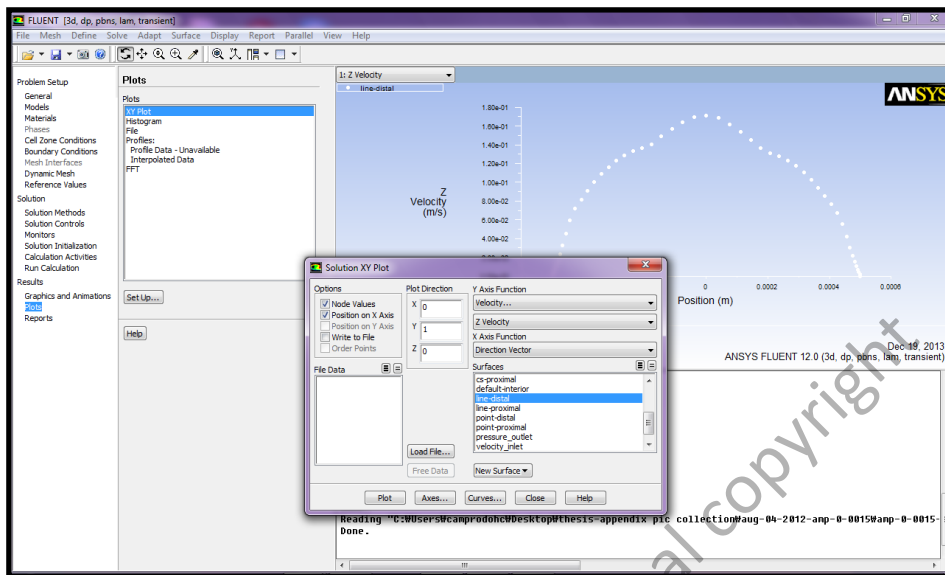


Figure B.14 : Results. Plots; XY Plots is selected and export it to Microsoft Office Excel in order to proceed the detail values.

## APPENDIX C

### User Define Function

**File type:** C File

**Details:**

```
#include "udf.h"
```

```
#include "math.h"
```

```
DEFINE_PROFILE(transient_velocity, thread, position)
```

```
{
```

```
float t, velocity;
```

```
face_t f;
```

```
t = RP_Get_Real("flow-time");
```

```
velocity = 0.0625 + 0.03125 * sin(M_PI/2 * t);
```

```
begin_f_loop(f, thread)
```

```
{
```

```
F_PROFILE(f, thread, position) = velocity;
```

```
}
```

```
end_f_loop(f, thread)
```

```
}
```